Measurement of the $\Upsilon(4S) \to B^0\overline{B}^0$ branching fraction at the Belle experiment

Pascal Schmolz

München 2024

Measurement of the $\Upsilon(4S) \to B^0\overline{B}^0$ branching fraction at the Belle experiment

Dissertation
an der Fakultät für Physik
der Ludwigs-Maximilians-Universität
München

vorlegt von
Pascal Maurice Schmolz
aus Stuttgart

München, den 12. Juni 2024

Messung des Verzweigungsverhältnisses von $\Upsilon(4S) \to B^0\overline{B}^0$ am Belle Experiment

Dissertation
an der Fakultät für Physik
der Ludwigs-Maximilians-Universität
München

vorlegt von
Pascal Maurice Schmolz
aus Stuttgart

München, den 12. Juni 2024

Erstgutachter:	Prof. Dr. Thomas Kuhr
Zweitgutachter:	Prof. Dr. Wolfgang Dünnweber
Tag der mündlichen Prüfung:	26. Juli 2024

Zusammenfassung

B-Fabriken sind Elektron-Positron-Teilchenbeschleuniger, deren Zweck in der Erzeugung einer möglichst hohen Anzahl an B-Mesonen besteht. Die Schwerpunktsenergie der Kollision ist dabei so gewählt, dass mit hoher Wahrscheinlichkeit eine $\Upsilon(4S)$-Resonanz entsteht. Der kurzlebige Zustand aus einem Bottom- und einem Antibottom-Quark zerfällt anschließend überwiegend in ein Paar aus B-Mesonen. Aus der zur Verfügung stehenden Energie und der Ladungserhaltung ergibt sich, dass entweder ein Paar ungeladener oder geladener B-Mesonen entsteht.

Die Produktionsraten von geladenen und ungeladenen Paaren an B-Fabriken ist für eine Vielzahl von Präzisionsmessungen von entscheidener Bedeutung. Es ist häufig von Vorteil, physikalische Größen indirekt über Verhältnisse andere Größen zu ermitteln, anstatt diese direkt zu bestimmen.

Entsprechend wurden bisher auch die Verzweigungsverhältnisse $\mathcal{B}\big(\Upsilon(4S) \to B^+B^-\big)$ und $\mathcal{B}\big(\Upsilon(4S) \to B^0\overline{B}^0\big)$ primär über das Verhältnis $R^{c/n}$ beider Größen bestimmt:

$$R^{c/n} = \frac{\mathcal{B}\big(\Upsilon(4S) \to B^+B^-\big)}{\mathcal{B}\big(\Upsilon(4S) \to B^0\overline{B}^0\big)}, \tag{1}$$

wobei $\mathcal{B}$ ein Verzweigungsverhältnis bezeichnet. Die vorliegende Dissertation befasst sich hingegen mit der direkten Messung von f_{00}, definiert als

$$f_{00} = \mathcal{B}\big(\Upsilon(4S) \to B^0\overline{B}^0\big). \tag{2}$$

Dazu wird ein am *Belle*-Experiment aufgenommener Datensatz mit einer integrierten Luminosität von $571\,\mathrm{fb}^{-1}$ ausgewertet. Die direkte Messung von f_{00} wird durch eine Methode ermöglicht, die auf der Rekonstruktion der beiden im Kollisionsereignis erzeugten B-Mesonen im gleichen Zerfallskanal beruht. Dies wird als *Double-Tagging* bezeichnet. Das in der vorliegenden Analyse ermittelte Ergebnis beträgt

$$f_{00} = 0.477 \pm 0.005_{\mathrm{stat}} \pm 0.013_{\mathrm{syst}}\,, \tag{3}$$

wobei der zweite Term die statistische Unsicherheit und der dritte Term die systematische Unsicherheit angibt.

Der in dieser Dissertation ermittelte Wert von f_{00} stimmt sowohl mit dem von der *Particle Data Group*[1] aus mehreren indirekten Messungen berechneten Mittelwert als auch mit dem 2005 publizierten Ergebnis einer *BaBar*-Analyse[2], der bisher einzigen direkten Messung dieses Verzweigungsverhältnisses, überein.

Abstract

B factories are electron-positron accelerators whose purpose is to generate the highest possible number of B mesons. The centre-of-mass energy of the collision is set to produce a $\Upsilon(4S)$ resonance with the highest probability. The short-lived state consisting of a bottom and an antibottom quark subsequently decays predominantly into a pair of B mesons. The available energy and the conservation of charge result in a decay to either a pair of uncharged or charged B mesons.

The rate at which either a charged or uncharged pair is created is of decisive importance for a variety of precision measurements. From an experimental point of view, it is often more advantageous to determine physical quantities in ratios instead of determining them directly. Accordingly, the branching ratios of $\Upsilon(4S)$ have so far been determined primarily via the ratio $R^{c/n}$ of two branching fractions:

$$R^{c/n} = \frac{\mathcal{B}\big(\,\Upsilon(4S) \to B^+B^-\,\big)}{\mathcal{B}\big(\,\Upsilon(4S) \to B^0\overline{B}^0\,\big)}, \tag{4}$$

where $\mathcal{B}$ denotes the branching ratio.

This dissertation, by contrast, addresses the direct measurement of f_{00}, defined as

$$f_{00} = \mathcal{B}\big(\,\Upsilon(4S) \to B^0\overline{B}^0\,\big). \tag{5}$$

For this purpose, a data set recorded at the *Belle* experiment with an integrated luminosity of $571\,\mathrm{fb}^{-1}$ is analysed. The direct measurement of f_{00} is enabled by a method based on the reconstruction of the two B mesons generated in the collision event in the same decay channel. This is called *double tagging*. The result determined in the present analysis amounts to

$$f_{00} = 0.477 \pm 0.005_{\mathrm{stat}} \pm 0.013_{\mathrm{syst}}\ , \tag{6}$$

where the second term indicates the statistical uncertainty and the third term the systematic uncertainty.

The value of f_{00} determined in this dissertation agrees both with the mean value calculated by the *Particle Data Group* [1] from several indirect measurements and with the result of a *BaBar* analysis [2] published in 2005, the only direct measurement of this branching ratio to date.

Contents

Chapter 1

Introduction

In addition to providing data for high precision measurements, the distinct advantage of B factories is the ability to determine absolute branching fractions. This sets B factories apart from hadron collider experiments like the LHC. By colliding elementary particles, the initial conditions are known, which allows for the determination of the totally produced pairs of B mesons, a number needed to normalize the decay rate. Absolute branching fractions of charged and neutral B meson decays are important input parameters for a large part of the analyses in the flavor physics program. These include testing Standard Model parameters like the CKM matrix elements, as well as searching for rare decays that may reveal physics beyond the Standard Model.

As numerous novel insights rely on high precision measurement, it is necessary that input parameters are known with high precisions as well. Among the important input parameters are the branching fractions, in particular those of the $\Upsilon(4S)$ decay. Precisely measured $\Upsilon(4S)$ branching fractions serve not only as essential input for subsequent analyses but also as a means of investigating isospin symmetry breaking in the environment of the $\Upsilon(4S)$ resonance. The breaking of isospin symmetry is the reason for the production asymmetry of charged and neutral B meson pairs. Moreover, the determination of the branching fractions of $\Upsilon(4S)$ enables to constrain the contributions of non-$B\overline{B}$ decay channels to the total decay rate of the $\Upsilon(4S)$.

The dissertation at hand presents a detailed documentation of the measurement of f_{00}, the branching fraction of the decay $\Upsilon(4S) \to B^0\overline{B}^0$. The data, consisting of $571\,\mathrm{fb}^{-1}$, is recorded at the *Belle* experiment, where electrons and positrons are brought to collision at a center-of-mass energy corresponding to the mass of the $\Upsilon(4S)$ resonance. Using the *single and double tag* method, sometimes just referred to as double-tagging, the determination is performed without assuming isospin symmetry. This model independent method allows a direct measurement of the branching fraction f_{00}, making it the second such measurement to date.

Given that double-tagging requires a fairly substantial amount of data, a frequent and comparatively accessible decay channel is chosen: $B^0 \to D^{*-}(\to \overline{D}^0\pi^-)\ell\nu_\ell$. In order to select as many of these decays as possible, a partial reconstruction is carried out.

In the course of developing the analysis, particularly the reconstruction efficiencies have raised concerns. Unexpected correlations have been revealed between the efficiencies of single-tagged and double-tagged B candidates, in contrast to the reference measurement conducted at the *BaBar* experiment [2]. Moreover, it is observed that the efficiencies vary significantly between different data taking periods. Great effort has been made to gain insight into the reasons for the correlation and the dependency on the data taking period, yet it has only been demonstrated that none of them have an impact on the final result.

The thesis is structured as follows. It begins with a description of the theoretical basis of this measurement. A brief introduction to the Standard Model of particle physics is followed by an explanation of isospin symmetry and how isospin relates to the measurement of f_{00}. An overview of various model calculations dedicated to the production asymmetry of charged and neutral B mesons in the $\Upsilon(4S)$ decay is presented. The theory chapter concludes with an experimental perspective of this issue. The following chapter introduces the *Belle* Experiment in general and the instrumentation of the detector in particular. The next chapter mentions the analysis software and describes the details of the data sets used to develop and perform the measurement. The special focus here is on the evaluation and application of corrections to the simulated data samples. The following three chapters explain the analysis method in detail. Both the implementation and the subsequent validation are discussed. The subsequent chapter describes the determination of the systematic uncertainties. The last two chapters present the results of the measurement, discuss them and provide an outlook for future investigations.

Conventions

The system of natural units is used throughout this thesis, i.e. $c = \hbar = 1$. If not stated otherwise, charge conjugation regarding particles and decays is implied. The symbol ℓ represents an electron or a muon, explicitly excluding taus.

Chapter 2

Theory

This chapter gives a brief description of the theoretical basis of particle physics, the Standard Model. After the introduction of the particle content and the interactions, the strong isospin is discussed. The concept of isospin is historically motivated, the details of the formulations are explained, and the transition to the Standard Model is described. In the following, the significance of isospin for the analysis described in this thesis is explained. The chapter concludes with a theoretical discussion of the experimental perspective on the quantity to be determined in the analysis.

2.1 The Standard Model

The theoretical framework on which our understanding of subatomic physics is based is known as the Standard Model of particle physics (SM) [3, 4]. The theory encompasses all known elementary particles and describes the fundamental forces governing their interactions.

The Higgs mechanism, an essential component of the SM, and the corresponding Higgs boson, are not introduced in this brief overview. A detailed description about the Higgs sector is found in [5].

2.1.1 Fundamental particles

The SM distinguishes between two distinct groups of particles based on the particle's spin quantum number. A concise representation of all particles and their defining properties is shown in Figure 2.1.

The particles in the first category are referred to as fermions and are characterized by a spin of $\frac{1}{2}$, or generally half-integer spins. Fermions serve as the fundamental constituents of matter. The SM additionally differentiates between two distinct types of fermions: Leptons and quarks. They differ by several quantum numbers. One of these numbers is the electric charge.

Six types of leptons exist, grouped into three generations, each comprising one charged and one neutral particle. The charged leptons — electron (e), muon

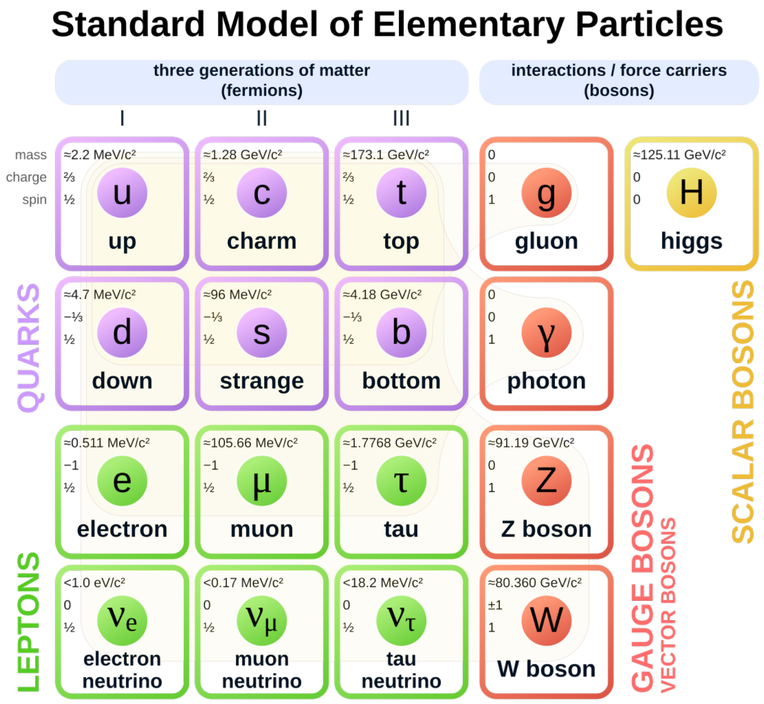

Figure 2.1: The particle content of the Standard Model of particle physics [6], including their masses, electrical charges and spin quantum numbers.

(μ), and tau (τ) — increase in mass sequentially and carry a negative elementary charge. Each charged lepton is paired with a neutral counterpart, forming a generation: the electron neutrino (ν_e), the muon neutrino (ν_μ), or the tau neutrino (ν_τ), respectively.

Quarks are likewise arranged in three generations, where one generation consists of an up-type quark carrying a $+\frac{2}{3}$ fraction of the elementary charge, and a down-type quark with $-\frac{1}{3}$ of elementary charge. The constituents of the first quark generation are designated as up (u) and down (d), while those of the second generation are known as charm (c) and strange (s), and the top (t) and bottom (b) quark form the last generation. The six types of quarks are also referred to as flavors.

In contrast to leptons, quarks have an additional quantum number, in addition to the electric charge they also carry color charge. In addition to the twelve fermions described above, the SM incorporates twelve antiparticle counterparts, each with opposite charges, reflecting the solutions of the Dirac equation, which include both positive and negative energy states [7].

The second category comprises bosons, particles that possess integer spin. Bosons act as carriers of the fundamental forces, further described in the next section. Since the interactions between particles are formulated as gauge theories, the force transmitting particles are also referred to as gauge bosons. The SM incorporates four such gauge bosons: photons (γ), gluons (g), $W^{\pm}$ bosons and Z^0 bosons.

2.1.2 Fundamental forces

Three types of interactions are included in the theoretical framework of the SM: the electromagnetic interaction, the weak interaction and the strong interaction. The fourth of the fundamental forces, gravity, is too weak to play a role at the scale of subatomic particles. Consequently, in contrast to the SM interactions, it has not yet been successfully formulated as a quantum field theory.

In quantum electrodynamics, the theory describing the electromagnetic force, photons are the excitations of the electromagnetic field and serve as mediators of the interaction. Since photons couple to electrical charge, carrying such charge is a prerequisite for participating in electromagnetic interactions. The electromagnetic coupling strength is comparatively high, since photons are massless and do not carry electrical charge themselves. Therefore, the range of the interaction is theoretically infinite. This is why the behavior of atoms and molecules is dominated by the electromagnetic interaction.

The weak interaction possesses the lowest coupling strength of all interactions and has a very short effective range [8]. This is due to the high masses of its mediators, the neutral Z^0 boson and the charged $W^\pm$ bosons. All fermions of the SM participate in weak interactions, neutrinos even exclusively. Due to the conservation the lepton number, leptons within a generation can therefore only interact through the weak interaction. Similarly, quarks are able to change their flavor only in weak interactions. The transition probabilities of the quark flavour are described by a unitary 3×3 matrix, the CKM-matrix [9]. The weak interaction is the only interaction that violates the parity symmetry, and furthermore, in particularly interesting for B physics, the only interaction that violates the charge-parity symmetry [10].

The fundamental theory governing the strong interaction is known as quantum chromodynamics (QCD), describing the dynamics of quarks and gluons [11]. Unlike the binary electrical charge, this interaction is characterized by a unique property known as color charge, where three such charges are necessary for achieving charge neutrality.

Gluons, the mediators of the strong force, carry one unit of color and one unit of anticolor, enabling self-coupling interactions distinct from the photon-mediated electromagnetic force. Quarks, the constituents of hadrons, also carry color charge, with antiquarks carrying anticolor charge. Notably, the confinement phenomenon within QCD prevents the isolation of individual quarks and gluons, compelling them to exist only within color-neutral bound states. Consequently, isolated quarks or gluons could not be observed in any experiment, but only in bound states. Confinement manifests in collider experiments through phenomena such as string-breaking, where increasing separation between quarks results in the generation of new quark-antiquark pairs, leading to the formation of colorless hadrons, and especially in hadron colliders, to the production of jets, stemming from the cascade of quark-antiquark pairs initiated by initially energetic colored particles. Furthermore, confinement contributes to the short-range nature of the strong interaction.

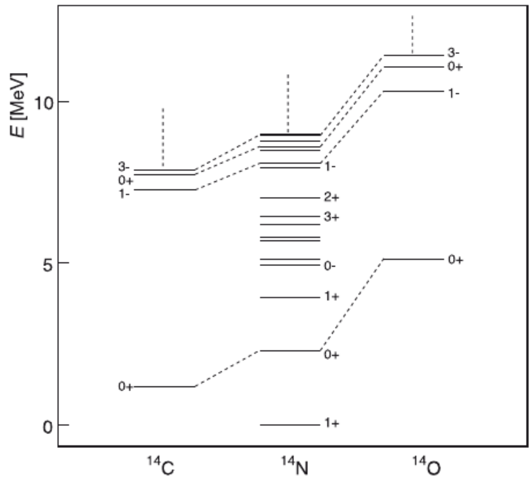

Figure 2.2: Energy spectra of excited mirror nuclei with mass number $A = 14$ [14]. Analogous states in the nuclei are linked by dashed lines. Mirror nuclei are nuclei with interchanged numbers of protons and neutrons. The similarity in the energy spectra led to the introduction of a symmetry between neutrons and protons, called isospin.

2.1.3 Isospin symmetry

The understanding of particle physics, or modern physics in general, is governed by symmetries [5]. The dynamical implications of symmetries were rationalized by Emmy Noether through the introduction of the relation to conservation laws: for every continuous symmetry, a conservation variable is generated - the inversion is also valid [12]. A prominent example of Noether's theorem associates the conservation of angular momentum to the isotropy of space, meaning the invariance of physical laws under rotation.

In the early days of atomic physics, two observations have led Heisenberg [13] to the assumption that there is an internal symmetry between a proton and the newly discovered neutron:

1. The similar level schemes of mirror nuclei (nuclei with interchanged number of protons and neutrons, e.g. $^{14}_{6}$C and $^{14}_{8}$O, see Figure 2.2)
2. The nearly identical masses of the proton and the neutron. Today, the deviation is measured to be less than 0.14% [1]:

$$\begin{aligned} m_p &= 938.27208816(29)\,\text{MeV} \\ m_n &= 939.56542052(54)\,\text{MeV} \end{aligned} \tag{2.1}$$

In this context, *internal* refers to the symmetry not being related to space or time, but rather to the characteristics of different particles. Drawing from these observations, Heisenberg concluded that the strong interaction would not distinguish between protons and neutrons.

Ignoring the electric charges and the minuscule difference in mass, the two particles are, in analogy to the already established spin, regarded as a two-state single-particle system called a *nucleon*. Denoting the proton p and neutron n as opposite states,

$$p = \begin{pmatrix} 1 \\ 0 \end{pmatrix} \quad \text{and} \quad n = \begin{pmatrix} 0 \\ 1 \end{pmatrix}, \tag{2.2}$$

the nucleon N can be defined as a vector in *isospin space* [1]

$$N = \begin{pmatrix} p \\ n \end{pmatrix}. \tag{2.3}$$

Following the formulation of the original two-state system of the spin, the nucleon carries isospin $+\frac{1}{2}$, and the third component I_3 has the eigenvalues $+\frac{1}{2}$ (proton) and $-\frac{1}{2}$ (neutron):

$$\begin{aligned} p &= \left| \frac{1}{2},\ +\frac{1}{2} \right\rangle, \\ n &= \left| \frac{1}{2},\ -\frac{1}{2} \right\rangle \end{aligned} \tag{2.4}$$

Protons are isospin-up states and neutrons isospin-down. With this notation, the assumed equivalence of the strong interaction towards protons and neutrons is understood as an invariance of the strong interaction under rotation in isospin space. A rotation of 180° around the first axis of isospin space transforms a proton into a neutron, and vice versa. If the strong force is invariant under rotation in isospin space, then according to Noether's theorem the isospin is conserved in all strong interactions.

The internal symmetry of the isospin is revealed when particles with otherwise different properties have similar masses, allowing them to be arranged in multiplets. The total isospin of a multiplet is given as

$$\text{multiplicity} = 2 \cdot I + 1, \tag{2.5}$$

since I_3 must range from $-I$ to $+I$, analogous to the spin formulation. For example, for the three pions, $I = 1$:

$$\begin{aligned} \pi^+ &= |1,\ +1\rangle, \\ \pi^0 &= |1,\ 0\rangle, \\ \pi^- &= |1,\ -1\rangle. \end{aligned} \tag{2.6}$$

The assignment of $+1$ and -1 is by convention, the 0 follows from the consideration of charge. The quartet of Δ baryons must carry $I = \frac{3}{2}$, and are defined as

$$\begin{aligned} \Delta^{++} &= \left| \frac{3}{2},\ +\frac{3}{2} \right\rangle, \\ \Delta^{+} &= \left| \frac{3}{2},\ +\frac{1}{2} \right\rangle, \\ \Delta^{-} &= \left| \frac{3}{2},\ -\frac{1}{2} \right\rangle, \\ \Delta^{--} &= \left| \frac{3}{2},\ -\frac{3}{2} \right\rangle. \end{aligned} \tag{2.7}$$

[1] To be precise, a two-component vector or *spinor*.

Historically, isospin was introduced to explain the symmetrical properties of proton and neutrons and later classified the multiplet structure of hadrons. With the emerging quark model, the concept of isospin was applied to the two lightest quarks, up and down, which form also form a doublet [15]:

$$\begin{aligned} u &= \left|\frac{1}{2}, +\frac{1}{2}\right\rangle, \\ d &= \left|\frac{1}{2}, -\frac{1}{2}\right\rangle. \end{aligned} \tag{2.8}$$

All other quarks carry zero isospin. This makes isospin symmetry a subset of the larger group of flavor symmetry. The invariance under rotations in isospin space is also known as charge independence and can be utilized to make predictions in dynamic processes. For instance, the relative cross sections of nn, np, and pp scattering can be determined solely from the charge independence of the strong interaction.

Hadrons with interchanged u and d quarks are referred to as isospin partners, such as the pairs of a charged and a neutral B meson:

$$\begin{aligned} B^+ &= \left|u\,\overline{b}\right\rangle \quad \longleftrightarrow \quad B^0 = \left|d\,\overline{b}\right\rangle \\ B^- &= \left|\overline{u}\,b\right\rangle \quad \longleftrightarrow \quad \overline{B}^0 = \left|\overline{d}\,b\right\rangle \end{aligned} \tag{2.9}$$

Following the symmetrical aspect, the masses of B^+ (B^-) and B^0 ($\overline{B}^0$) are almost identical:

$$\begin{aligned} m_{B^+} &= 5.27966(12)\,\mathrm{GeV}, \\ m_{B^0} &= 5.27934(12)\,\mathrm{GeV}. \end{aligned} \tag{2.10}$$

The difference of approximately 0.006% stems mostly from the marginally different quark masses of u and d.

While historically, isospin was thought to be invariant in strong interactions, it became clear that isospin is indeed not an exact symmetry of the strong force. However, given the small difference in the light quark masses, it is generally regarded as a *good* approximation of a symmetry [16]. In addition to the mass difference, the electromagnetic interaction contributes to further, occasionally significant, violation of isospin symmetry.

To conclude, isospin can be accepted as an approximate symmetry of the strong interaction. Assuming that isospin is conserved when modelling a process simplifies the calculation in many applications. However, there are processes in which a wide variety of effects are involved and modelling is not trivial. One of these cases is discussed in the next section.

2.2 Isospin Violation at $\Upsilon(4S)$ Threshold

The threshold production of the $\Upsilon(4S)$ resonance offers an excellent basis for studying B physics. The strongly decaying $\Upsilon(4S)$ produces pairs of B mesons. Due to charge conservation, this can only be a pair of differently charged B mesons, or a pair of neutral B mesons. A key characteristic for the $\Upsilon(4S)$ resonance is the ratio of the production rates of charged and neutral pairs. This section introduces the relevant physical parameters and outlines the relation to isospin. Various theoretical calculations attempting to model the decay of the $\Upsilon(4S)$ are discussed. It is demonstrated that various mechanisms with opposing effects make modeling isospin violation overly complex, and as a result, predicting the relationship between production rates is unreliable given the current state of knowledge.

2.2.1 $B\overline{B}$ pair production at B Factory

Accelerator experiments such as *BaBar*, *Belle*, and the successor *Belle II* are collider facilities known as B *factories* due to their operation at the center-of-mass energy of 10.58 GeV. This energy corresponds to the mass of the $\Upsilon(4S)$. The bottomonium resonance decays almost exclusively to a pair of $B\overline{B}$ mesons [1]:

$$\mathcal{B}\big(\Upsilon(4S) \to B\overline{B}\big) \ > \ 96\%, \tag{2.11}$$

at 95% confidence level. A lower bound for $f_{\not{B}} = \mathcal{B}\big(\Upsilon(4S) \not\to B\overline{B}\big)$ is obtained from the sum of measured $\Upsilon(4S)$ decays to lighter bb states and pions and given as [17]:

$$f_{\not{B}} \ > \big(0.264 \pm 0.021\big)\% \tag{2.12}$$

On account of conservation of energy, the $\Upsilon(4S)$ is only allowed to decay into a pair of the two lightest B mesons. For this, only two branching fractions must be considered:

$$\begin{aligned} f_{00} &= \mathcal{B}\big(\Upsilon(4S) \to B^0\overline{B}^0\big), \\ f_{\pm} &= \mathcal{B}\big(\Upsilon(4S) \to B^+B^-\big). \end{aligned} \tag{2.13}$$

Following the definition in Equation 2.9, the B mesons within one decay product pair are each the isospin partners of the other decay product pair. Consequently, given the almost identical masses of the isospin partners (Equation 2.10), the approximate symmetry of isospin would suggest an equal production rate, $f_{\pm} = f_{00}$. It has already been deduced that isospin is not globally conserved. In the process

$$e^+e^- \to \Upsilon(4S) \to B\overline{B}, \tag{2.14}$$

at a B factory, the limited phase space in the $\Upsilon(4S) \to B\overline{B}$ decay of a few MeV results in small B velocities, which parametrically enhance electromagnetic effects and thus isospin violation. This is further discussed in the next section. The magnitude of the breaking is expressed into the production asymmetry of the $\Upsilon(4S)$ to a charged or a neutral B meson pair:

$$R^{c/n} = \frac{f_{\pm}}{f_{00}}. \tag{2.15}$$

Due to this relation, measuring $R^{c/n}$ or equivalently f_{00}, allows for an interpretation of isospin violation at the $\Upsilon(4S)$ resonance.

In a world with conserved isospin symmetry, the production asymmetry would vanish and $R^{c/n} = 1$. The next section discusses various theoretical papers addressing the corrections of $R^{c/n}$ due to isospin violation.

2.2.2 Review of theoretical predictions of $R^{c/n}$

Neglecting isospin symmetry breaking, the $\Upsilon(4S)$ decay would produce B^+B^- and $B^0\overline{B}^0$ in equal amount, hence $R^{c/n} = 1$. This section summarizes theory calculations approaching corrections to the decay rate fraction, $\delta R^{c/n}$. The papers listed here are not exhaustive.

The breaking of isospin symmetry is generally regarded as small, due to the marginal difference in the already small masses of the up and down quarks, and the relatively weak coupling of the electromagnetic interaction. The threshold production by the $\Upsilon(4S)$ resonance gives rise to effects that influence the magnitude of the isospin violation. In particular, Coulomb corrections are parametrically enhanced by the low velocity of the resulting B mesons.

Different theoretical methodologies have been suggested to estimate the Coulomb effects in $\Upsilon(4S) \to B\overline{B}$ decays, yielding entirely divergent qualitative predictions regarding the magnitude of these effects. Initially, with point-like mesons, the corrections were estimated to be close to 20%, subsequent calculations using meson models and vertex structures lead to deviations in the single-digit percentage range. When the effects of the strong interaction are also taken into account, a prediction becomes almost impossible, as the corrections then depend substantially on additional assumptions.

Point-like mesons

The first theoretical approach to corrections to $R^{c/n}$ was undertaken by D. Atwood and W. Marciano in 1989 [18]. Their calculation will later be referred to as *textbook form*. Initially, the non-relativistic velocity of the B mesons produced near threshold is considered. The slow velocity of the B mesons,

$$\beta = \sqrt{1 - \frac{4m_B^2}{m_{\Upsilon(4S)}^2}} \simeq 0.065, \tag{2.16}$$

increases the possibility for electromagnetic interaction between B^+ and B^-.

To simplify the calculation, the $\Upsilon(4S)$ and B mesons are considered as point-like particles. It is argued that neglecting the hadronic structure is not a poor approximation, although it clearly misrepresents the low-energy spectrum. The result is obtained by solving the Schrödinger equation in a Coulomb potential for a P-wave final state. The calculation indicates that the Coulomb corrections enhance the B^+B^- production rate relative to $B^0\overline{B}^0$ by a factor

$$F_{\text{Coulomb}} = 1 + \frac{\pi\alpha}{2\beta} + \mathcal{O}(\frac{\alpha^2}{\beta^2}), \tag{2.17}$$

where α is the fine structure constant and β is as defined above. In first order, this results in a correction of $\delta R^{c/n} = 0.18$.

Meson and vertex structure

Shortly afterwards, G. Lepage [19] responded with his publication in 1990, arguing that the structure of the mesons should not be ignored. The Coulomb corrections were noted to be very sensitive to the structure of the $\Upsilon(4S)$ and B mesons. The decay amplitude T for $\Upsilon(4S) \to B\overline{B}$ without corrections reads

$$T_0 = \boldsymbol{\epsilon} \cdot \boldsymbol{p}_B \Phi(\mathbf{p_B}), \tag{2.18}$$

where $\boldsymbol{\epsilon}$ denotes the $\Upsilon(4S)$ polarization vector, $\boldsymbol{p}_B$ the momentum of the B meson and $\Phi(\mathbf{p_B})$ the function that parametrizes the vertex in the $\Upsilon(4S) \to B\overline{B}$ decay. To consider the meson and vertex structure, the amplitude is extended to include the electromagnetic form factor of the B mesons, the non-relativistic propagator for the B mesons during the time between the decay and the Coulomb interaction, and vertex functions, i.e. the amplitude for the $\Upsilon(4S)$ to decay into the B mesons:

$$\delta T = -e^2 \int \frac{\mathrm{d}^3\boldsymbol{q}}{(2\pi)^3} \frac{\left[f_B(\boldsymbol{q}^2)\right]^2}{\boldsymbol{q}^2} \frac{1}{\boldsymbol{p}_B^2/m - (\boldsymbol{p}_B + \boldsymbol{q})^2/m + i\epsilon} \epsilon \cdot (\boldsymbol{p}_B + \boldsymbol{q}) \Phi(\boldsymbol{p}_B + \boldsymbol{q}),$$

with the charge form factor $f_B(\boldsymbol{q}^2)$ in the first factor. The second factor is the nonrelativistic propagator for the B mesons for the time between decay and the electromagnetic interaction.

By replacing the form factors and the vertex function with their values at zero momentum,

$$\begin{aligned} F_{B^+} &= 1, \\ F_{B^0} &= 0, \\ \Phi(\boldsymbol{p}_B + \boldsymbol{q}) &= \Phi_0, \end{aligned}$$

the textbook form in Equation 2.17 is obtained.

Depending on the model for the vertex function, the enhancement is reduced from 18% to 4% or even turned into a 3% suppression of the production of charged B pairs relative to the neutral B pair. Notably, the vertex functions depend on the momentum of the B meson, which in turn depends on the centre-of-mass energy of the e^+e^- collision.

Strong interaction phase

The strong coupling of the resonance to the B meson pair has been neglected in the two previous approaches. The determination of strong effects on the isospin violation in $\Upsilon(4S) \to B\overline{B}$ is generally complicated, and several aspects of the strong force have been addressed by various authors.

Non-relativistic chiral perturbation theory has been used by R. Kaiser *et al.* (2003) [20] to obtain an estimate of $\delta R^{c/n}$. This effective theory of QCD addresses the strong interaction of B mesons at short distances, including the $B^*B\pi$ vertex and the coupled channels with pairs of pseudoscalar mesons. The B^*B system, although a phase-space forbidden channel of the $\Upsilon(4S)$ decay, must still be included in the calculation for this approach. The resulting correction of $R^{c/n}$ depends on the B^*B coupling and the isospin violating part of the $\Upsilon(4S)$ coupling to $B\overline{B}$ states.

M. Voloshin contributed several iterations of papers between 2003 and 2004, and again in 2018 [21, 22, 23, 24], which approached the theoretical value of $R^{c/n}$ by incorporating the non-resonant $I = 1$ state, such as the process $e^+e^- \to \rho^+\rho^- \to B\overline{B}$. Additionally, Dubynskiy *et al.* [25] calculated $R^{c/n}$ by considering both the isoscalar state $I = 0$, the resonant $e^+e^- \to \Upsilon(4S)$, and the isovector state $I = 1$. The principal conclusion to be drawn from these calculations is that the value of $\delta R^{c/n}$ undergoes a change in sign within a narrow range of the $\Upsilon(4S)$ decay width. The corrections to $R^{c/n}$ calculated with the strong interaction phase in consideration deviate significantly from Equation 2.17, where the sign and the amount of the deviation is to be explained by the finite size of the mesons and their scattering in the isovector state [24]. Consequently, the production asymmetry of B^+B^- and $B^0\overline{B}^0$ is heavily influenced by the centre-of-mass energy of the e^+e^- collision.

2.3 Experimental Perspectives

Experimentally, it is advantageous to measure a ratio. If the related variables are appropriately selected, a number of systematic effects potentially cancel out. For this reason, an attempt was made to determine $R^{c/n}$ first. Subsequently, $f_\pm$ and f_{00} can be inferred on the basis of an assumption about the decay rate of $\Upsilon(4S) \to B\overline{B}$.

2.3.1 Measurements of $R^{c/n}$

In the early 2000s, the *CLEO*, *BaBar* and *Belle* experiments carried out numerous measurements of $R^{c/n}$. The trade-off for measuring this ratio, which is easier to determine experimentally, is that certain assumptions have to be made. The quantities that are to be extracted from experimental data are the number of charged and neutral B, $N(B^+)$ and $N(B^0)$, respectively. The B mesons decay into specific final states x, denoted as $B^+ \to x^+$ and $B^0 \to x^0$. The final states are related by isospin, that is, they consist of isopartners as defined in subsection 2.1.3.

Transposing the ratio in Equation 2.15 to include $N(B^+)$ and $N(B^0)$ in the equation gives

$$\begin{aligned} R^{c/n} = \frac{f_\pm}{f_{00}} &= \frac{\Gamma\big(\Upsilon(4S) \to B^+B^-\big)}{\Gamma\big(\Upsilon(4S) \to B^0\overline{B}^0\big)} \\ &= \frac{N(B^0)}{\epsilon(B^0)}\frac{\epsilon(B^+)}{N(B^+)} \cdot \frac{\mathcal{B}\big(B^+ \to x^+\big)}{\mathcal{B}\big(B^0 \to x^0\big)} \\ &= \frac{N(B^0)}{\epsilon(B^0)}\frac{\epsilon(B^+)}{N(B^+)} \cdot \frac{\Gamma\big(B^+ \to x^+\big)}{\Gamma\big(B^0 \to x^0\big)}\frac{\tau(B^+)}{\tau(B^0)}, \end{aligned} \tag{2.19}$$

where Γ indicates the decay rate, ϵ the reconstruction efficiency, τ the lifetime. The following assumptions are now required for the extraction of $R^{c/n}$:

1. The lifetime ratio $\frac{\tau(B^+)}{\tau(B^0)}$ has to be assumed from other measurements.
2. The decay rates of $B^+ \to x^+$ and $B^0 \to x^0$ are assumed to be equal, in order for them to cancel out in the ratio. This is justified by the fact that

Experiment	Method	$R^{c/n}$	$\tau(B^+)/\tau(B^0)$	Ref.
CLEO (2001)	$B \to J/\psi\ K$	$1.04 \pm 0.07 \pm 0.04$	1.066 ± 0.024	[28]
BaBar (2002)	$B \to J/\psi\ K$	$1.10 \pm 0.06 \pm 0.05$	1.062 ± 0.029	[29]
CLEO (2002)	$B \to D^*\ \ell\nu$	$1.058 \pm 0.084 \pm 0.136$	1.074 ± 0.028	[30]
Belle (2003)	$B \to \ell\ell$	$1.01 \pm 0.03 \pm 0.09$	1.083 ± 0.017	[31]
BaBar (2004)	$B \to J/\psi\ K$	$1.006 \pm 0.036 \pm 0.031$	1.083 ± 0.029	[29]
BaBar (2005)	$B \to c\bar{c}\ K$	$1.06 \pm 0.02 \pm 0.03$	1.086 ± 0.017	[32]
Belle (2023)	$B \to J/\psi\ K$	$1.065 \pm 0.012 \pm 0.019 \pm 0.047$	1.076 ± 0.004	[33]

Table 2.1: List of measurements of $R^{c/n}$ from different methods with the assumed lifetime ratio. Each measurement of $R^{c/n}$ listed here assumes isospin symmetry so that the decay rates of the B mesons cancel out. The values of $R^{c/n}$ are presented with statistical and systematic uncertainties. The most recent *Belle* measurement assign the assumption on isospin symmetry with an additional uncertainty.

the two decays, both in the initial and final states, differ only by one up and one down quark. In other words, with assumed isospin symmetry in the B decays, $\Gamma\big(B^+ \to x^+\big) = \Gamma\big(B^0 \to x^0\big)$

With these, Equation 2.19 the actual quantity measured in these analyses is

$$R^{c/n} \frac{\tau(B^0)}{\tau(B^+)} = \frac{N(B^0)}{\epsilon(B^0)} \frac{\epsilon(B^+)}{N(B^+)}. \tag{2.20}$$

The ratio of decay rates $\Gamma\big(B^+ \to x^+\big)/\Gamma\big(B^0 \to x^0\big)$ could not have been taken from external experiments, because its measurement depends on the knowledge of $R^{c/n}$ itself [26]. Therefore, a theoretical calculation of the ratio would be the only alternative to the isospin approximation, which, however, would decrease the accuracy.

As described in subsection 2.2.2, a theoretical prediction of $R^{c/n}$ is generally very complicated, and the results and accuracy of these calculations do not match the experimental results so far [27]. For this reason, many analyses have attempted to measure $R^{c/n}$. A list of the most prominent ones using the isospin assumption is given in Table 2.1 and are represented in Figure 2.3. A frequently chosen channel is $B \to J/\psi\, K$, including the excited state of the K meson. This channel is suitable since the weakly decaying B meson produces an isosinglet state and an isotriplet state, the J/ψ and the K, respectively.

The most recent average of $R^{c/n}$ calculated by HFLAV is obtained by fitting to the global average of individual measurements of $R^{c/n}$, the one direct measurement of f_{00} (described in the next section, see Equation 2.27) and the constraint in Equation 2.25, and yields

$$R^{c/n}_{\text{HFLAV 2021}} = 1.057^{+0.024}_{-0.025}, \tag{2.21}$$

a value different from unity by 2.2σ [17].

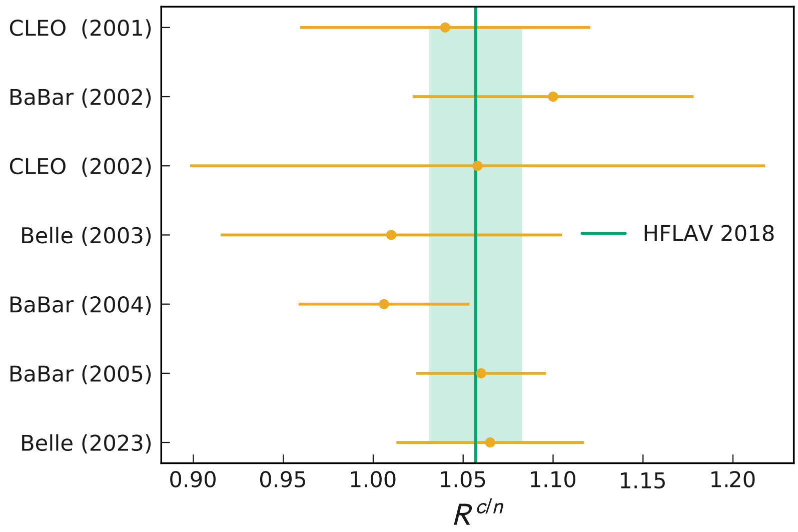

Figure 2.3: The published values of $R^{c/n}$ as listed in Table 2.1. The values show excellent consistency.

2.3.2 Measurements of f_{00}

In principle, two contrasting approaches exist for determining f_{00}. Either $R^{c/n}$ can be measured first, followed by the deduction of f_{00}, or f_{00} can be measured directly. In the following, both approaches are described, beginning with the indirect measurement.

From an experimental perspective, measuring the ratio $R^{c/n}$ first, is more convenient and has been done in numerous analyses (see Table 2.1). In order to obtain f_{00} from $R^{c/n}$, an additional assumption is necessary, besides the assumptions already made regarding the lifetimes of the B mesons and the isospin symmetry in the B decays: the contribution of decays to the total decay rate of the $\Upsilon(4S)$. The PDG evaluation [1], along with numerous other publications, assumes that the $\Upsilon(4S)$ decays entirely into a pair of BB mesons, either charged or neutral:

$$\mathcal{B}\big(\Upsilon(4S) \to B\overline{B}\big) = 1, \tag{2.22}$$

or equivalently

$$f_{\pm} + f_{00} = 1. \tag{2.23}$$

With this assumption, the published values of $R^{c/n}$ in Table 2.1 are employed to determine

$$f_{00} = \frac{1}{1 + R^{c/n}} \tag{2.24}$$

and listed in Table 2.2.

In its latest publication in 2021 [17], HFLAV refined this assumption and takes non-$B\overline{B}$ decays into consideration. Thus, Equation 2.23 reads

$$f_{\pm} + f_{00} + f_{\not{B}} = 1, \tag{2.25}$$

where $f_{\not{B}} = 0.00264 \pm 0.00021$ is assumed to be equal to the upper limit given in Equation 2.12. The averages for $R^{c/n}$, f_{00} and $f_{\pm}$ calculated based on this

Experiment	$R^{c/n}$	f_{00}	$f_{\pm}$
CLEO (2001)	1.040 ± 0.081	0.490 ± 0.019	0.510 ± 0.019
BaBar (2002)	1.100 ± 0.078	0.476 ± 0.018	0.524 ± 0.018
CLEO (2002)	1.058 ± 0.160	0.486 ± 0.038	0.514 ± 0.038
Belle (2003)	1.010 ± 0.095	0.498 ± 0.023	0.502 ± 0.023
BaBar (2004)	1.006 ± 0.048	0.499 ± 0.012	0.501 ± 0.012
BaBar (2005)	1.060 ± 0.036	0.485 ± 0.008	0.515 ± 0.008
Belle (2021)	1.065 ± 0.081	0.484 ± 0.019	0.516 ± 0.019
HFLAV 2018	$\mathbf{1.058 \pm 0.024}$	$\mathbf{0.486 \pm 0.006}$	$\mathbf{0.514 \pm 0.006}$
HFLAV 2021	$\mathbf{1.057^{+0.024}_{-0.025}}$	$\mathbf{0.485^{+0.006}_{-0.011}}$	$\mathbf{0.512^{+0.006}_{-0.016}}$

Table 2.2: Values of $f_{00} = 1/(1 + R^{c/n})$ and $f_{\pm} = 1 - f_{00}$ derived from $R^{c/n}$ measurements listed in Table 2.1 with total uncertainty on $R^{c/n}$ given by $\sqrt{\sigma^2_{\text{stat}} + \sigma^2_{\text{syst}}}$. The last two rows represent the averages calculated by HFLAV in 2018[34] and 2021[17], respectively. The 2018 value is also listed in the *Review of Particle Physics 2023* [1]. The difference between the two averages is that the latter incorporates $\Upsilon(4S)$ decays to non-$B\overline{B}$ states, as detailed in Equation 2.25. Common to both averages is the inclusion of the *BaBar* measurement of f_{00}.

redefined assumption is listed in Table 2.2. In this, the positive error of $f_{\not{B}}$ is set to infinity.

To date, only one direct measurement of f_{00} has been performed. The analysis described in this thesis represents the second such measurement. The first measurement of f_{00} was carried out at the *BaBar* experiment in 2005 [2]. The method applied in this analysis is developed by the *MARK III Collaboration* for a measurement of $\psi(3770)$ [35] and is based on double-tagged $\Upsilon(4S)$ decays, i.e. both B mesons are reconstructed. More on this method and its application is detailed in section 5.1.

The feature utilized in this method is that in the counting equations of single-tag and double-tag candidates, the $\Upsilon(4S) \to B^0\overline{B}^0$ branching fraction contributes linearly, whereas the single-tag and double-tag decay rates contribute quadratically. This enables the dependence on the decay rates in the ratio of the number of single-tag candidates squared to the number of double-tag events to be dropped, while the dependence on f_{00} remains.

The presence of double-tag events requires a relatively large amount of data, but the method allows f_{00} to be extracted without assuming isospin symmetry or knowledge of B lifetimes.

The *BaBar* measurement of f_{00} does not encompass the entire integrated luminosity of 424.2 fb^{-1} collected by the detector, only a small fraction of 81.7 fb^{-1}. The overall experimental setup with PEP-II, an asymmetric-energy e^+e^- collider, and the omnipurpose *BaBar*-detector at the intersection, is comparable to KEKB and the *Belle*-detector. Details on the similarities and differences of the experiments are found in [36].

The branching fraction of interest is extracted from the single-tag and double-tag samples by

$$f_{00} = \frac{C N_{\mathrm{s}}^2}{4 N_{\mathrm{d}} N_{B\overline{B}}}, \tag{2.26}$$

where $N_{\mathrm{s}}(N_{\mathrm{d}})$ denotes the number of selected single-tag (double-tag) candidates, $N_{B\overline{B}}$ the total number of $B\overline{B}$ events in the data sample and $C = \epsilon_{\mathrm{d}} \,/\, \epsilon_{\mathrm{s}}^2$ the ratio of double-tag reconstruction efficiency and the square of single-tag reconstruction efficiency. The ratio of efficiencies is determined from simulation to be $C = 0.995 \pm 0.008$. This is explicitly stated at this point, as it differs significantly from the observation of the *Belle* measurement described in this dissertation.

The obtained value is reported to be

$$f_{00} = 0.486 \pm 0.010(\mathrm{stat}) \pm 0.008(\mathrm{syst}). \tag{2.27}$$

The total statistical and systematic uncertainty amounts to 2.63%, with the dominant source being the total number of $B\overline{B}$, contributing 1.13%.

2.3.3 Significance for future measurements

Accurate determination of the absolute branching fractions of charged and neutral B meson decays is essential for flavour physics, influencing the measurements of the SM parameters of and potential sensitivity to new physics. The *Belle* and *BaBar* experiments combined have recorded more than $1\,\mathrm{ab}^{-1}$ of integrated luminosity at the $\Upsilon(4S)$ resonance. The currently operating *Belle II* experiment is expected to increase this by a factor of 50 [37].

The resulting reduction in statistical uncertainty means that systematic effects will become more and more dominant. A significant systematic uncertainty remains the ratio of $\Upsilon(4S)$ decays to B^+B^- and $B^0\overline{B}^0$.

The recently published *Belle II* measurement of $|V_{cb}|$ using $\overline{B}^0 \to D^{*+}\ell\overline{\nu}_\ell$ [38] evaluated the uncertainty off f_{00} to be the second-highest systematic uncertainty, behind the efficiency to correctly identify a slow pion.

Since the measurement of $R^{c/n}$ depends on the knowledge of the B lifetimes and the assumption on isospin symmetry, a direct measurement of f_{00} and $f_\pm$ is preferable. In particular, f_{00} has already been measured using the *BaBar* data set, even though only a fraction of the existing sample has been utilized so far.

$f_\pm$, on the other hand, has not been measured directly before. This is due to neutral slow pions in the signal channel $B^+ \to D^{*0}(\to D^0\pi^0)\ell^+\overline{\nu}_\ell$, a final state with low reconstruction efficiency, which is not sufficient for a direct measurement with the existing data sets. However, the accuracy of $f_\pm$ is also improved by measuring f_{00} alone.

Chapter 3

The Belle Experiment

The *Belle* experiment was specifically designed to study B mesons. The *Belle* detector, installed at the only intersection of the KEKB storage rings, collected data from 1999 to 2010. The highly successful operation eventually only shut down to make way for an overall upgrade, the successor experiment Belle II, which finally took data again in 2018. This chapter summarizes the instrumentational setup and the experimental complex at *The High Energy Accelerator Research Organization*, commonly known as *KEK*, in Tsukuba, Japan. The information is gathered from [36], [39] and [40].

3.1 B factories

Due to their design and primary objective, generating and effectively reconstructing an immense amount of B mesons, the high energy particle physics experiments *Belle* and *BaBar* are commonly referred to as B factories. Unlike other experiments also incorporating a physics program targeting at B physics, the data samples recorded in a B factory contain B meson pairs embedded in a relatively clean environment. This cleanliness is a result of the choice of the initial particles that are brought into collision. B factories are electron-positron colliders operating at the $\Upsilon(4S)$ resonance, with a center-of-mass energy of $\sqrt{s} = 10.58\,\mathrm{GeV}$.

As explained in subsection 2.2.1, the phase space available in the decay of a $\Upsilon(4S)$ provides only enough to produce a pair of B^+B^- or $B^0\overline{B}^0$ mesons, no excited states of B mesons are possible. Precisely, a $\Upsilon(4S)$ generated in a e^+e^- collision decays into one of these two pairs in over 96% of cases [1]. These types of accelerators therefore ensure a clean sample of B mesons with no QCD contamination, as is the case in hadron colliders. The process producing the $B\overline{B}$ pairs is depicted in the Feynman diagram in Figure 3.1.

The data recorded at the $\Upsilon(4S)$ resonance is split into two separate samples: the SVD1 sample with $140\,\mathrm{fb}^{-1}$ and the SVD2 sample accounting for $571\,\mathrm{fb}^{-1}$, corresponding to different configurations of the Silicon Vertex Detector, as explained in subsection 3.3.1.

To broaden its scope, the *Belle* experiment not only focused on operating at

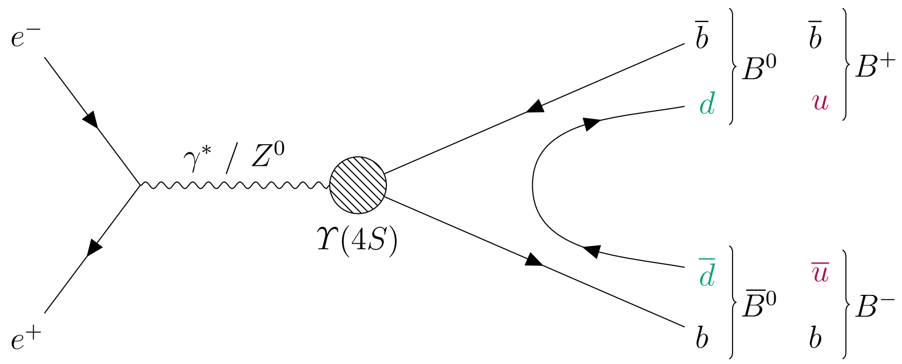

Figure 3.1: A feynman diagram of the $B\overline{B}$ pair production at a B factory. The mediating photon or Z^0 boson decays to a bottomonium state, the $\Upsilon(4S)$ resonance. Color confinement triggers the formation of an additional quark-antiquark pair, leading to the creation of two mesons. Neutral mesons are formed by a $d\bar{d}$ pair, while charged mesons result from a $u\bar{u}$ pair.

the center-of-mass energy corresponding to the $\Upsilon(4S)$ resonance. It also collected resonance data from other bottomonium states such as $\Upsilon(5S)$ or $\Upsilon(2S)$. In addition, scans were performed around these respective resonances to analyze the continuum region. In total, *Belle* collected on-resonance data amounting to $866\,\text{fb}^{-1}$ and $122\,\text{fb}^{-1}$ of off-resonance. The Υ mass spectrum is shown in Figure 3.2.

Parallel to the operation of *Belle*, the *BaBar* collaboration also conducted experiments on a B-factory [41]. Both *Belle* and *BaBar* had the same physics objectives and used comparable detector designs and analytical approaches. This parallel effort proved advantageous as it allowed cross-verification and comparison of experimental results between the two projects.

Belle ceased data collection in 2010 to enable the transition to the upgraded *Belle II* experiment and the enhanced accelerator complex, Super-KEKB. This upgrade aims to increase the total integrated luminosity by a factor of 50 [37]. *Belle II* recorded its initial collisions in April 2018 and to date has collected almost $500\,\text{fb}^{-1}$. [42]

3.2 KEKB accelerator

The beams of electrons and positrons are provided by the accelerator complex called KEKB [40]. At first, positrons are generated in a fixed-target scattering of electrons on tantalum. Subsequently, the electrons and the generated positrons are accelerated to their final energy in a linear accelerator, after which they are injected into storage rings measuring 3 km in circumference, traveling in opposite directions. A scheme with additional information is shown in Figure 3.3.

The requirements for the accelerator resulting from the physical programme for investigating CP violation in the B meson system include:

1. High luminosity: The measurement of time-dependent CP asymmetry demands for an enormous amount of data. The branching fraction for one of

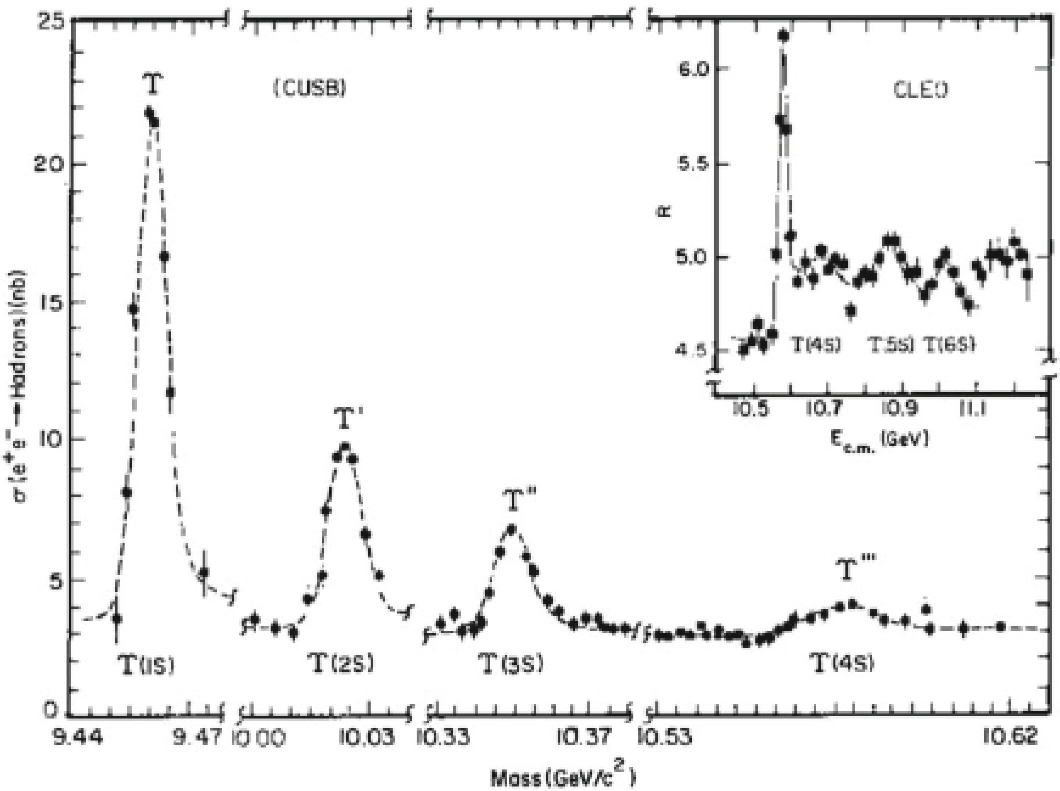

Figure 3.2: Cross sections for hadron production as a function of center-of-mass energy, recorded at earlier experiments CUSB and CLEO [43]. Four distinct peaks are observable, labeled in ascending order as $\Upsilon(1S)$, $\Upsilon(2S)$, $\Upsilon(3S)$ and $\Upsilon(4S)$. The *Belle* experiment generally operates at the $\Upsilon(4S)$ resonance, which emerges the least prominently from the continuum.

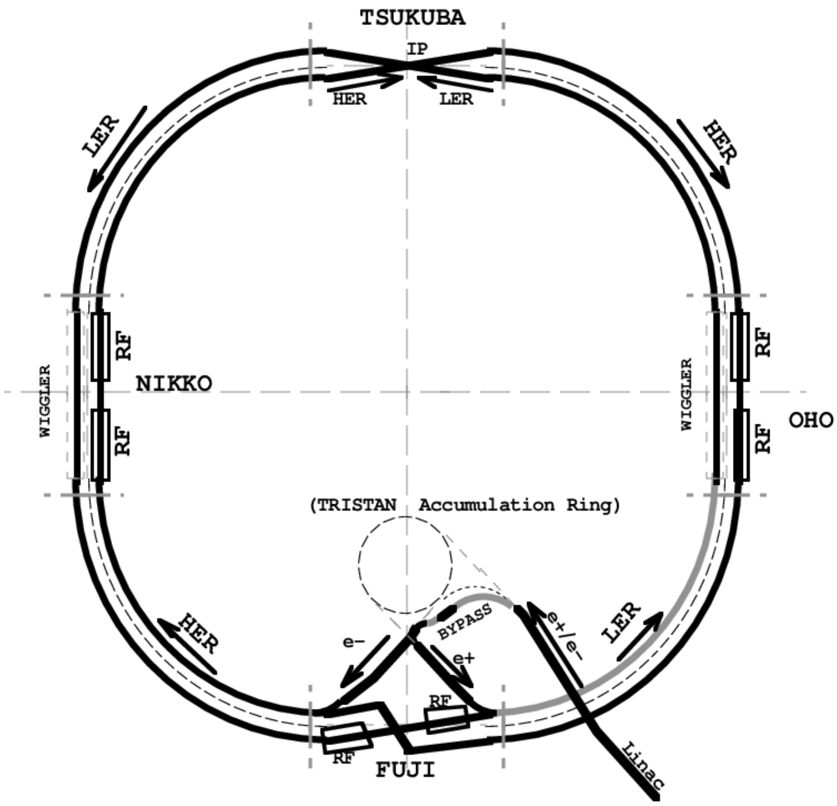

Figure 3.3: The KEKB accelerator complex [44]. Electrons and positrons are accelerated in a linear collider (*Linac*) and subsequently injected to circulate clockwise in the *High Energy Ring* (HER, electrons) and counter-clockwise in the *Low Energy Ring* (LER, positrons). Radiofrequency cavities (RF) and wigglers stabilize the beam conditions and compensate for energy loss from synchrotron radiation. At the interaction point (IP) the beams are brought to collision, surrounded by the *Belle* detector (not shown).

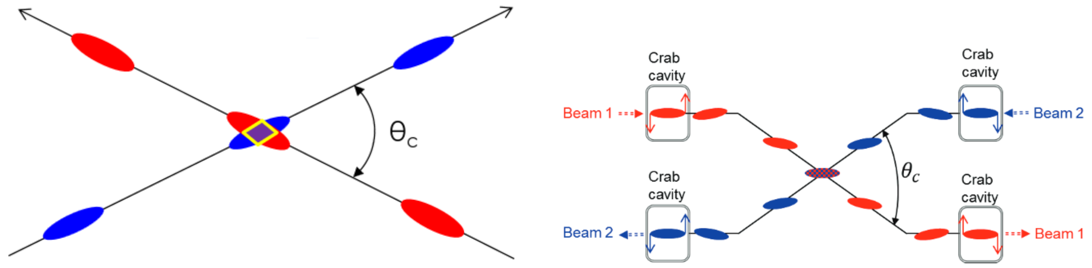

Figure 3.4: Bunch crossing without (left) and with Crab cavities (right) [45]. The transverse kick provided by the Crab cavities increases the overlap of the bunches, maximizing the number of collisions per bunch crossing.

the most important decays for measuring time-dependent CP asymmetry is $\mathcal{B}\big(B^0 \to J/\psi(\to \ell^+\ell^-)K_S^0\big) = 4.8 \cdot 10^{-5}$.

2. Boosted center-of-mass system: To ensure that the decay length of the B^0 and $\overline{B}^0$ mesons is resolvable in the laboratory system, the whole center-of-mass system is required to be boosted.

The second requirement is fulfilled by colliding electrons and positrons of unequal initial energies: the electrons stored in the *High Energy Ring* (HER) are accelerated to 8 GeV, while the positrons in the *Low Energy Ring* (LER) are accelerated to 3.5 GeV. This provides the center-of-mass system, i.e. the $\Upsilon(4S)$, with a boost of

$$\beta\gamma = \frac{E(e^-) - E(e^+)}{\sqrt{s}} = 0.425, \tag{3.1}$$

in reference to the laboratory system.

To adhere to the first requirement, one technical solution is the utilization of Crab cavities [45]. Particles circulate in bunches around the storage rings, and the objective is to maximize collisions between these particles. Crab cavities serve to adjust the orientations of the beam bunches so that they intersect head-on, as shown in Figure 3.4. This, combined with other measures, enabled reaching a peak luminosity of $2.1 \times 10^{34}\,\mathrm{cm^{-2}s^{-1}}$, surpassing the original design goal by more than double.

3.3 Belle detector

The *Belle* detector belongs to the category of omnipurpose detectors [39]. Generally, the detector system comprises a combination of various subdetectors, stacked in layers and shaped like a cylinder, with detectors filling the two ends, known as endcaps, to achieve an almost 4π coverage. The two beams run along the cylinder axis in a beam pipe. The beams intersect at a point that is not at the center of the detector, to account for the asymmetric energy.

The requirements for the individual components are determined by the physics program of B factories. The essential necessities are as follows:

- High acceptance: Nearly 4π coverage with sensitive detector material around the intersection point.
- Light material for the inner detector: The beam pipe, made of beryllium with a cooled channel between inner and outer walls, minimizes material in terms of radiation length, reducing multiple scattering and energy loss for particles crossing the beam pipe.
- Vertexing capability: Accurate measurement of CP-violating asymmetries requires precise determination of the decay vertex of each B meson in an event. The necessary resolution of $\sim 100\,\mu$m must be reached in both the beam direction and in transverse plane.
- Particle identification: To classify particles over a broad momentum range, multiple identification technologies are necessary. The *Belle* drift chamber is capable to identify tracks of even low momentum particles and accurately measures energy loss. This capability is augmented with a Time-Of-Flight system and Cherenkov detector for high momentum particles.
- Electromagnetic calorimetry: Precise information about the energy of both electrons and neutral particles is required.
- Trigger system: A reliable mechanism for registering events of interest to the physics programme in the shortest possible time.

A key component within the detector, apart from the individual subdetectors, is the superconducting solenoid which provides a homogeneous magnetic field with a strength of 1.5T. As the field lines are parallel to the beam pipe, charged particles are forced on a circular trajectory within the x, y-plane. The radius of curvature is essential for momentum determination. A schematic representation of the longitudinal and transverse cross-section of the *Belle* detector is shown in Figure 3.5. The geometry definitions are

- z-axis is parallel to e^+ beam and points in opposite direction of e^+ beam
- y-axis points from origin to center of the storage ring
- x-axis conforms to right-handed orthogonal coordinate system
- polar angle θ is the angle with respect to the z-axis
- azimuthal angle ϕ is the angle in (x, y)-plane
- $r = x^2 + y^2$ is the distance from origin in the (x, y)-plane

The following chapter provides an overview of the primary components of the detector, from the innermost to the outermost subdetector.

3.3.1 Silicon Vertex Detector

The Silicon Vertex Detector (SVD) [46]is installed to meat the requirement of the accurate knowledge of decay vertices and is the innermost subdetector. It existed in two configurations, SVD1 and SVD2. The latter was an upgrade aimed at addressing issues encountered with the former. The measurement described in this

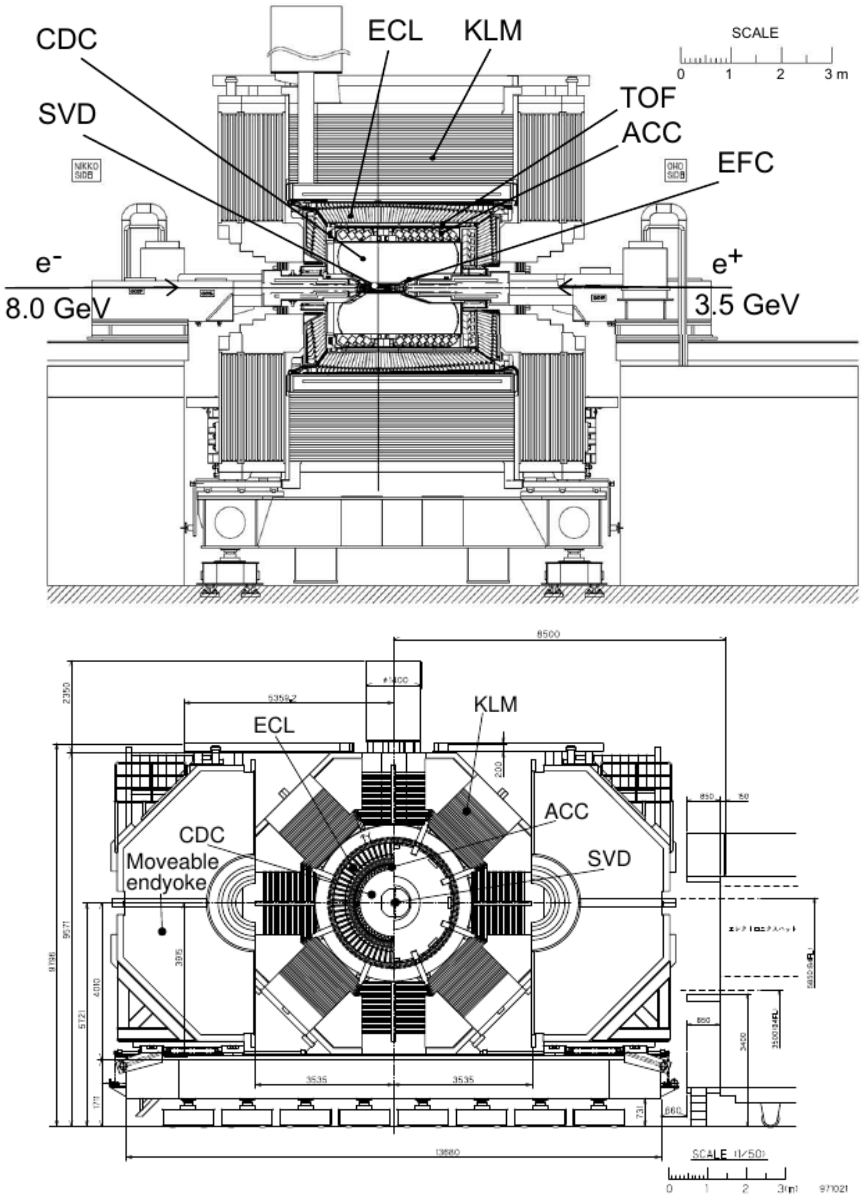

Figure 3.5: Longitudinal (top) and transverse (bottom) cross section of the *Belle* detector [36]. The subdetectors are: SVD (Silicon Vertex Detector), CDC (Central Drift Chamber), ACC (Aerogel Cherenkov Counters), TOF (Time-Of-Flight), ECL (Electromagnetic Calorimeter), EFC (Extreme Forward Calorimeter), KLM (K_L^0 and Muon Detector).

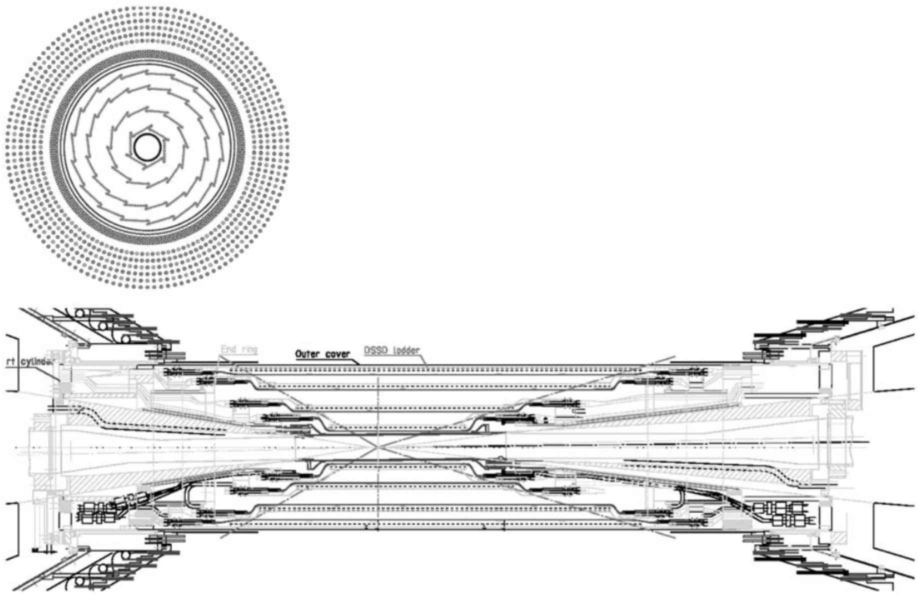

Figure 3.6: Silicon Vertex Detector in the SVD2 configuration. The top scheme shows the transverse cross section with four layers of DSSDs. The bottom scheme depicts the longitudinal cross section, showing a progressively increasing length of sensitive coverage from one layer to the next. [36]

thesis analyzes data obtained using the SVD2 setup, thus only this configuration is described.

The core elements are double-sided silicon detectors (DSSD), arranged in 4 layers. The layers are arranged in such a way that the full angular acceptance of ($17° < \theta < 150°$) is covered, depicted in Figure 3.6.

Silicon detectors are capable of detecting traversing charged particles. Through ionization, electron-hole pairs are generated within the *pn* junction of a silicon detector. These are then directed towards readout electronics by applying a voltage to the depletion region.

As the sensors on both sides are perpendicular to each other, $r - \phi$ information can be derived. The arrangement in layers makes it possible to track the motion of the particles.

3.3.2 Central Drift Chamber

The detector that cylindrically surrounds the SVD is called the Central Drift Chamber (CDC) [47]and fulfills multiple crucial functions:

1. Reconstruction of charged particle tracks (*tracking*), accurate determination of their hit coordinates within the detector volume, and facilitation of momentum reconstruction.

2. Particle identification through $\mathrm{d}E/\mathrm{d}x$ measurements within its gas volume. Additionally, low-momentum tracks, which may not reach the particle identification system, can still be identified solely through the CDC.

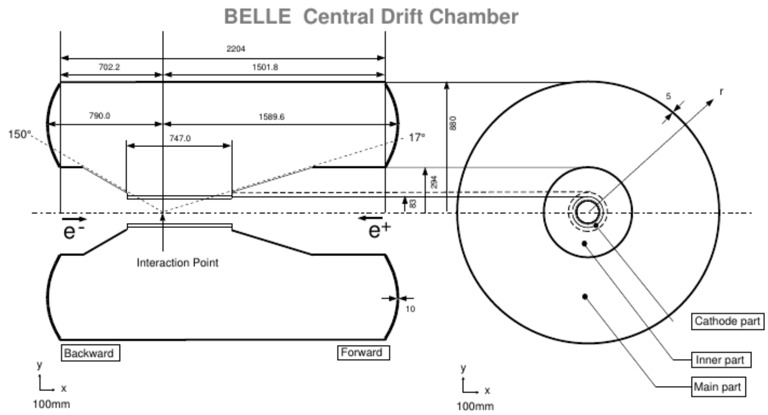

Figure 3.7: Structure of the Central Drift Chamber. The left scheme shows a longitudinal cross section (asymmetric coverage), the right scheme depicts the transverse cross section [36].

3. Providing trigger signals for charged particles.

Charged particles passing through a gaseous medium produce electrons and ions by ionization. Anode and cathode wires passing through the chamber attract the electrons and ions, producing an electrical signal. The time it takes the electrons to drift to the anode and their drift speed in the medium allows the position of the particles to be determined.

The CDC is asymmetric in the z-direction to account for the boost of the center-of-mass system. The coverage is the same as for the SVD, ($17° \leq \theta \leq 150°$). The chamber consists of 50 cylindrical layers with a mix of axial and small-angle stereo layers. In total the CDC has 8400 drift cells. In combination with the cathode strips, the stereo-layers allow for the z-position measurement of the traversing particle. The structure of the CDC is depicted in Figure 3.7.

Crucial information for particle identification is obtained from the measurement of the energy loss, $\mathrm{d}E/\mathrm{d}x$ of charged particles. The Bethe-Bloch formula [48] relates energy loss in matter to the speed of the particle. Utilizing this formula along with momentum measurement allows for deducing the particle type by calculating its mass.

3.3.3 Aerogel Cherenkov Counters

The subdetector enclosing the CDC is a system called Aerogel Cherenkov Counters (ACC) [49] and consist of a barrel and an endcap region as depicted in Figure 3.8. and provides additional discrimination between charged particles, particularly between pions and kaons. The distinctive information is obtained from Cherenkov radiation, detected in photomultiplier tubes.

Charged particles passing through a dielectric medium, such as aerogel, at a speed faster than the phase velocity of light in the medium v_{aerogel}, polarize the medium. The polarized molecules quickly return to their normal state, emitting photons in the process. The condition under which these Cherenkov photons are emitted

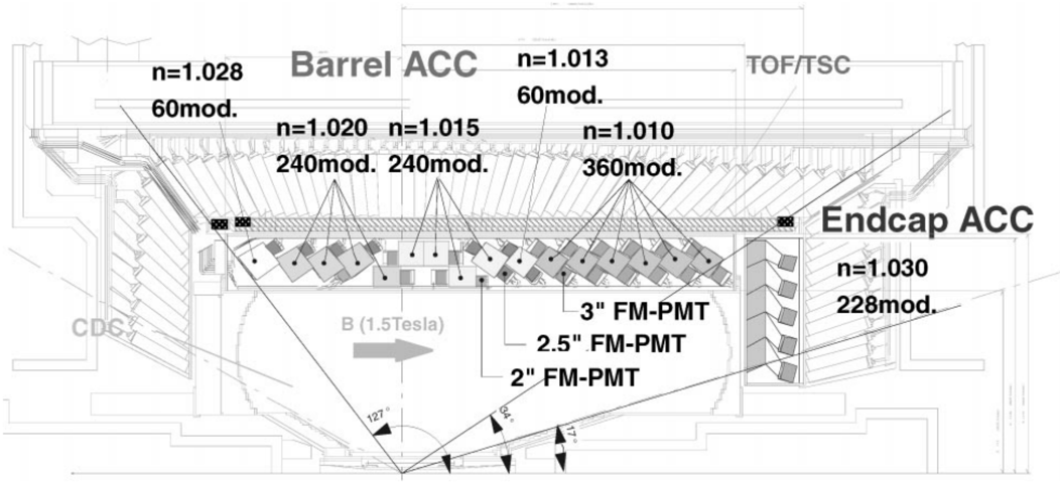

Figure 3.8: Schematic view of the Aerogel Cherenkov Counters subdetector [49]. The refractive indices of the barrel modules range from 1.010 to 1.028, whereas the endcap is equipped with $n = 1.030$. The asymmetric design of the experiment is considered in the arrangement.

relates the particle's speed v to the refractive index n of the medium,

$$\beta = \frac{v}{c} > \frac{c_{\text{aerogel}}}{c} = \frac{1}{n}. \tag{3.2}$$

The refractive indices of the aregol range from 1.010 to 1.028 for the barrel modules, the endcap has $n = 1.030$. With this setup, the ACC achieves $K - \pi$ separation for particles with momenta between 1.2 to 3.5 GeV.

3.3.4 Electromagnetic Calorimeter

The energy of particles such as electrons, positrons or photons is measured using calorimeters. When electromagnetically interacting particles enter the calorimeter, they trigger particle showers. This is a cascading process involving bremsstrahlung and pair production. The number of scintillation photons created in the showering process is proportional to the energy deposit of the entering particle.

The *Belle* detector consists of two calorimeters. The main subdetector is the Electromagnetic Calorimeter (ECL) [39], covering the barrel region and parts of the forward and backward endcap, as depicted in Figure 3.9. The ECL consists of 8763 individual crystals in which the particle shower is released. Photomultiplers then detect the scintillation photons. Dividing the crystals into multiple segments offers additional information about the location of the energy deposit. The spatial coverage of the ECL of $17° \leq \theta \leq 150°$ is only partly interrupted at the junction of the barrel region and the endcaps. The ECL can measure a wide range of energy levels spanning several orders of magnitude, with its resolutions of 4% at 100 MeV to 1.6% at 8 GeV. By taking the ratio E/p, the energy measured in the ECL is crucial for distinguishing between electrons and hadrons.

The region around the beam pipe ($6.4° \leq \theta \leq 11.5°$) that is not covered by the ECL is equipped with another calorimeter, the Extreme Forward Calorimeter

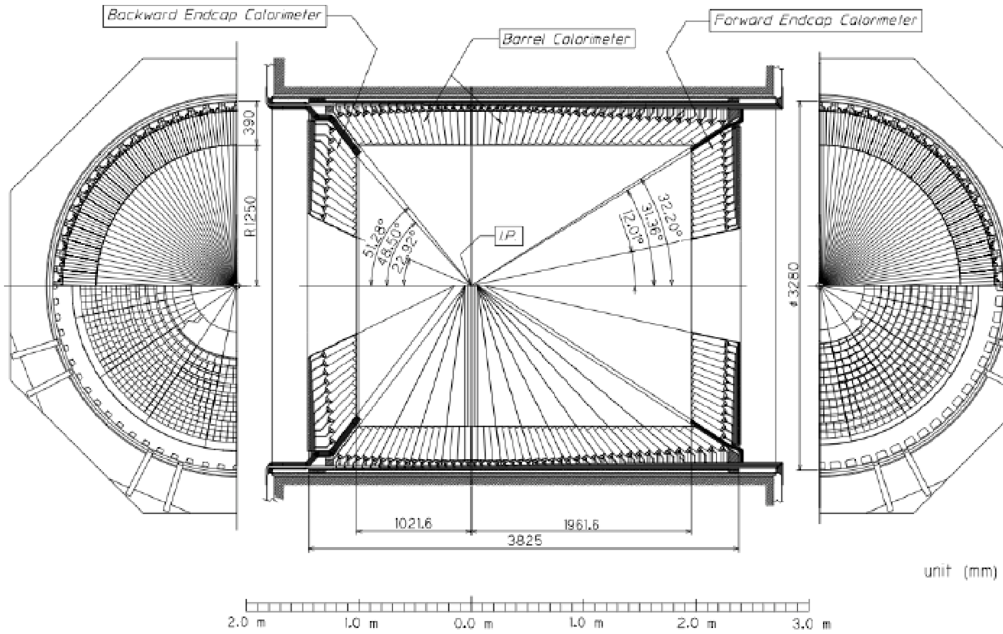

Figure 3.9: The Electromagnetic Calorimeter [36]. The center scheme shows the longitudinal cross section, left and right are halves of the transverse cross section. The ECL covers the barrel region as well as parts of both endcaps.

(EFC). The function of the EFC is different from the ECL. The purpose of the EFC is to supply data for measuring instantaneous luminosity and machine background. The criteria for the crystals in the EFC are also different, due to the significantly higher radiation levels in this extreme region.

3.3.5 Time-Of-Flight system

The $K-\pi$ separation of the ACC and CDC is complemented by the Time-Of-Flight (TOF) [50] for it provides information to distinguish kaon and pion tracks with momenta below 1.2 GeV. The minimum momentum required to reach the TOF is 0.28 GeV. This subdetector measures the time it takes a particle to travel from the interaction point to one of the 128 plastic scintillator counters of the TOF. Moreover, the TOF equips the trigger system with timing signals. Specifically, the TOF signal steers the readout of the ECL and the CDC.

3.3.6 K_L^0 and Muon Detector

The K_L^0 and Muon Detector (KLM) [51] constitutes the outermost and largest individual component of the detector. As the name suggests, the KLM detects neutral long-lived kaons and muons. The detector is a system of alternating layers of stopping material and sensitive material, laid out in 8 components in the barrel region and two end caps.

Iron plates with a thickness of 4.7 cm serve as interacting material. K_L^0 mesons trigger showers of ionizing particles in the plates and in the ECL. The detection of

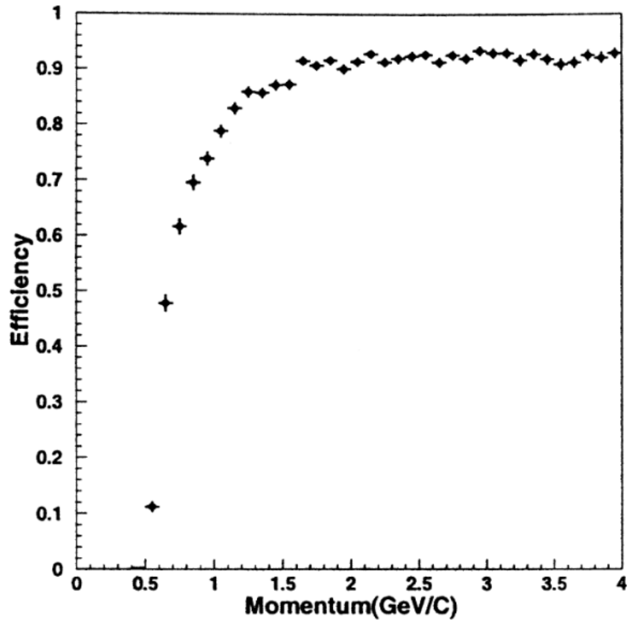

Figure 3.10: Muon identification efficiency vs momentum for a likelihood cut of 0.66 [52].

these shower particles is the only registered information about K_L^0. Muons, which interact relatively weakly, do not produce showers but instead leave hits in the resistive plate electrodes situated between the iron plates. In contrast, hadrons, which interact more strongly with the iron, traverse fewer layers of the KLM. By combining this information with the hits recorded in the CDC, it becomes possible to differentiate between muons and hadrons.

The efficiency of muon identification increases with momentum, where the minimum transverse momentum necessary to reach the KLM being 600 MeV. For particles with momenta larger than 1.5 GeV, distribution of efficiency is approximately constant, as depicted in Figure 3.10.

3.4 Particle identification

The *Belle* detector is designed to identify particles that are either stable or have a sufficiently long lifetime to ensure that they do not decay before passing through the detector volume. These particles are collectively referred to as final state particles (FSP), and comprise the list of $e^{\pm}$, $\mu^{\pm}$, $K^{\pm}$, p, $\overline{p}$, γ and K_L^0.

Charged particles leave hits in the tracking detectors SVD and CDC and energy deposit in the ECL. The curvature of the tracks, combined with the measurement of $\mathrm{d}E/\mathrm{d}x$, enables the identification of the particle's type. In addition, particularly pions and kaons are discriminated with information from TOF and ACC.

Typically, the identification of neutral FSPs is more challenging. Neutral particles decaying into two photons produce characteristic V shaped energy clusters in the ECL.

Eventually, the likelihood of different particle hypotheses is expressed as likelihood ratios $\mathcal{L}$. The specifics of electron likelihood determination is found in [53], and for muons in [54].

Chapter 4

Data Samples and Analysis Software

This chapter provides an overview of the key components integral to the analysis presented in this note. It includes a description of the analysis software used, the experimental data acquired by the Belle detector, and the simulated data, including both the generic Belle MC samples and privately generated signal samples. The chapter concludes with a detailed description of the various types of corrections applied to the generic Belle MC samples, explaining in detail the steps taken to achieve the most accurate representation of the real data.

4.1 Analysis software

The analysis of the data is carried out with the *Belle II Analysis Software Framework*, in short `BASF2` [55]. This analysis is based on the version `release-06-01-08` with some privately implemented contributions, explained in section 5.6.

The generic MC samples described in section 4.3 were generated by the *Belle* collaboration using the *Belle Analysis Software Framework*. In order to analyze the data with `BASF2`, the Belle data are converted into a format that can be processed by the new software framework. This is done using the `B2BII` package [56] from `BASF2`.

4.2 Recorded data samples

This analysis relies on the on-resonance data captured by the Belle detector using the upgraded SVD configuration (SVD2) from 2003 to 2008. Following an overhaul in early 2003, the SVD was installed in its revised version, so only SVD2 data is analyzed. The data was collected in distinct data acquisition periods, typically spanning several months. These so-called *experiments* are identified by numerical labels, and the experiments used for this measurement (31 to 65) are listed in Table 4.1.

In total, the offline integrated luminosity comprises $\mathcal{L} = 571.15\,\mathrm{fb}^{-1}$. Given the

exp. no.	$\mathcal{L}$ [fb^{-1}]	$N_{B\overline{B}} \times 10^6$	collection period
31	17.725	19.7	2003 (Oct – Dec)
33	17.508	19.3	2004 (Jan – Feb)
35	16.691	18.5	2004 (Feb – Mar)
37	60.909	67.2	2004 (Mar – Jul)
39	41.157	47.1	2004 (Sep – Dec)
41	58.752	64.0	2005 (Jan – Apr)
43	56.206	61.6	2005 (Apr – Jun)
45	12.946	14.4	2005 (Sep – Oct)
47	37.205	41.2	2005 (Nov – Dec)
49	27.024	29.7	2006 (Jan – Mar)
51	39.237	41.9	2006 (Apr – Jun)
55	72.088	80.2	2006 (Sep – Dec)
61	34.095	37.4	2007 (Oct – Dec)
63	32.858	35.6	2008 (Feb – Apr)
65	37.751	41.8	2008 (Apr – Jun)
31 – 65	571.15	619.62	2003 – 2008

Table 4.1: Luminosity, the measured number of $B\overline{B}$ pairs and the date of recording for the distinct experiments as well as the total data sample. [57]

SVD upgrade altered the performance in both tracking and particle detection, only the data collected with the SVD2 configuration is used, as integration of SVD1 data would require further management of systematic uncertainties.

Experiments with physical data are numbered odd, the even numbered experiments are runs for testing, calibration and similar and are not intended for ordinary analyses. The experiments with number 53, 57 and 59 recorded off-resonance data and are hence not used in this measurement.

4.3 Simulated data samples

Monte Carlo data, abbreviated as MC, refers to simulated data samples created using Monte Carlo generators [58]. Hadronic events such as $e^+e^- \rightarrow \Upsilon(4S)$ and continuum events from $e^+e^- \rightarrow q\overline{q}$, where $q\overline{q}$ denotes $u\overline{u}$, $d\overline{d}$, $s\overline{s}$, or $c\overline{c}$, are simulated using the `EvtGen` package [59]. The fragmentation and hadronization of quarks are modeled by the `Jetset` generator within the `PYTHIA` package [60]. Additionally, the emission of radiative photons originating from final states is simulated with *PHOTOS* [61].

Subsequently, the interactions between the particles resulting from the generated collisions and the Belle detector are simulated with the help of the `GEANT 3` package [62]. After detector simulation, MC data mirrors actual recorded data, enabling comparative analysis using the same tools at every analysis step.

The *Belle* collaboration offers extensive datasets encompassing a comprehensive range of B meson decay processes. These datasets, referred to as generic Belle

MC, are employed in this analysis. To mitigate statistical uncertainties in the analysis of simulated decays, the MC samples are generated with an integrated luminosity that is ten times greater than the recorded data from the experiment. A simulated sample of equivalent size to the recorded data is referred to as stream. The generic Belle MC is divided into samples of different event types: the generic $B \to c$ events, split into charged and neutral B pairs, and the continuum events comprising non-$B\overline{B}$ events.

For the purpose of developing and validating ntuple MC-truth variables, a special MC sample that contains only signal events is produced. Detailed information about the truth matching variables and the necessity for a dedicated MC sample is elaborated in section 5.6. Two separate signal MC datasets are produced: single-tag and double-tag events, both consisting of 100 000 events for each of them. The single-tag sample contains only true single-tag events, i.e. all events have one and only one B^0 decaying through the signal channel.

4.4 MC corrections

Multiple advancements have been made in both the accuracy of measured quantities and the refinement of physical models since the production of the original Belle MC data. However, due to the extensive time and resources required to generate a large-scale data set, it is not feasible to directly incorporate the latest achievements in particle physics into the simulation of this analysis. Furthermore, differences between data and MC exist in numerical values, such as the number of events or the efficiency of reconstructing a particular final state particle. These values were reviewed in later studies and in some cases improved.

To overcome these issues, a technique that rescales the event weight is implemented on the existing generic MC. This technique applies weights to simulated events for the following aspects, with the goal of achieving the closest possible alignment between the experimental data and simulation.

Data-MC difference:

- slow pion reconstruction efficiency
- lepton identification
- luminosity scaling

Updated physics parameters:

- branching fractions for $B \to X_c \ell \nu_\ell$ decays
- form factor model parametrization for $B \to X_c \ell \nu_\ell$ decays

where X_c represents the charmed mesons D, D^* and D^{**}. The notation D^{**} is commonly used in particle physics and denotes the four orbitally excited mesons D_1, D_1', D_2^* and D_0^*, see Figure 4.1 Further elaboration on the correction procedures

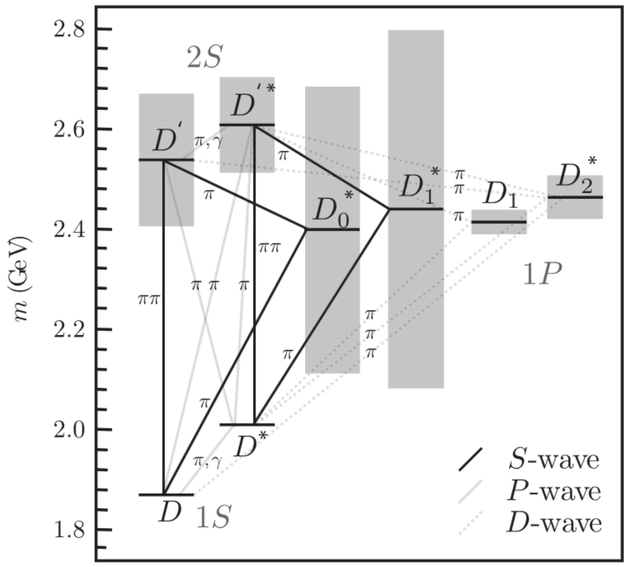

Figure 4.1: The orbitally excited D mesons, commonly referred to as D^{**} [63]. Represented are the masses and decay widths. The lines linking the states indicate decays via the strong interaction. The $1P$ states are made up of two spin-doublets: the broad states D_0^* and D_1', and the narrow states D_1 and D_2^*.

is provided in the subsequent sections. The influence of the corrections is reported in section 7.2.

4.4.1 Slow pion efficiency

Discrepancies in the reconstruction efficiencies stem from inaccuracies in simulating particle interactions with the detector material and providing an inaccurate description of the detector response. As described in section 5.2, B signal candidates are formed by combining a lepton and a charged pion. The lepton possesses a relatively high momentum, for which the efficiency is adequately modeled. However, the charged pion has a momentum in the center-of-mass frame of

$$p_{\mathrm{cms}}(\pi) < 200\,\mathrm{MeV}, \tag{4.1}$$

which prevents it from reaching the two of the three sub-detectors for particle identification, ACC and TOF. Slow pions may only reach the CDC. More details on particle identification is found in section 3.4.

The reconstruction efficiency difference in data and MC is studied in detail in [64]. The outcome of the study, weights in bins of the pion momentum, are listed in Table 4.2. These weights were determined through a systematic investigation of low momentum tracks from $B^0 \to D^{*-}\pi^+$ decays. The signal yields from experimental data were compared to MC samples using a 2-dimensional fit applied to the distribution of $(\Delta E, \Delta m)$. The resultant weights are normalized to the highest momentum bin. Every B^0 candidate is allocated the weight corresponding to the momentum of the slow pion, allowing for multiple corrections for an event depending on the number of B^0 candidates present.

$p_{\text{lab}}(\pi)$ [GeV]	weight	σ_{uncorr}	σ_{corr}	σ_{syst}
0.050 – 0.075	0.832	0.070	0.009	0.001
0.075 – 0.100	0.930	0.027	0.010	0.001
0.100 – 0.125	0.967	0.021	0.010	0.000
0.125 – 0.150	0.984	0.017	0.010	0.000
0.150 – 0.175	1.009	0.016	0.011	0.000
0.175 – 0.200	1.008	0.018	0.011	0.000
> 0.200	1.000	0.018	0.011	0.000

Table 4.2: Correction weights and its uncertainties for the slow pion reconstruction efficiency for different ranges of pion momentum in the lab-frame [64].

The corrections ρ_π listed in Table 4.2 are provided with an uncorrelated and a correlated statistical uncertainty, $\sigma_{\text{stat}}^{\text{uncorr}}$ and $\sigma_{\text{stat}}^{\text{corr}}$ respectively, and an additional correlated systematic uncertainty $\sigma_{\text{syst}}^{\text{corr}}$,

$$\rho_\pi(i) \pm \sigma_{\text{stat}}^{\text{uncorr}}(i) \pm \sigma_{\text{stat}}^{\text{corr}}(i) \pm \sigma_{\text{syst}}^{\text{corr}}(i), \tag{4.2}$$

for the index i represents one of the six momentum bins. The evaluation of systematic uncertainties due to correcting for the slow pion efficiency is given in subsection 8.1.1.

4.4.2 Lepton identification efficiency and fake rate

Two aspects of particle identification give rise to differences in data and MC: firstly, the efficiency of particle identification; and secondly, the rate at which non-leptonic particles are misidentified as leptons.

The inherent particle identification efficiency (PID) within the simulation may deviate from the actual efficiency observed in the experimental data. To quantify the discrepancy for electron and muon PID between data and MC, leptons are reconstructed from the high purity sample of $e^+e^- \rightarrow e^+e^- \ \ell^+\ell^-$ in [65].

The correction factors provided depend on 6 bins of particle identification selection criterion, 10 momentum bins and 7 polar angle regions of the particle track. For each of these bins, correction factors are calculated as the ratio between the efficiencies derived from MC and data. The corrections determined in [65] are determined in the purely leptonic decay $e^+e^- \rightarrow e^+e^- \ \ell^+\ell^-$. Since the weights are intended to be applied to leptons originating from B meson decays, the results of the study are validated by examining $B \rightarrow X J/\psi (\rightarrow \ell^+\ell^-)$ events to determine the effect of the hadronic environment.

Considering the fake rate of leptons, the results provided in [66] are used. Similar to true lepton correction explained above, fake rate correction factors are determined in bins of momentum and polar angles.

For the true lepton correction factors, the statistical uncertainty among different kinematic bins is independent, while the systematic uncertainties are assumed to be fully correlated. The uncertainties on the fake rate corrections factors are also correlated among different bins. The evaluation of the systematic uncertainties due to correcting for lepton PID is given in subsection 8.1.2.

4.4.3 Event scaling

The number of generated events in the MC samples do not match the number in the data. To correct for this, we rescale the number of generated events by applying the following weights w independent for neutral (B^0) and charged (B^-) pairs of B mesons, charmed (c) and light-quark (uds) continuum events:

$$w(B^0) = \frac{N^{\mathrm{data}}_{B\bar{B}} \cdot f_{00}}{N^{\mathrm{MC}}_{B^0\bar{B}^0}}, \tag{4.3}$$

$$w(B^-) = \frac{N^{\mathrm{data}}_{B\bar{B}} \cdot (1 - f_{00})}{N^{\mathrm{MC}}_{B^+B^-}}, \tag{4.4}$$

$$w(c) = \frac{N^{\mathrm{data}}_{B\bar{B}} \cdot \sigma_c}{\sigma_{B\bar{B}} \cdot N^{\mathrm{MC}}_{c}}, \tag{4.5}$$

$$w(uds) = \frac{N^{\mathrm{data}}_{B\bar{B}} \cdot \sigma_{uds}}{\sigma_{B\bar{B}} \cdot N^{\mathrm{MC}}_{uds}}. \tag{4.6}$$

Here, $N^{\mathrm{data}}_{B\bar{B}}$ represents the measured number of $B\bar{B}$ events in data [67], while N^{MC} corresponds to the number of generated events in the generic MC samples [68]. The term $f_{00} = \mathcal{B}\big(\Upsilon(4S) \to B^0\bar{B}^0\big) = 0.486 \pm 0.006$ [1] denotes the branching fraction for $\Upsilon(4S)$ decays into $B^0\bar{B}^0$ pairs.

Additionally, the cross-sections used to generate the MC samples are incorporated through $\sigma_{B\bar{B}} = 1090\ \mathrm{pb}^{-1}$, $\sigma_{uds} = 2090\ \mathrm{pb}^{-1}$ and $\sigma_c = 1300\ \mathrm{pb}^{-1}$ [69]. These weights allow us to rescale the event yields appropriately, ensuring consistency between the MC samples and the data.

4.4.4 Branching fractions

To account for improved measurements of the branching fractions of processes relevant for this analysis, we update the values by calculating event weights. Specifically, the processes under considerations involve events of the form $B \to X_c\ell\nu$, where X_c represents the charmed mesons D, D^* and D^{**}, as previously defined.

The calculation of weights involves categorizing events based on the true underlying decays of the B mesons involved. For each B meson in an event that is decaying into one of the modes, a weight w_{BFR} for correcting the branching fraction is calculated as

$$w_{\mathrm{BFR}} = \frac{\mathcal{B}_{\mathrm{updated}}\big(B \to X_c\ell\nu\big)}{\mathcal{B}_{\mathrm{MC}}\big(B \to X_c\ell\nu\big)}, \tag{4.7}$$

where $\mathcal{B}_{\mathrm{updated}}\big(B \to X_c\ell\nu\big)$ denotes the updated branching fraction for the respective decay mode, and $\mathcal{B}_{\mathrm{MC}}\big(B \to X_c\ell\nu\big)$ represents the branching fraction in the original Belle MC. Consequently, if both B mesons in an event decay into one of the modes, two weights are applied to the event accordingly.

The branching fractions are updated to the values based on the averages calculated by the Heavy Flavor Averaging Group (HFLAV, [17]). These are the most precise branching fraction determinations. To reduce the uncertainties on the values even further, the results of the branching fraction measurements of the neutral $B^0 \rightarrow X_c^- \ell^+ \nu$ and charged $B^+ \rightarrow X_c^0 \ell^+ \nu$ decays can be combined if one assumes isospin symmetry.

Two approaches are employed for the calculation of isospin-weighted averages of branching fractions. The first approach is applied to the decays $B \rightarrow D\ell\nu$ and $B \rightarrow D^*\ell\nu$, while the second is used for $B \rightarrow D^{**}\ell\nu$.

Approach 1: $B \rightarrow D\ell\nu$ and $B \rightarrow D^*\ell\nu$

The branching fraction of particle P to final state f is formulated theoretically as

$$\mathcal{B}\left(P \rightarrow f \right) = \frac{\Gamma\left(P \rightarrow f\right)}{\Gamma\left(P \rightarrow \text{all}\right)} = \Gamma\left(P \rightarrow f\right) \cdot \tau_X, \tag{4.8}$$

where Γ denotes the decay rate and τ the lifetime. The postulate of isospin symmetry implies that the decay rates are equivalent, hence

$$\Gamma\left(B^0 \rightarrow X_c^- \ell^+ \nu\right) = \Gamma\left(B^+ \rightarrow X_c^0 \ell^+ \nu\right). \tag{4.9}$$

Consequently, assuming isospin symmetry between neutral and charged B mesons, it can be deduced that the disparity in branching fractions arises solely from variations in the lifetimes of the B mesons. This relationship is derived from Equation 4.8 and Equation 4.9, and when solved for the branching fraction of charged B mesons, it can be expressed as

$$\mathcal{B}\left(B^+ \rightarrow X_c^0 \ell^+ \nu \right) = \mathcal{B}\left(B^0 \rightarrow X_c^- \ell^+ \nu \right) \cdot \frac{\tau_{B^+}}{\tau_{B^0}}. \tag{4.10}$$

The ratio of lifetimes is provided by HFLAV as $\frac{\tau_{B^+}}{\tau_{B^0}} = 1.076 \pm 0.004$ [17]. In order to compute the isospin-averaged branching fractions, it is necessary to determine the weights v_B^0 and v_B^+ in

$$\overline{\mathcal{B}}_{B^+} = v_B^+ \cdot \left(\mathcal{B}(B^+ \rightarrow X_c^0 \ell^+ \nu\right) + v_B^0 \cdot \left(\mathcal{B}(B^0 \rightarrow X_c^- \ell^+ \nu) \cdot \frac{\tau_{B^+}}{\tau_{B^0}}\right). \tag{4.11}$$

To improve clarity, the following substitutions are introduced:

$$\mathcal{B}_{B^+} := \mathcal{B}(B^+ \rightarrow X_c^0 \ell^+ \nu) \tag{4.12}$$

$$\mathcal{B}_{B^0} R_\tau := \mathcal{B}(B^0 \rightarrow X_c^- \ell^+ \nu) \cdot \frac{\tau_{B^+}}{\tau_{B^0}}, \tag{4.13}$$

so that Equation 4.11 reads

$$\overline{\mathcal{B}}_{B^+} = v_B^+ \cdot \mathcal{B}_{B^+} + v_B^0 \cdot \mathcal{B}_{B^0} R_\tau. \tag{4.14}$$

Decay	$\mathcal{B}$(HFLAV) $\times 10^{-2}$	v_B^+	w_{B^-}	$\mathcal{B}$(isospin) $\times 10^{-2}$
$B^0 \to D^-\ell^+\nu_\ell$	$2.31 \pm 0.04 \pm 0.09$	0.56	0.44	2.2396 ± 0.0664
$B^+ \to D^0\ell^+\nu_\ell$	$2.35 \pm 0.03 \pm 0.09$			2.4098 ± 0.0709
$B^0 \to D^{*-}\ell^+\nu_\ell$	$5.06 \pm 0.02 \pm 0.12$	0.27	0.73	5.1137 ± 0.1082
$B^+ \to D^{*0}\ell^+\nu_\ell$	$5.66 \pm 0.07 \pm 0.21$			5.5023 ± 0.1146

Table 4.3: Isospin-averaged branching fractions for $B \to D\ell\nu$ and $B \to D\ell\nu$. The input values for the averaging are provided by HFLAV [17]. The variance weights v_B^0 and v_B^+ are applied in Equation 4.11. The last column gives the isospin-averaged branching fractions used for the reweighting of MC.

The variance weights v_B^0 and v_B^+ are derived from the inverse of the covariance matrix

$$C = \begin{pmatrix} \sigma(\mathcal{B}_{B^+})^2_{\text{stat.}} + \sigma(\mathcal{B}_{B^+})^2_{\text{syst.}} & \rho \cdot \sigma(\mathcal{B}_{B^+})_{\text{syst.}} \cdot \sigma(\mathcal{B}_{B^0} R_\tau)_{\text{syst.}} \\ \rho \cdot \sigma(\mathcal{B}_{B^+})_{\text{syst.}} \cdot \sigma(\mathcal{B}_{B^0} R_\tau)_{\text{syst.}} & \sigma(\mathcal{B}_{B^0} R_\tau)^2_{\text{stat.}} + \sigma(\mathcal{B}_{B^0} R_\tau)^2_{\text{syst.}} \end{pmatrix}, \quad (4.15)$$

where it is assumed that the measurements are uncorrelated, hence the correlation coefficient $\rho = 0$ and the off-diagonal entries vanish, so that the calculation of variance weights is reduced to

$$v_B^+ = \frac{C^{-1}_{0,0}}{C^{-1}_{0,0} + C^{-1}_{1,1}} \quad (4.16)$$

$$v_B^0 = \frac{C^{-1}_{1,1}}{C^{-1}_{0,0} + C^{-1}_{1,1}}. \quad (4.17)$$

Table 4.3 summarizes the values for the isospin averaging of the branching fractions.

Approach 2 : $B \to D^{**}\ell\nu$

The method for averaging the branching fractions for decays involving D^{**} mesons is different, and this approach follows the procedure described in [70]. The issue is due to the fact that only the product branching ratios

$$\mathcal{B}\big(\, B \to D^{**}(\to D^*\pi^+)\ell^+\nu \,\big) = \mathcal{B}\big(\, B \to D^{**}\ell^+\nu \,\big) \times \mathcal{B}\big(\, D^{**} \to D^*\pi^+ \,\big) \quad (4.18)$$

have been measured experimentally. Therefore, the total D^{**} branching fractions have to be implied from the partial branching fractions. This calculation is only feasible when assuming isospin symmetry for the decays of the D mesons. This assumption, in particular, provides the isospin factors f_π for 2-body and $f_{\pi\pi}$ for 3-body pion decays, expressed as

$$f_\pi = \frac{\mathcal{B}\big(\, D^{**} \to D^{(*)}\pi^+ \,\big)}{\mathcal{B}\big(\, D^{**} \to D^{(*)}\pi \,\big)} = \frac{2}{3} \quad (4.19)$$

$$f_{\pi\pi} = \frac{\mathcal{B}\big(\, D^{**} \to D^{(*)}\pi^+\pi^- \,\big)}{\mathcal{B}\big(\, D^{**} \to D^{(*)}\pi\pi \,\big)} = \frac{1}{2} \pm \frac{1}{6}. \quad (4.20)$$

Assumptions for pure 3-body decays and intermediate decays states are covered by the uncertainty of 1/6. The denominators encounter all decays, e.g.

$$\mathcal{B}\big(\, D^{**} \to D^{(*)}\pi \,\big) = \mathcal{B}\big(\, D^{**} \to D^{(*)}\pi^{+} \,\big) + \mathcal{B}\big(\, D^{**} \to D^{(*)0}\pi^{0} \,\big). \tag{4.21}$$

The factor then is derived from the square of the matrix elements that describe the transition of these processes.

The decays $B \to D_0^*\ell^+\nu$ and $B \to D_1'\ell^+\nu$ only have one distinct 2-body decay mode each: $D\pi$ and $D^*\pi$ respectively. The average partial branching fractions calculated by HFLAV [17] are

$$\mathcal{B}\big(\, B^+ \to D_0^{*0}(\to D^+\pi^-)\ell^+\nu \,\big) = (0.28 \pm 0.03 \pm 0.04) \cdot 10^{-2} \tag{4.22}$$

$$\mathcal{B}\big(\, B^+ \to D_1^{\prime 0}(\to D^+\pi^-)\ell^+\nu \,\big) = (0.28 \pm 0.06) \cdot 10^{-2} \tag{4.23}$$

where for the latter, only two of the three reported values are considered for the variance weighted average since one measurement is incompatible. In combination with the isospin factor f_π, the total branching fractions can be determined as

$$\mathcal{B}\big(\, B^+ \to D_0^*\ell^+\nu \,\big) = \mathcal{B}\big(\, B^+ \to D_0^*(\to D^-\pi^+)\ell^+\nu \,\big) \cdot \frac{1}{f_\pi} = (0.42 \pm 0.08) \cdot 10^{-2}, \tag{4.24}$$

$$\mathcal{B}\big(\, B^0 \to D_0^*\ell^+\nu \,\big) = \frac{\mathcal{B}\big(\, B^+ \to D_0^*\ell^+\nu \,\big)}{\tau_{B^+}/\tau_{B^0}} = (0.39 \pm 0.07) \cdot 10^{-2} \tag{4.25}$$

and

$$\mathcal{B}\big(\, B^+ \to D_1^{\prime 0}\ell^+\nu \,\big) = \mathcal{B}\big(\, B^+ \to D_1^{\prime 0}(\to D^-\pi^+)\ell^+\nu \,\big), \cdot \frac{1}{f_\pi} = (0.28 \pm 0.06) \cdot 10^{-2} \tag{4.26}$$

$$\mathcal{B}\big(\, B^0 \to D_1^{\prime 0}\ell^+\nu \,\big) = \frac{\mathcal{B}\big(\, B^+ \to D_1^{\prime 0}\ell^+\nu \,\big)}{\tau_{B^+}/\tau_{B^0}} = (0.42 \pm 0.09) \cdot 10^{-2}. \tag{4.27}$$

No further decay modes undergo corrections for their branching fractions. Additionally, it is important to note that this analysis does not account for the so-called *gap*, which refers to the discrepancy between the sum of the branching fractions of the exclusive decay modes of $B \to X_c\ell\nu$ and the inclusive branching fraction.

4.4.5 Form factor models

In the description of weak decays involving $b \to c\ell\overline{\nu}_\ell$ transitions, the hadronic matrix elements for the weak currents are parametrized by form factors [71] A comprehensive overview of heavy-quark symmetry, the effective theory forming the basis for the description is found in [72], more details on form factors in [73].

Since the initial production of the original MC sample, significant advancements have been made in the modeling of the decay kinematics for semileptonic B decays involving D mesons. To incorporate these improvements, the existing models are updated by applying appropriate weights to each event associated with either one or two decays of the type $B \to D\ell\nu_\ell$, $B \to D^*\ell\nu_\ell$ or $B \to D^{**}\ell\nu_\ell$.

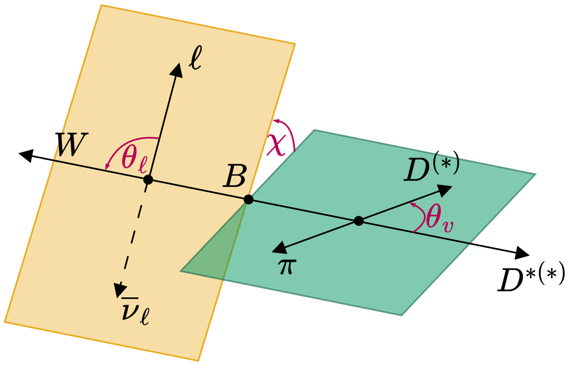

Figure 4.2: The helicity angles θ_l, θ_V and χ describe the decay kinematics of $B \to D^*\ell\nu_\ell$ and $B \to D^{**}\ell\nu_\ell$.

The choice of the form factor model only applies to the kinematic properties of the decay. The model on its own has no influence on the branching fraction. Therefore, only the shape of kinematic distributions is affected by the form factor corrections. Due to the reconstruction efficiency being correlated with the kinematic variables, the corrections impact the normalization, whereas on generator level the normalization is conserved, as can be seen for example in Figure 4.4.

The correction of form factor models is based on weights that are derived from kinematic variables that describe the decay. The variables are defined in the following.

The kinematics of any B decay involving a D, D^* or D^{**} is defined by recoil w, the product of the 4 velocities of the B and D mesons:

$$w = v_B \cdot v_D = \frac{m_B^2 + m_D^2 - q^2}{2m_B m_D}, \tag{4.28}$$

where v is the 4-velocity, m the mass of the meson, and $q = p_B - p_D$ the difference of the 4-momenta of B and D.

The decay $B \to D\ell\nu_\ell$ is solely described by w. In addition to w, the decays $B \to D^*\ell\nu_\ell$ and $B \to D^{**}\ell\nu_\ell$ are also a function of the helicity angels θ_l, θ_V and χ.

These angles describe the shape of the decays and are defined as

$$\begin{aligned} \theta_l &: \text{angle between } \ell \text{ and the virtual } W \text{ boson in rest frame of the } W\text{boson}, \\ \theta_V &: \text{angle between charmed meson and its first daughter}, \\ &\quad\ \text{in the rest frame of } D^{*(*)}\text{boson}, \\ \chi &: \text{angle between the } W \text{ boson decay plane and the } X_c \text{ decay plane}. \end{aligned} \tag{4.29}$$

A representation of the decay including the angles is given in Figure 4.2.

Model update 1: $B \to D\ell\nu_\ell$ and $B \to D^*\ell\nu_\ell$

The form factor parametrization of Caprini, Lellouch and Neubert (CLN) [74] was used to generate the decays $B \to D\ell\nu_\ell$ and $B \to D^*\ell\nu_\ell$ in the official Belle

decay	CLN parameter
$B \to D\ell\nu_\ell$	$\rho^2 = 1.16$
$B \to D^*\ell\nu_\ell$	$\rho^2 = 1.3$ $R_1(1) = 1.18$ $R_2(1) = 0.71$

Table 4.4: Parameters of outdated CLN form factor parametrization as used in generation of the official Belle MC data. A full explanation of the parameter is given in [74].

MC samples. Apart from outdated parameters, listed in Table 4.4 employed in this model, recent analyses favor a parametrization based on a model-independent approach by Boyd, Grinstein and Lebed (BGL) [75]. The differential decay rates of both of these parametrizations are implemented in the `eFFORT` package [76].

It provides the ability to calculate weights of the form

$$w^{D}_{\mathrm{CLN}\to\mathrm{BGL}}(w) = \frac{\dfrac{\mathrm{d}\Gamma_{\mathrm{BGL}}(w)}{\mathrm{d}w}}{\dfrac{\mathrm{d}\Gamma_{\mathrm{CLN}}(w)}{\mathrm{d}w}} \tag{4.30}$$

and

$$w^{D^*}_{\mathrm{CLN}\to\mathrm{BGL}}(w, \cos\theta_\ell, \cos\theta_V, \chi) = \frac{\dfrac{\mathrm{d}\Gamma_{\mathrm{BGL}}(w, \cos\theta_\ell, \cos\theta_V, \chi)}{\mathrm{d}w\mathrm{d}\cos\theta_\ell\mathrm{d}\cos\theta_V\mathrm{d}\chi}}{\dfrac{\mathrm{d}\Gamma_{\mathrm{CLN}}(w, \cos\theta_\ell, \cos\theta_V, \chi)}{\mathrm{d}w\mathrm{d}\cos\theta_\ell\mathrm{d}\cos\theta_V\mathrm{d}\chi}} \tag{4.31}$$

for $B \to D\ell\nu_\ell$ and $B \to D^*\ell\nu_\ell$ decays respectively. $\mathrm{d}\Gamma_{\mathrm{model}}(\boldsymbol{\theta})/\mathrm{d}\boldsymbol{\theta}$ is the differential decay rate for the given model parametrization with respect to the set of kinematic decay variables $\boldsymbol{\theta}$, defined in Equation 4.28 and Equation 4.29.

Each MC event including one or two decays of the type $B \to D^{(*)}\ell\nu_\ell$ on generator level is corrected with one individually calculated weight for each B meson. The calculation of the weights are based the corresponding kinematic variables of the generator level decay.

The values that parametrize the BGL form factors for the decays of $B \to D\ \ell\ \nu_\ell$ are given by a private fit to the data points provided by Glattauer et al. in [77]. The values are listed in table Table 4.5.

The values that parametrize the BGL form factors for the decay $B \to D^*\ \ell\ \nu_\ell$ are given by Ferlewicz et al. [78]. The configuration that is used in this analysis is BGL(1,1,2), refer to [78] for detailed information. The values for the latter are listed in table Table 4.6.

The distribution of weights and the kinematic variables that are used to calculate the weights are shown in Figure 4.3 and Figure 4.5 for $B \to D\ell\nu_\ell$ and $B \to D^*\ell\nu_\ell$ decays respectively. Shown in these figures are the results for generator level

	(Nom. $\pm$ stat) $\times 10^3$	
V_{cb}	41.184	1.152
$f_+(0)$	12.615	0.098
$f_+(1)$	-96.208	3.341
$f_+(3)$	413.884	94.447
$f_+(3)$	-173.699	891.809

Table 4.5: The parameters used in the BGL parametrization for the decay $B \to D\ell\nu_\ell$, taken from a private fit to the data provided in [77].

	(Nom. $\pm$ stat $\pm$ sys) $\times 10^3$		
a_0^g	1.000	0.020	0.020
a_1^g	-2.350	0.610	0.660
a_0^f	0.511	0.004	0.013
a_1^f	0.670	0.170	0.300
$a_0^{F_1}$	0.300	0.060	0.080
$a_1^{F_1}$	-3.680	1.120	1.200

Table 4.6: The parameters that are used in the BGL(1,1,2) parametrization for the decay $B \to D^*\ell\nu_\ell$, taken from [78]. Listed are the nominal values and their statistical and systematic uncertainties. More explanations can be found in [78].

decays (upper) and true variables of reconstructed candidates (lower). The mean of the weights determined for uncut generator level decays is equal to 1, hence the normalization is conserved. This is different for the selected candidates with kinematic cuts to extract signal.

Model update 2 : $B \to D^{**}\ell\nu$

The other type of decays that undergo form factor corrections are $B \to D^{**}\ell\nu$, where D^{**} is either D_1, D_1' D_2^* or D_0^*.

For these decays, we update the form factor models from the ISGW2 parametrization [79] that was used in the official Belle MC, to the parametrization of Leibovich, Ligeti, Stewart and Wise (LLSW, [80]).

Other than for $B \to D\ell\nu$ and $B \to D^*\ell\nu$, the decay rates of these are not analytically implemented in eFFORT. In the course of the analysis of $\mathcal{R}(D^{(*)})$ [81], [82], another method was developed that realizes the reweighting and was later implemented into eFFORT as well. The principle of the method is the comparison of histograms of suitable kinematic variables that describe the decay on generator-level for both parametrization. For this, the same MC samples are produced once with the ISGW2 model and once with the LLSW model. With the existing setup of the Belle Analysis Software Framework, it is not possible to generate Belle MC with the LLSW parametrization for the form factor model. As this method anyway only depends on generator level information and also not on the reference frame (Belle and Belle II have different boosts), the MC samples can be produced with

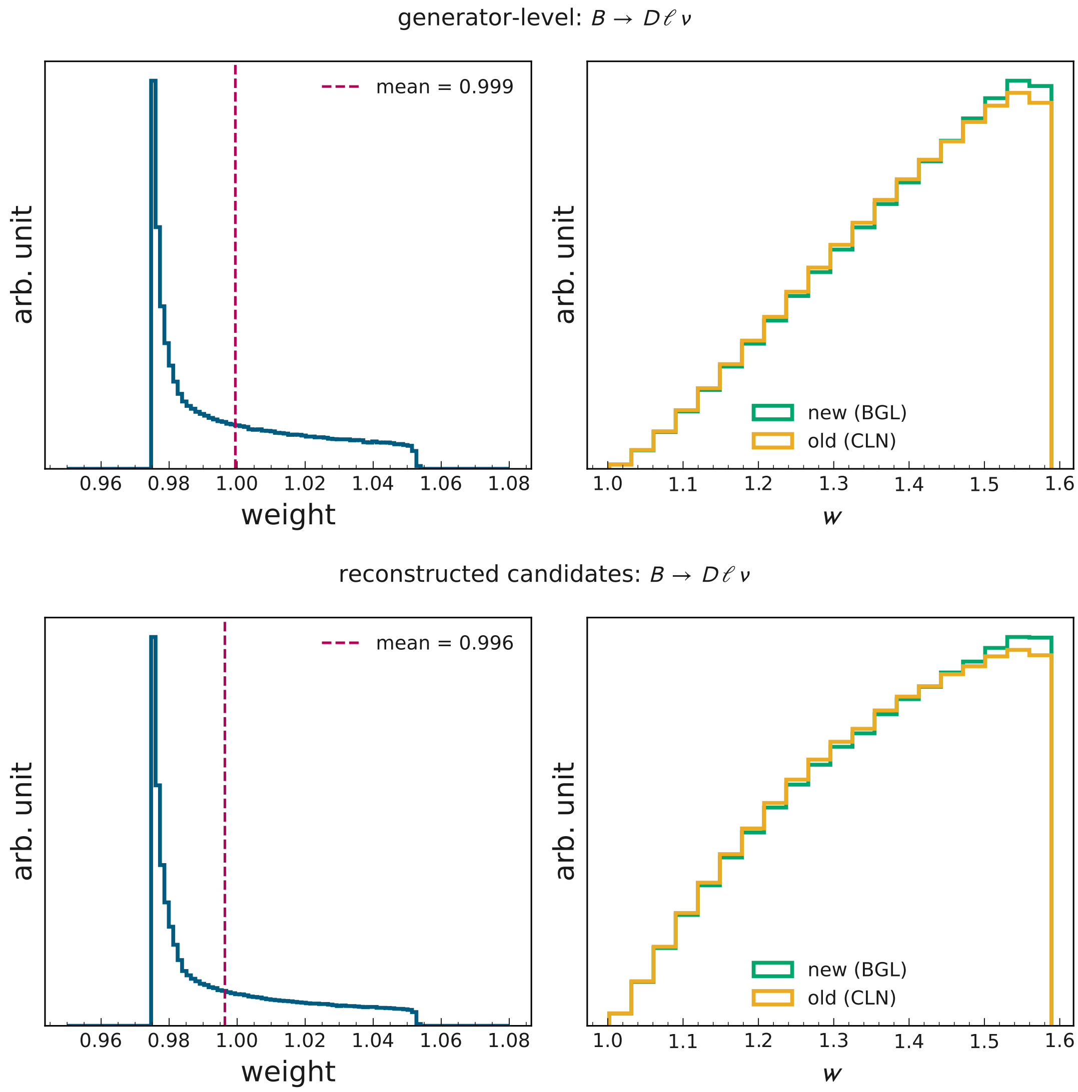

Figure 4.3: Weight distribution and true kinematic variable used to determine form factor model corrections for $B \to D\ell\nu_\ell$ decays. Upper: Generator level particles. Lower: Reconstructed candidates .

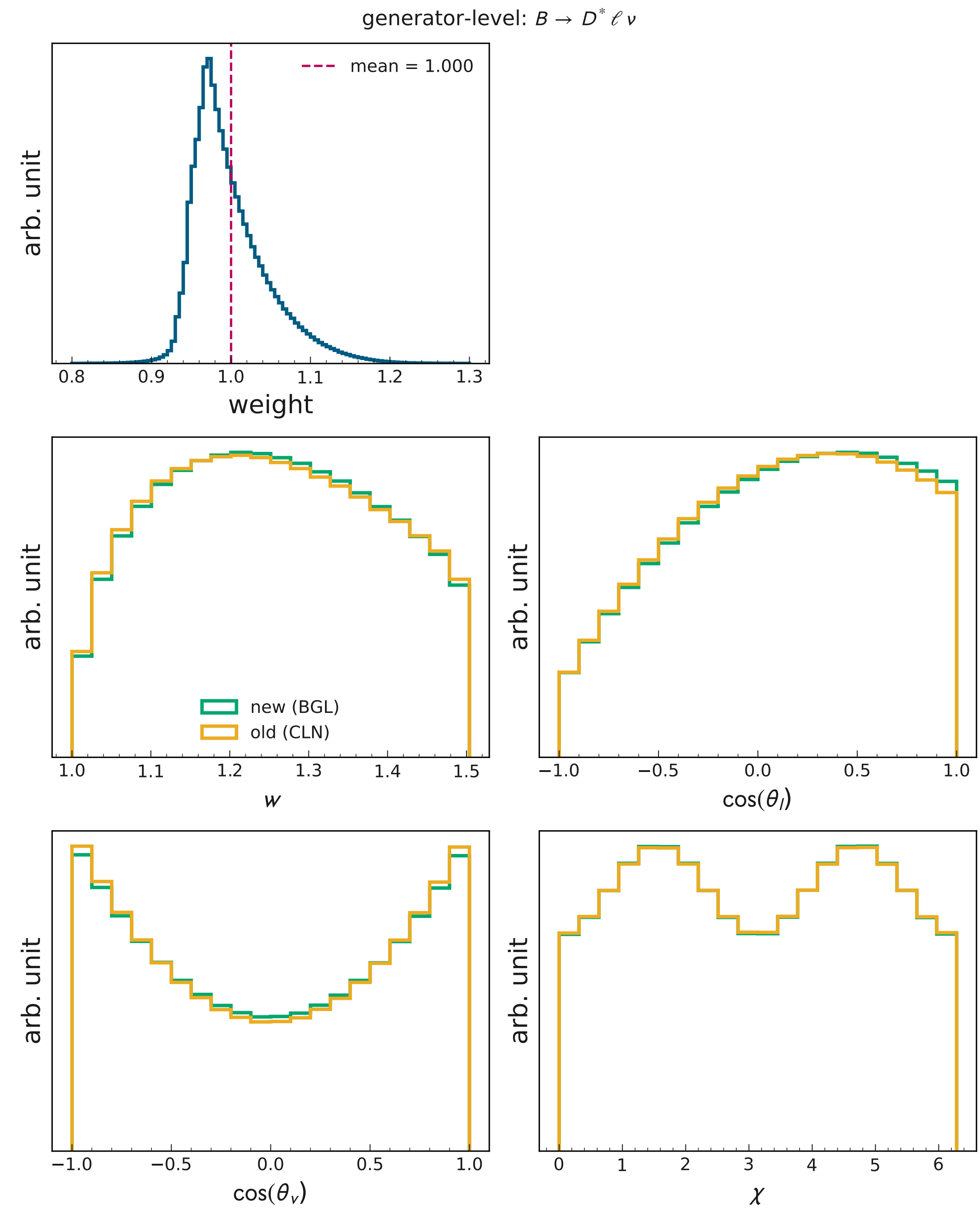

Figure 4.4: Weight distribution and kinematic variables used to determine form factor model corrections for generator-level $B \to D^* \ell \nu_\ell$ decays.

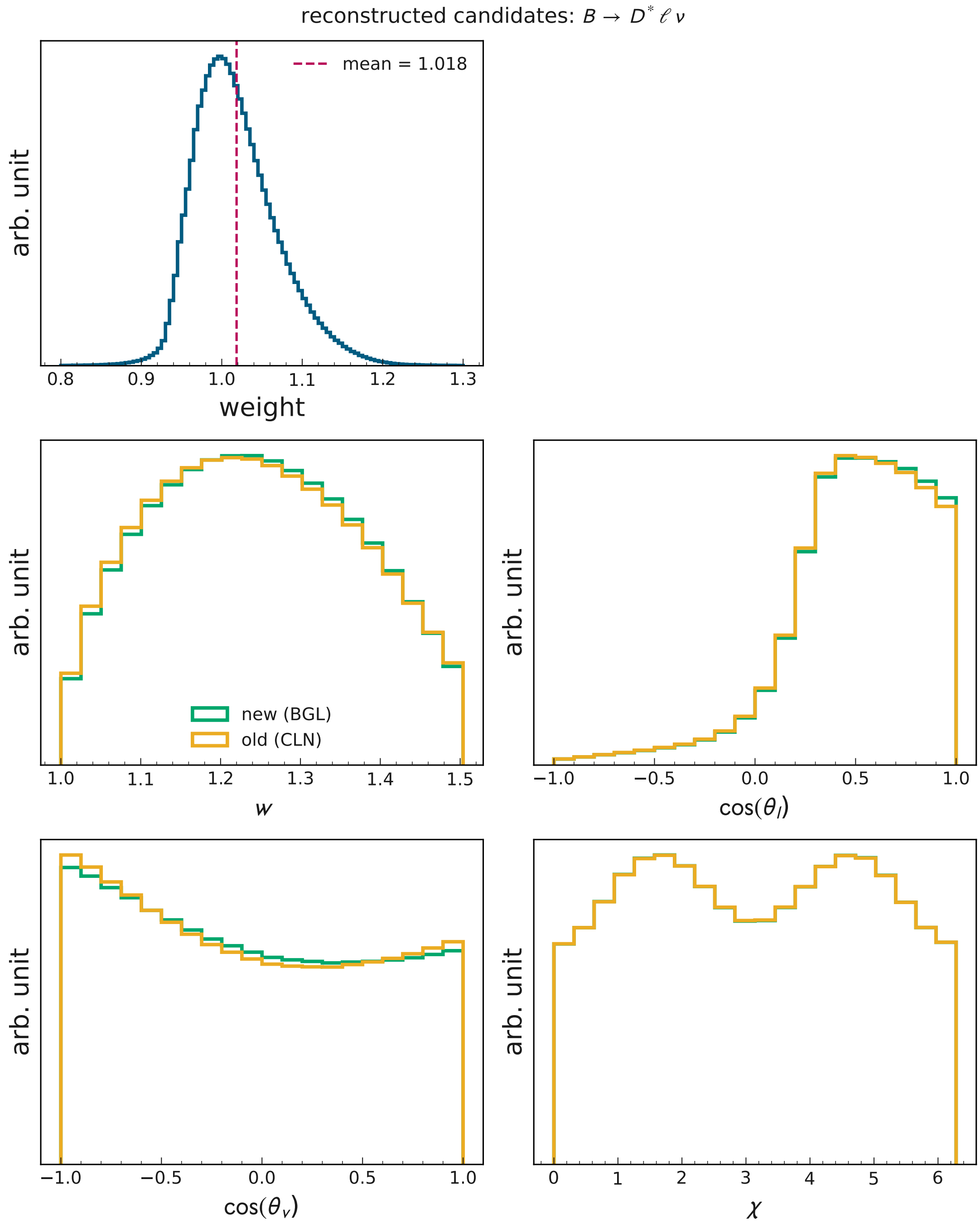

Figure 4.5: Weight distribution and kinematic variables used to determine form factor model corrections for true reconstructed $B \to D^* \ell \nu_\ell$ decays.

`basf2`, the Belle II Analysis Software Framework.

For $B \to D_1 \ell \nu$ decays, calculation of weights in based on the approximation of the analytical equations Equation 4.30 or Equation 4.31 with the histograms of the MC samples:

$$\hat{w}^{D_1}_{\text{ISGW2}\to\text{LLSW}}(i_w, i_{\cos\theta_l}, i_{\cos\theta_V}) = \frac{N^{\text{LLSW}}_{i_w, i_{\cos\theta_l}, i_{\cos\theta_V}}}{N^{\text{ISWG2}}_{i_w, i_{\cos\theta_l}, i_{\cos\theta_V}}}, \tag{4.32}$$

where N denotes the histogram bin content for the given model and i_x the bin in the variable x, evaluated on generator level. For $B \to D_1' \ell \nu$ and $B \to D_2^* \ell \nu$, the formula reads

$$\hat{w}^{D_1'/D_2^*}_{\text{ISGW2}\to\text{LLSW}}(i_w, i_{\cos\theta_l}) = \frac{N^{\text{LLSW}}_{i_w, i_{\cos\theta_l}}}{N^{\text{ISWG2}}_{i_w, i_{\cos\theta_l}}}, \tag{4.33}$$

and for $B \to D_0^* \ell \nu$, it only depends on w:

$$\hat{w}^{D_0^*}_{\text{ISGW2}\to\text{LLSW}}(i_w) = \frac{N^{\text{LLSW}}_{i_w}}{N^{\text{ISWG2}}_{i_w}}, \tag{4.34}$$

The choice of kinematic variables that are used for the reweighting is following the studies made by M. Welsch in [82]:

- $B \to D_1 \ell \nu$: w, $\cos\theta_l$, $\cos\theta_V$
- $B \to D_1' \ell \nu$: w, $\cos\theta_l$
- $B \to D_2^* \ell \nu$: w, $\cos\theta_l$
- $B \to D_0^* \ell \nu$: w

An interpolation with radial basis functions is eventually carried out to convert the weights $\hat{w}$ into a continuous analytical expression w, applicable to correct the form factor models of $B \to D^{**} \ell \nu$ decays. The normalization is determined by applying the interpolated ratio to the ISGW2 sample, subsequently the number of ISGW2 events is divided by the sum of the weights.

The outcome of this reweighting method is shown exemplarily for the decay $B \to D_1 \ell \nu$ in Figure 4.6 and Figure 4.7. Again, the upper plots show the result for generator level decays, whereas the lower plots show the impact on reconstructed candidates. The dependencies of the form factor models to the kinematic variables is noticeable: While the distributions for ISGW2 and LLSW are distinctly different for w, $\cos\theta_l$, $\cos\theta_V$, while they overlap for χ. Similar observations are made for the other D^{**} decays.

The remaining plots For D_1', D_2^* and D_0^* are found in section A.2 in Figure A.1, Figure A.3 and Figure A.5 respectively.

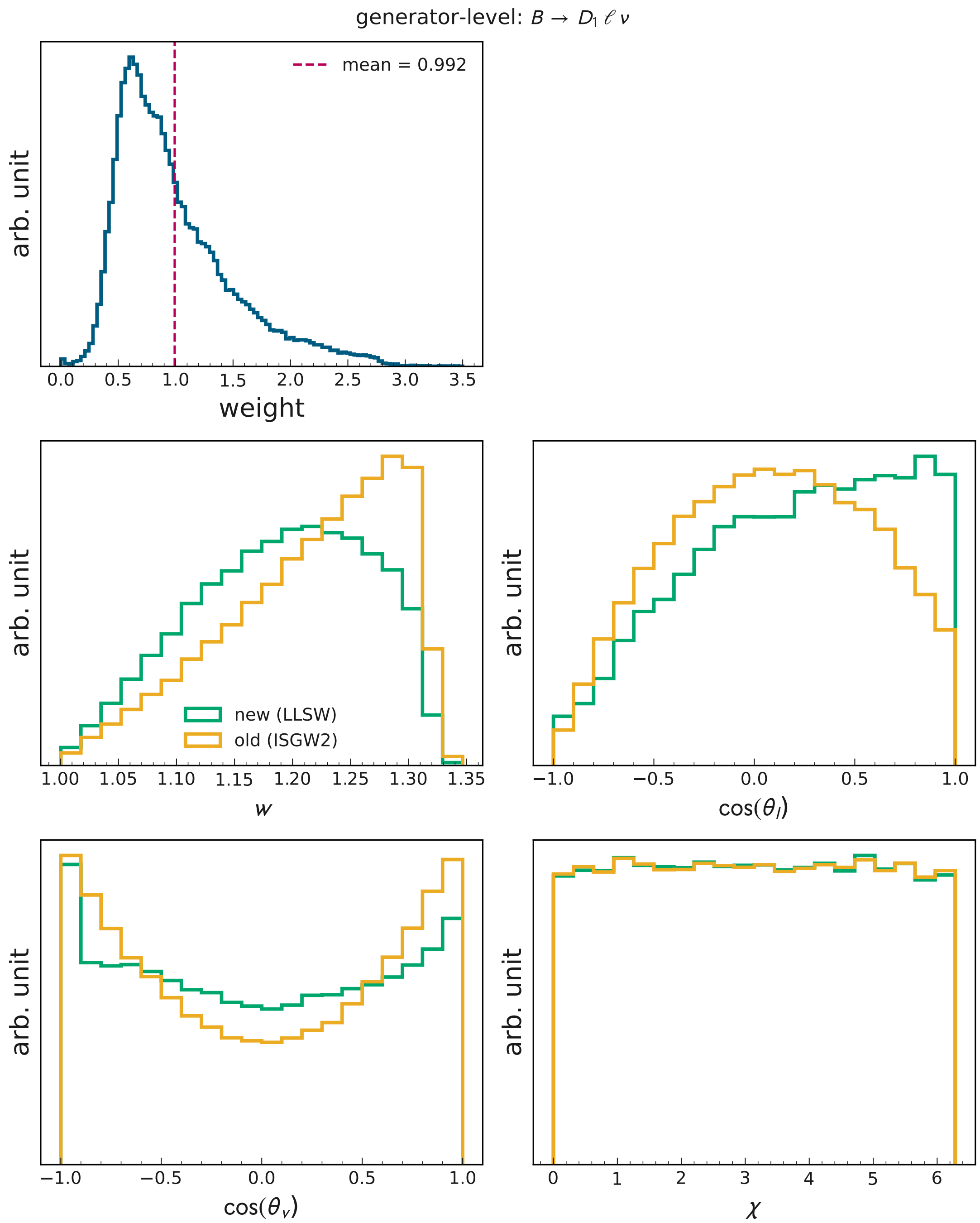

Figure 4.6: Weight distribution and kinematic variable used to determine form factor model corrections for generator-level $B \to D_1\ell\nu$ decays. The plots for the remaining D^{**} decay channels are found in section A.2.

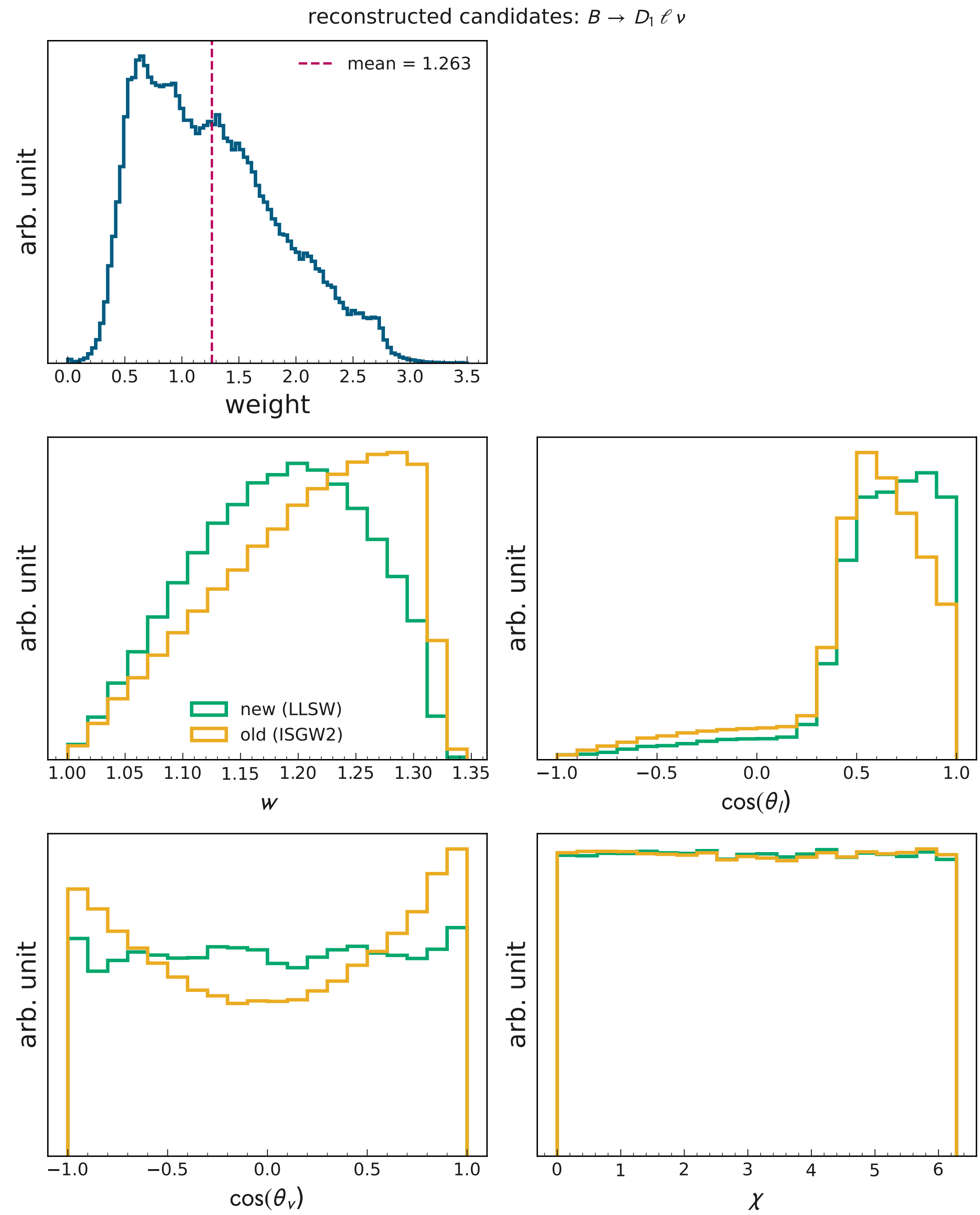

Figure 4.7: Weight distribution and kinematic variable used to determine form factor model corrections for true generated $B \to D_1 \ell \nu$ decays. The plots for the remaining D^{**} decay channels are found in section A.2.

Chapter 5

Analysis Method

5.1 Single and double tag method

The objective of this analysis is to quantify $f_{00} = \mathcal{B}\big(\Upsilon(4S) \to B^0\overline{B}^0\big)$ and is based on a method employed in a similar analysis by *BaBar* [2].

In particular, this analysis adopts a model-independent approach for extracting the branching fraction, ensuring a direct measurement without relying on explicit or implicit assumptions of isospin symmetry. Consequently, no quantities measured under the assumption of conserved isospin, especially regarding the decay rates and branching fractions of B decays, are used in determining f_{00}. The method explained below, based on single and double tags, enables this to be achieved.

The branching fraction f_{00} to determine is found in the equation that counts the number of candidates N with at least one B^0 decaying into a defined signal mode, referred to as *single-tag*:

$$N_{\text{single}} = 2 \cdot N_{B\overline{B}} \cdot f_{00} \cdot \mathcal{B}\big(\, B^0 \to \text{signal}\,\big) \cdot \epsilon_{\text{single}}, \tag{5.1}$$

where $N_{B\overline{B}}$ is the number of produced $B\overline{B}$ pairs, $\mathcal{B}\big(\, B^0 \to \text{signal}\,\big)$ denotes the branching fraction of the B^0 decaying into a dedicated signal mode (defined in section 5.2) and ϵ_{single} the signal reconstruction efficiency. The factor of 2 accounts for the fact that both B meson can decay into signal. A detailed deduction of this formula is given in the appendix section A.1. Note that cases where both B^0 mesons decay into the signal are regarded as comprising two single-tag candidates.

The branching fraction of the signal decay $\mathcal{B}\big(\, B^0 \to \text{signal}\,\big)$ has to be omitted, for itself was measured with assumed isospin. To achieve this, and thus a model independent extraction of f_{00}, we consider events where not only one, but both B^0 decay into signal, as well. Hence, the label *single* in Equation 5.1 to reference that for each event both B candidates are tagged individually. Following, the equation for counting these double-tagged events reads

$$N_{\text{double}} = N_{B\overline{B}} \cdot f_{00} \cdot \Big[\mathcal{B}\big(\, B^0 \to \text{signal}\,\big)\Big]^2 \cdot \epsilon_{\text{double}}, \tag{5.2}$$

where the signal branching fraction occurs in square and ϵ_{double} denotes the efficiency to reconstruct both B via the same channel. It should be explicitly noted here that one double-tag candidate is considered simultaneously as two single-tag candidates.

Taking the square of Equation 5.1 and dividing by Equation 5.2, and solving it for f_{00} yields

$$f_{00} = \frac{1}{4N_{B\bar{B}}} \cdot \frac{N^2_{\text{single}}}{N_{\text{double}}} \cdot \frac{\epsilon_{\text{double}}}{\epsilon^2_{\text{single}}}, \tag{5.3}$$

where the branching fraction is cancelled out naturally. This allows for a model independent extraction of the branching fraction f_{00} by only counting the number of single and double tag candidates and determining their reconstruction efficiencies based on simulation.

5.2 Signal channel and partial reconstruction

In principle, any decay mode can be selected as signal in this analysis. In practice, however, the main criterion is to achieve the highest possible reconstruction efficiency, given the limited size of the data set. Therefore, the decay of $B^0 \to D^{*-}\ \ell^+\ \nu_\ell$ followed by $D^{*-} \to \overline{D}^0\ \pi^-$ is chosen as signal channel. The subsequent decay of the $\overline{D}^0$ meson is not reconstructed; instead, all possible decays of the $\overline{D}^0$ meson are considered, see Figure 5.1. This approach is commonly termed *partial reconstruction*, although *BaBar* coined the term *inclusive reconstruction* which was considered misleading in the context of a *Belle* analysis.

The method mentioned in section 5.1 utilizes events in which both B mesons are reconstructed via the same decay mode. The rate of such a double tag event is naturally quite low as the probability for it to occur is proportional with the square of the branching fraction.

This is considered by choosing a signal decay channel that has a comparatively high branching fraction of approximately [1]

$$\mathcal{B}\big(\, B^0 \to \text{signal}\,\big) = 0.05 \times 0.68 = 3.4\% \tag{5.4}$$

and at the same time allowing a reconstruction technique that provides a high reconstruction efficiency: a semileptonic charmed decay, where the B^0 is partially reconstructed. This means that the B^0 candidate is merely formed by combining a lepton and a charged pion. The resulting loss of purity by not reconstructing the $\overline{D}^0$ is accepted in favor of the statistics gained.

As later elaborated in section 5.5, the maximum possible momentum of the pion in the center-of-mass frame is only slightly more than 1 MeV. Therefore, it is referred to as a *slow pion*.

The measurement itself comprises only counting of single and double tag candidates, so the precise position and shape of the fit variable distribution is particularly not important, as long as it is sufficiently distinguishable from background events.

$$
\begin{array}{lll}
B^0 \to D^{*-}\,\ell^+\,\nu_\ell & & \mathcal{B}\big(B^0 \to D^{*-}\ell^+\nu\big) \sim 5\% \\
\quad \hookrightarrow \overline{D}^0\,\pi^- & & \mathcal{B}\big(D^{*-} \to \overline{D}^0\pi^-\big) \sim 68\% \\
\qquad \to \cdots,\ \cdots,\ \cdots & & \text{not reconstructed}
\end{array}
$$

Figure 5.1: Signal channel and the corresponding branching ratios. Partially reconstructed means the particular decay of the $\overline{D}^0$ is not reconstructed, but all possible modes are taken into account. This increases the efficiency but decreases the purity.

5.3 Event selection

Before the reconstruction is carried out with `basf2`, the Belle `mDST` data is converted to the Belle II `mDST` data format via with a `basf2` module called `b2biiConversion.convertBelleMdstToBelleIIMdst`. As recommended by the documentation of the software, the default settings of the conversion module are applied:

- `hadronB = True`: A collection of cuts, the aim of which is to filter for $B\overline{B}$ events. According to the report, an efficiency of 99.1% is achieved [83].
- `smearTrack = 2`: Apply small variations to parameters of track helix to achieve better match between data and MC, more information is found in [84].

The following list gives a detailed description of the reconstruction part of the analysis. A schematic overview can be found in Figure 5.2.

- All tracks must be of the same track quality: The transverse distance to the interaction point for a vertex (dr) must be less than 2 cm and the distance of the $z-$ component of the point-of-closest-approach to the interaction point (dz) must be less than 4 cm.
- Electrons and muons are selected with momenta between 1.5 GeV and 2.5 GeV in the $\Upsilon(4S)$ center-of-mass frame and a particle identification probability (PID) of 0.90. The momentum requirement is to prevent leptons from $e^+e^- \to c(\to X\ell\nu)\bar{c}$ decays.
- Candidates for the pion are selected based on a center-of-mass momentum of less than 200 MeV. The selection of slow pion is justified given the available phase space in the D^* decay, further details are provided in section 5.5. Since slow pions do not reach particle identification detectors such as TOP, it is not advisable for *Belle* analyses to cut on PID. This would result in more true pion candidates being lost than fakes being rejected.
- The B^0 candidate is reconstructed by the opposite-sign combination of a lepton and a slow pion candidate. In this partial reconstruction the D^0 meson produced in the decay of the D^* is not reconstructed. Consequently, the full

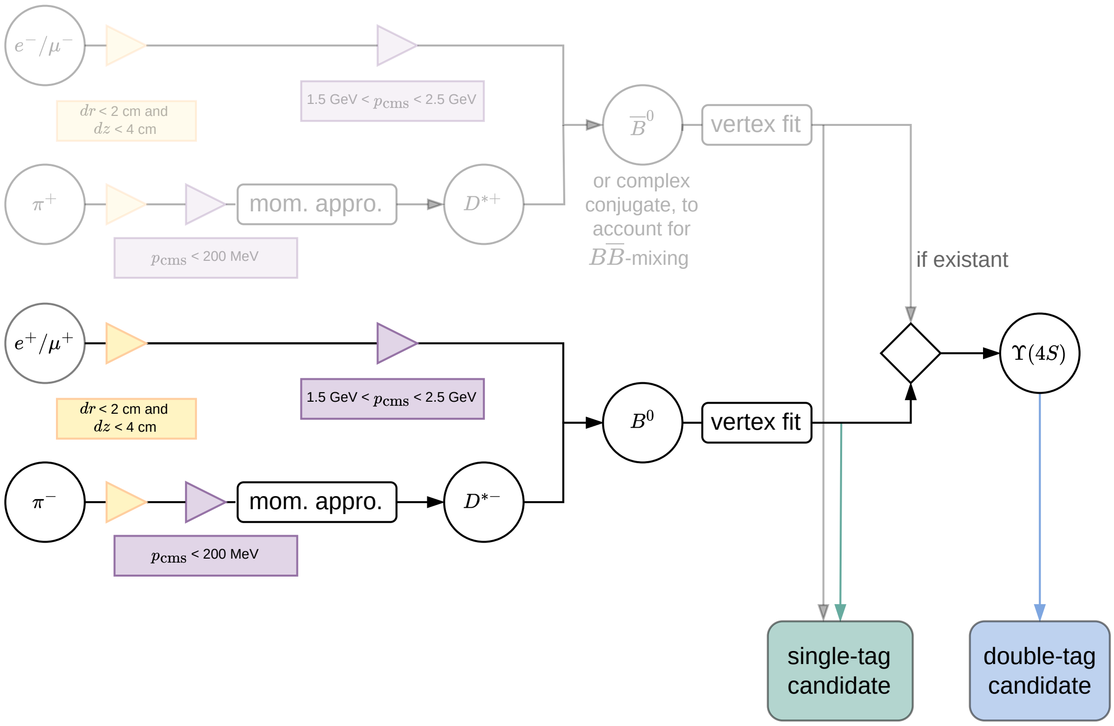

Figure 5.2: The scheme of the reconstruction. Lepton and pion candidates fulfilling certain track and momentum requirements are selected. The momentum of the pion is used to approximate a D^* meson. A B^0 candidate is formed by combining the pion and D^* candidate. A fit eliminates B^0 candidates for which no vertex can be found for the trajectories of their daughter particles. The relevant variables for further analysis of the resulting single-tag candidates are stored in a ROOT file. If at least one additional B^0 candidate can be identified within the event, an $\Upsilon(4S)$ candidate (double-tag) is formed, and its variables are also stored accordingly.

detector information on the kinematics of the D^* is not available. To address this limitation, the 4-momentum is approximated only by the kinematics of the π and by exploiting the unique phase space configuration of the D^* decay, as further discussed in section 5.5.

- Upon obtaining the B^0 candidate, a vertex fit is performed, and candidates that fail the fit are discarded. For the remaining candidates, their variables are stored in a ntuple and labelled *single-tag*.

- If there are at least two B^0 candidates in the event, an attempt is made to combine them into one or more $\Upsilon(4S)$ candidates. To account for $B^0\overline{B}^0$ mixing, both combinations of $\Upsilon(4S) \to B^0\overline{B}^0$ and $\Upsilon(4S) \to B^0\ B^0$ are considered. No selection criteria are applied to the $\Upsilon(4S)$. Finally, the variables of these candidates are also stored in a ntuple and labelled as *double-tag*.

5.4 Bremsstrahlung correction

A decelerating charged particle looses energy by radiation. To obtain the four momentum of the electron when it was created in the decay, the four momentum of the photons emitted from the electron have to be taken into account. The `basf2` module `modularAnalysis.correctBremsBelle` is employed for this purpose.

In this process, the 4-momentum of the photon closest to the electron's track, within a cone with an opening angle of $5°$, is added to the momentum of the electron. In addition, the photons must meet a criterion based on energy deposition within a specified region of the ECL. These regions are segmented into the forward direction (cluster region 1, opening angle between $19° - 31°$), the barrel (cluster region 2, $31° - 129°$) and the backwards direction (cluster region 3, $131° - 154°$). The conditions are:

- `clusterReg == 1 and clusterE > 0.075 and E < 0.5`,
- `clusterReg == 2 and clusterE > 0.05 and E < 0.5`,
- `clusterReg == 3 and clusterE > 0.1 and E < 0.5`.

Here, the `clusterReg` specifies the cluster region, `clusterE` represents the sum of the ECL cluster's energy and E is the photon's energy.

5.5 D^*-momentum approximation

As described in section 5.2, the decay tree is only reconstructed until $D^{*-} \to \overline{D}^0\pi^-$. Due to this partial reconstruction, the 4-momentum of the D^* cannot be measured since the kinematic information of the $\overline{D}^0$ is missing. In order to still calculate the fit variable missing mass squared (more information in section 6.1)

$$M^2_{\text{miss}} = \left(p_{B^0} - p_{D^*} - p_\ell\right)^2 \tag{5.5}$$

it becomes necessary to estimate the D^* 4-momentum using available kinematic variables, specifically those of the charged pion.

The possibility of estimating the 4-momentum of the D^* solely based on the measured 4-momentum of the π arises from the following conditions:

1. the charge of the D^{*-} is uniquely defined by the charge of the π^- and $D^{*0} \to D^+\pi^-$ is forbidden by energy conservation, and
2. the mass of the D^{*-} is only slightly larger than the sum of the masses of the daughter particles π^- and $\overline{D}^0$ [1]:

$$M_{D^*} = (2010.26 \pm 0.05)\,\text{MeV} \tag{5.6}$$
$$M_D + M_\pi = (2004.41 \pm 0.05)\,\text{MeV} \tag{5.7}$$

The first condition enables the clear assignment that if a D^* decays to a charged pion, the only possible mode is $D^{*-} \to \pi^-\overline{D}^0$. The second condition allows a good approximation of the 4-momentum D^{*-} by using only the 4-momentum of the slow

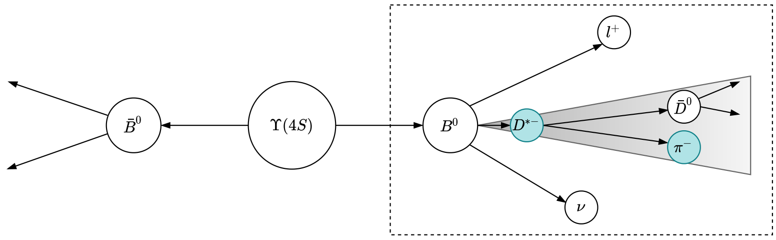

Figure 5.3: In the center-of-mass frame, the flight direction of the pion is similar to the direction of the D^*. This is a consequence of the limited phase space of the D^* decay ($m(D^*) \approx m(\pi) + m(D^0)$)

pion. The small difference in mass between the mother and its daughter particles implies a small kinematic phase space. As a consequence, in the D^* rest frame, the pion is nearly at rest. Hence, in the $\Upsilon(4S)$ center-of-mass frame, the slow pion is emitted within a 1 radian wide cone centered around the D^* direction[36], which is depicted in Figure 5.3.

To estimate the D^* 4-momentum, the correlation of the reconstructed pion 4-momentum and the true D^* 4-momentum is examined. Due to the radial symmetry, there is no difference between the $x-$ and $y-$components, for which they are treated equally. The $z-$component and the energy are plotted separately. The resulting three correlation plots are found in Figure 5.4.

All correlations were fitted with third-degree polynomials. To facilitate this, the pion momentum components are divided into 50 bins between $-0.18\,\text{GeV}$ and $0.18\,\text{GeV}$. For each of these bins, the mean of the true D^* momentum distribution is calculated to create a profile plot. The fit is performed on the profile distribution. The fit parameters a_i, b_i and c_i for $x-$ and $y-$components, $z-$component and energy respectively, are finally used to approximate the D^* 4-momentum:

$$p_x(D^*) = \sum_{i=0}^{3} a_i \cdot p_x^i(\pi) \tag{5.8}$$

$$p_y(D^*) = \sum_{i=0}^{3} a_i \cdot p_y^i(\pi) \tag{5.9}$$

$$p_z(D^*) = \sum_{i=0}^{3} b_i \cdot p_z^i(\pi) \tag{5.10}$$

$$E(D^*) = \sum_{i=0}^{3} c_i \cdot E^i(\pi) \tag{5.11}$$

The result of the 4-momentum estimation can be seen in the third row in Figure 5.4, together with the true distribution it tries to approximate. The last row plots show the differences between the true and approximated distributions.

The width of the distribution representing the difference between the initially generated and the calculated estimation suggests that the approximated momentum components describes the actual momentum with an accuracy of roughly $0.5\,\text{GeV}$.

The agreement for the 3-space momentum components is generally considered adequate, reflecting the high degree of correlation of the pion and D^* in these components. Estimation of the energy component, however, is not as reliable. This is most likely due to the fact that the pion is emitted either in the same or in the opposite direction of the D^*, when observed in the center-of-mass system.

Hence, the energy correlation differs for forward and backward pions, which is depicted in the upper right plot in Figure 5.4 by the red band (forward emitted pions) and the off-diagonal contribution in white (backward emitted pions). In addition, the reconstruction performance of the backward emitted pions is lower.

Since the approach to approximating the D^* energy does not differ between the two cases, the estimate does not agree as well with the expectation. This inaccuracy will be reflected in the shape of the distribution of the M^2_{miss}, as described in section 6.1. In particular, the inaccuracy due to the approximation reduces the sharpness of the signal peak. This is acceptable insofar as an exact description of the shape of the distribution is not the primary concern, but the distinctness of the signal from the background.

5.6 Truth matching

In the jargon of particle physics experiments, *truth-matching* in an MC study refers to the identification of the originally generated counterpart of a reconstructed particle candidate. This involves not only comparing the particle identity, but also checking the decay topology, i.e. the correct relationship to ancestors and descendants for all particles involved in the decay.

For this analysis, the standard approach of truth-matching is not applicable, so that an indicator for the quality of the MC match is not readily available. In the case of partial reconstruction of the D^*, the `MCMatcherParticles` module does not provide the `basf2` variable `isSignal`.

Such a variable, which classifies signal candidates as correctly or incorrectly reconstructed, is required both for determining reconstruction efficiencies and for fitting templates. The following describes the implementation of the truth-matching algorithm that is applied in this analysis.

`isSignalInclusive`

As described in section 5.2, a pair of π and ℓ is selected. Subsequently, the π candidate is used to create a D^* particle, according to the explanation in section 5.5. Finally, the B^0 candidate is a combination of the D^* and the lepton.

In order to validate the reconstruction of a signal candidate, it is necessary to establish the correspondence between all relationships of the reconstructed candidate and the generated particle. This is accomplished by invoking the `matchMCTruth` method on the `ParticleList`. Subsequently, generator-level information becomes available regarding the particle's identity and, for each particle, its specific decay topology.

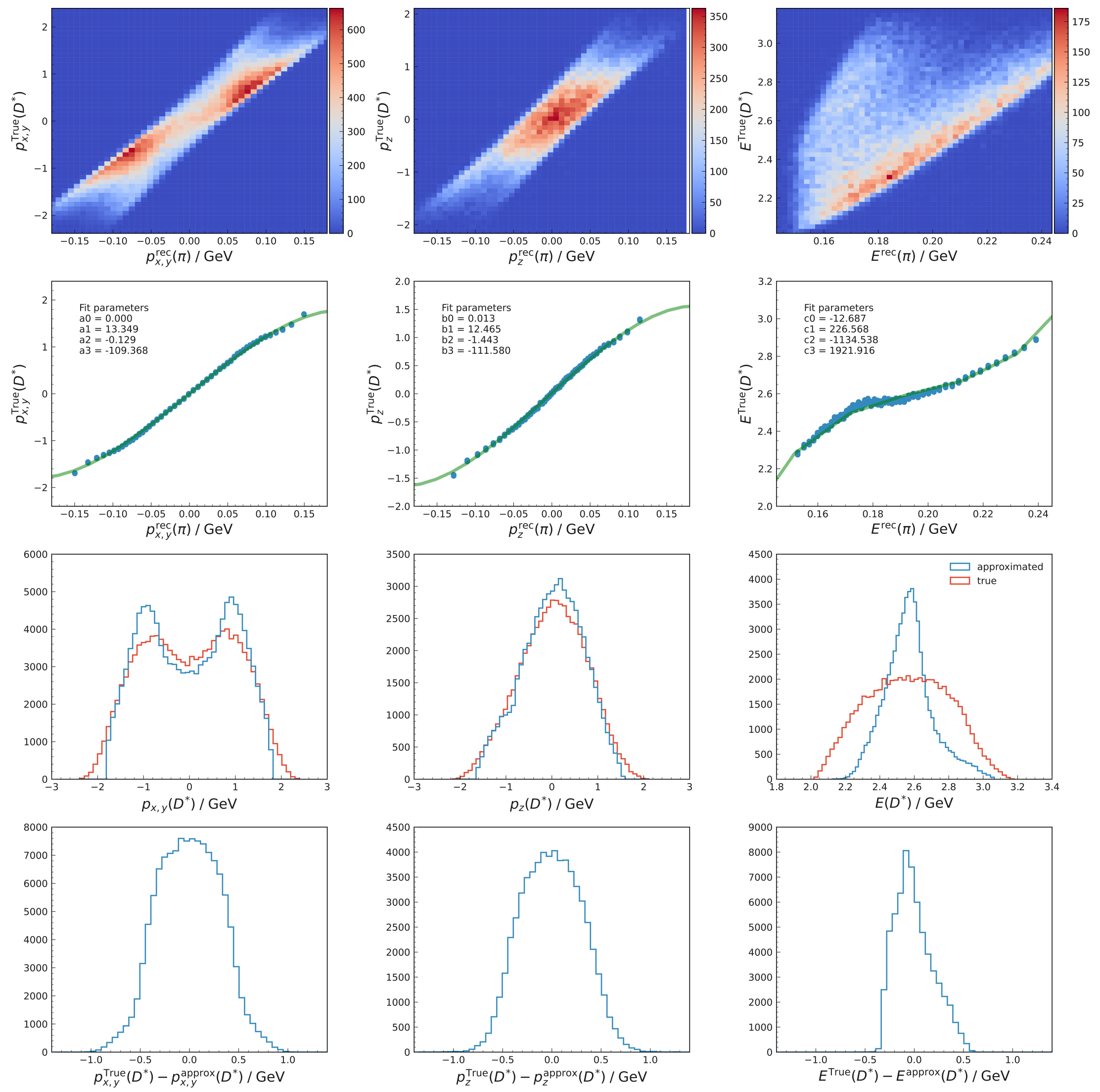

Figure 5.4: The correlation of the reconstructed pion and the true D^* 4-momenta in the center-of-mass frame is used to approximate the D^* momentum. The top row shows the 2-dimensional correlation, the second row the profile plot of the above ones. The profile plot distributions are fitted with third-degree polynomials. To approximate the D^* 4-momentum components, the fit parameters are used to scale the reconstructed pion momentum, seen in the third row. The last row depicts the difference between the true and the approximated D^* 4-momentum components.

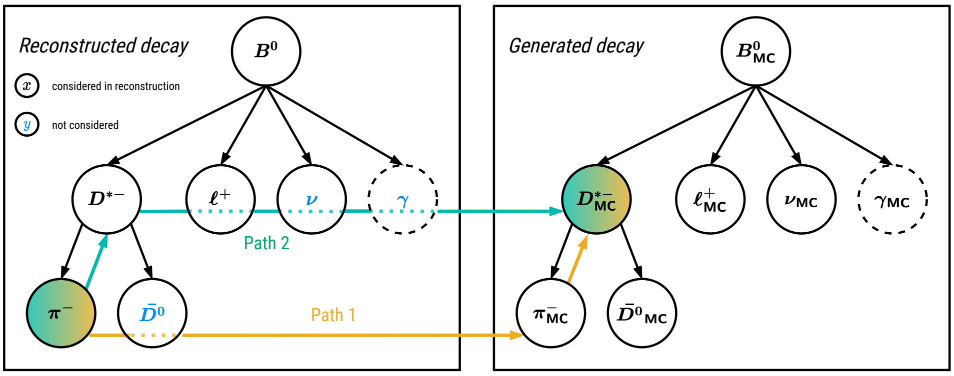

Figure 5.5: Truth-matching algorithm that provides the variable to identify correctly reconstructed candidates, denoted as `isSignalInclusive`:

1. Initiate at reconstructed π^- candidate
2. follow **Path 1**
   - link candidate to MC-related particle $\rightarrow \pi^-_{\text{MC}}$
   - obtain mother of MC-related particle $\rightarrow D^{*-}_{\text{MC}}$(Path 1)
3. follow **Path 2**
   - obtain mother of reconstructed particle $\rightarrow D^{*-}$
   - link reconstructed mother to MC-related particle $\rightarrow D^{*-}_{\text{MC}}$(Path 2)
4. confirm that particles at endpoints of both paths are identical $\rightarrow D^{*-}_{\text{MC}}(\text{Path 1}) = D^{*-}_{\text{MC}}(\text{Path 2})$
5. iterate steps 1. – 5. for each reconstructed particle (π^-, D^{*-}, ℓ^+, B^0)

For the actual truth-matching of the reconstructed B^0 candidate, one has to verify the correct particle identity and the correct origin of the particle, i.e. does the particle come from the correct mother particle. This is done iteratively for each reconstructed particle. The algorithm is illustrated and explained in Figure 5.5.

This algorithm ensures the accurate lineage for each of the reconstructed particles. To reject other decay modes, the daughter particles of the B^0 should exclusively consist of D^*, ℓ, ν, or γ. No specific considerations need to be made regarding the neutrino or any possible number of photons.

If all of the checks are positive, the newly created variable `isSignalInclusive` is set to 1, otherwise it is set to 0 and to `NaN` if no MC particles were found.

`isSignalInclusiveDouble`

For double-tag candidates, an additional variable is required to validate the reconstruction of the $\Upsilon(4S)$. This variable results from combining the previous one, where the algorithm is applied to both daughter particles. The variable `isSignalInclusiveDouble` is set to 1 only if both B^0 candidates are correctly reconstructed; otherwise, it is set to 0.

5.7 Reconstruction efficiencies

The formula for f_{00} in Equation 5.3 calculates the branching fraction by counting single and double-tagged signal candidates. The ratio of the efficiencies involved will be denoted as C_{eff}, adopted from the *BaBar* analysis:

$$C_{\text{eff}} = \frac{\epsilon_{\text{double}}}{\epsilon^2_{\text{single}}}. \tag{5.12}$$

The efficiency ϵ is defined as the ratio of the number of correctly reconstructed candidates and the number of true signal decays in the sample. Two distinct efficiencies are distinguished: the single-tag efficiency ϵ_{single} and the double-tag efficiency ϵ_{double}. The efficiencies are crucial for scaling the number of reconstructed candidates to obtain the actual number of signal B^0 in the data. To determine the efficiencies, the simulation is employed. The calculation of the single-tag efficiency is carried out as follows:

$$\begin{aligned}
\epsilon_{\text{single}} &= \frac{N^{\text{reconstructed}}_{\text{single}}}{N^{\text{generated}}_{\text{single}}} && (5.13)\\
&= \frac{N^{\text{reconstructed}}_{\text{single}}}{2 \cdot N^{\text{meas}}_{B\overline{B}} \cdot f^{\text{PDG}}_{00} \cdot \mathcal{B}\left(B^0 \to D^{*-}\ell^+\nu_\ell\right) \cdot \mathcal{B}\left(D^{*-} \to \overline{D}^0\pi^-\right) \cdot 2}, && (5.14)
\end{aligned}$$

where $N^{\text{reconstructed}}_{\text{single}}$ is the MC-corrected number of reconstructed single-tag candidates, $N^{\text{generated}}_{\text{single}}$ the number of generated single-tag candidates in the MC sample, $N^{\text{meas}}_{B\overline{B}}$ the measured number of produced pairs of $B\overline{B}$ in the Belle data set [67], f^{PDG}_{00} the reported PDG value [1] and $\mathcal{B}\left(B^0 \to D^{*-}\ell^+\nu_\ell\right) \cdot \mathcal{B}\left(D^{*-} \to \overline{D}^0\pi^-\right) \cdot 2$ the product branching fraction of the signal decay channel with the factor of 2 accounting for the two lepton channels e^+ and μ^+.

Accordingly, the double-tag efficiency is defined as

$$\begin{aligned}
\epsilon_{\text{double}} &= \frac{N^{\text{reconstructed}}_{\text{double}}}{N^{\text{generated}}_{\text{double}}} && (5.15)\\
&= \frac{N^{\text{reconstructed}}_{\text{double}}}{N^{\text{meas}}_{B\overline{B}} \cdot f^{\text{PDG}}_{00} \cdot \left[\mathcal{B}\left(B^0 \to D^{*-}\ell^+\nu_\ell\right) \cdot \mathcal{B}\left(D^{*-} \to \overline{D}^0\pi^-\right) \cdot 2\right]^2}. && (5.16)
\end{aligned}$$

In this scenario, it is essential to include $N^{\text{meas}}_{B\overline{B}}$ in the denominator, even though our focus is on counting the number of signal decays generated in the MC sample. This is due to the fact that the quantity in the numerator, the number of reconstructed signal candidates, is reweighed as explained in section 4.4. Consequently, the number of $B\overline{B}$ pairs generated cannot be determined simply by the event number contained in the MC sample; rather, the same sample must be used for both the numerator and the denominator.

The term C_{eff} serves as an indicator of whether the detection of a B^0 meson depends on the prior reconstruction of another B^0 in the event. A value of $C_{\text{eff}} = 1$

suggests that the efficiency of detecting each B^0 is uncorrelated in events where both B^0 mesons decay via the signal channel. The *BaBar* analysis for f_{00} finds that these efficiencies are indeed uncorrelated and reports $C_{\text{eff}}^{BaBar} = 0.995 \pm 0.008(\text{stat})$ [2]. However, the methodology behind this calculation is not explicitly stated, preventing a direct comparison with the result presented here.

It is currently observed that the performance of the *Belle* detector and the reconstruction algorithms indicate a positive correlation between these efficiencies. The value obtained using the corrected *Belle* MC sample is

$$C_{\text{eff}} = 1.086 \pm 0.003. \tag{5.17}$$

Furthermore, the findings displayed in Figure 5.6 provide indications of dependencies in the efficiencies on the data acquisition runs, i.e., the reconstruction efficiencies vary from experiment to experiment. To explore this, single and double tag efficiencies were determined for each distinct MC experiment containing $B\overline{B}$ collisions, ranging from experiment 31 through experiment 65. Subsequently, the ratio of efficiencies (C_{eff}) was calculated for each experiment.

The middle plot shows the reconstruction efficiencies for single-tag (yellow) and double-tag (green) candidates. Dashed lines represent the total efficiencies averaged over all experiments. The bars for the statistical error of the individual experiments are too small to be visible, so the variation of the efficiencies over the experiments is not statistical, but inherent in the simulated data.

Corresponding to the middle, the lower plot shows the values of the ratio of efficiencies C_{eff}, individually for each experiment. In this ratio, the statistical errors can be seen as bars, as well as the light-blue area around the dashed line represents the total value of C_{eff}, averaged over the all experiments. Prior to attempting the reweighting of the generic MC samples to correct for the outdated physical parameters, as described in detail in section 4.4, the substantial variation of C_{eff} across experiments proved too significant: a calculated p-value of 2.6×10^{-9} halted the analysis and forced intensive investigations. A satisfactory p-value of 0.493 for the distribution of C_{eff} was attained only after implementing several corrections to the simulated data set.

The obtained value for $C_{\text{eff}} = 1.086 \pm 0.003$ suggests a higher probability of reconstructing a B^0 meson when another signal B^0 has already been identified in the same event. Multiple studies have been carried out in an attempt to explain the underlying causes behind the variations in efficiencies, but none have been successful in finding a final explanation. Reported below are three investigations into factors that could potentially have an impact on the ratio between the reconstruction efficiencies of single-tag and double-tag candidates. These potentials arise since all these factors have a considerable influence on efficiencies and therefore may introduce a correlation between single and double tag efficiencies.

- Divide MC sample into $B^0 \to D^{*-}\, e^+\, \nu_\mu$ decays and $B^0 \to D^{*-}\, \mu^+\, \nu_\mu$ decays
- Examine influence of *HadronB*−skim

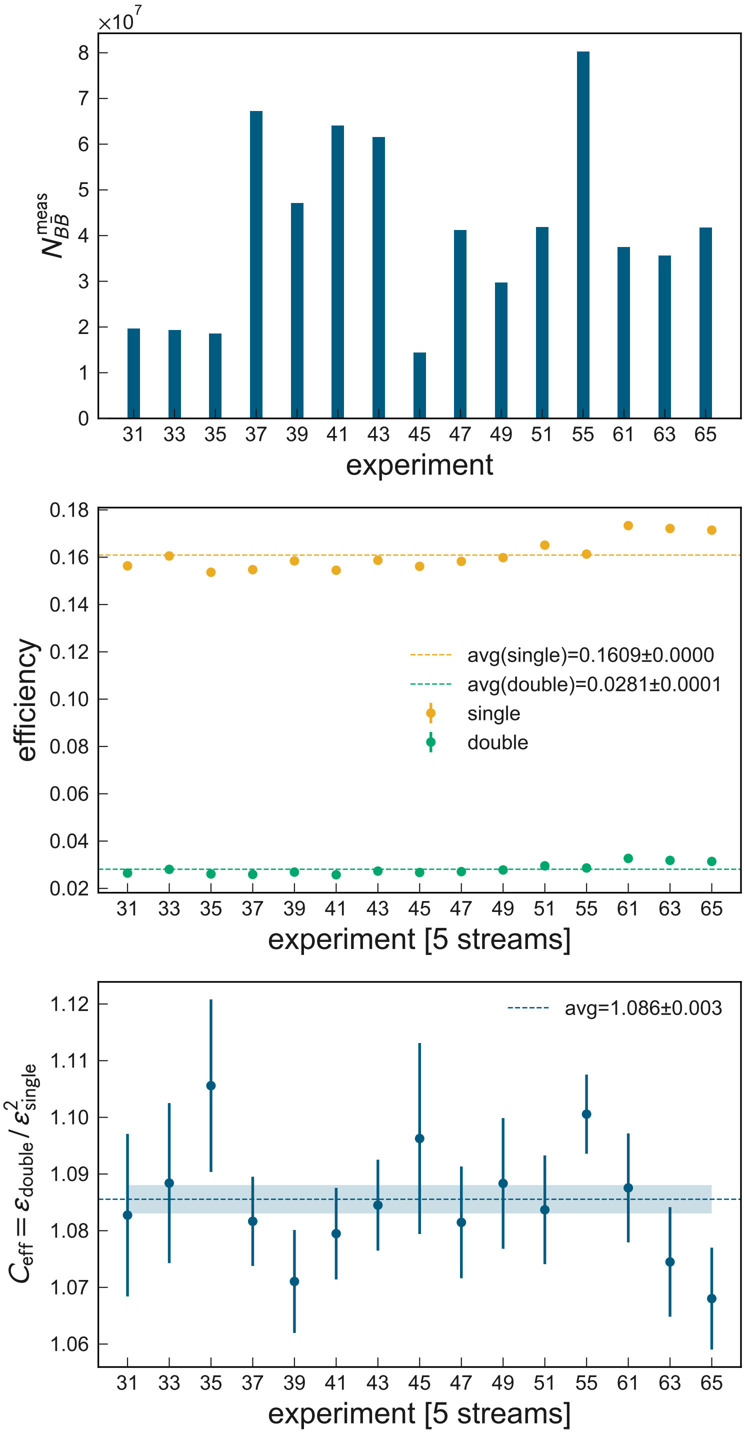

Figure 5.6: Upper: The plot provides the number of measured $N_{B\bar{B}}$ for the experiments 31 − 65. Middle: Efficiencies, represented by the yellow (single-tag) and green (double-tag) lines, are displayed for each distinct experiment. The dashed line illustrates the total single-tag efficiency averaged over the entire dataset. Statistical error bars, though present, are too diminutive to be visible. Lower: The ratio of efficiencies C_{eff} for each distinct experiment, the dashed line represents the averaged C_{eff} −value over the entire data set. The light-blue area corresponds to the statistical uncertainty on the averaged value. The size of the MC sample is five times the luminosity used in the analysis.

	$B^0 \to D^{*-}e^+\nu_e$	$B^0 \to D^{*-}\mu^+\nu_\mu$
ϵ_{single}	0.156 ± 0.000	0.166 ± 0.000
ϵ_{double}	0.026 ± 0.000	0.030 ± 0.000
C_{eff}	1.080 ± 0.005	1.081 ± 0.005

Table 5.1: Lepton-channel study for $C_{\text{eff}} \neq 1$: Efficiencies and the ratio C_{eff} determined separately for electron and muon channel samples. Both values of C_{eff} are below the reported value of 1.086 for the full sample. This discrepancy can be explained by considering that the total sample includes additional events, specifically those events with one B^0 decaying through the electron channel and the other B^0 decaying through the muon channel.

- Determine dependency on track multiplicity

Lepton channels

The primary decay in the signal mode is $B^0 \to D^{*-}\ \ell^+\ \nu_\ell$, where the charged lepton ℓ^+ is either an electron or a muon. The two final state particles interact differently with the detector, resulting in distinct efficiencies. Splitting the data into two samples, one with electrons and one with muons only, allows the reconstruction efficiencies to be calculated individually. Similar to Figure 5.6, the efficiencies and C_{eff} −values are calculated separately for each experiment as well as averaged over all experiments. The results are listed in Table 5.1 and represented in Figure 5.7.

The upper plot in Figure 5.7 shows the efficiencies for single-tag and double-tag decays for the electron-channel as well as the muon-channel. Throughout all experiments, the efficiency of reconstructing the decay $B^0 \to D^{*-}\ \mu^+\ \nu_\mu$ is higher than the efficiency of $B^0 \to D^{*-}\ e^+\ \nu_\mu$. There is an approximate 6% difference between the average efficiencies for single-tag decays in the electron-channel and the muon-channel. Similarly, for double-tag decays, there is a difference of $\sim$ 12%.

Corresponding to the upper plot, the lower plot in Figure 5.7 shows the C_{eff} −values calculated separately for the electron-channel and muon-channel. By taking the ratio of efficiencies individually for each lepton type, the differences disappear, and within the statistical uncertainty, the observed results for C_{eff} align.

Hence, there is no evidence that the reconstruction in the different lepton channels are responsible for the deviation of C_{eff} from 1.

hadronB-skims

The *HadronB*-skim[83] is another possible candidate that could contribute to a correlation in the reconstruction of single-tag and double-tag decays. *HadronB* refers to a collection of cuts applied with the aim of removing non-hadronic e^+e^- events and keeping as many hadronic events as possible. The reported $B\overline{B}$ efficiency is 99.1%. The default skim type, recommended for B analyses, is applied as detailed in section 5.3.

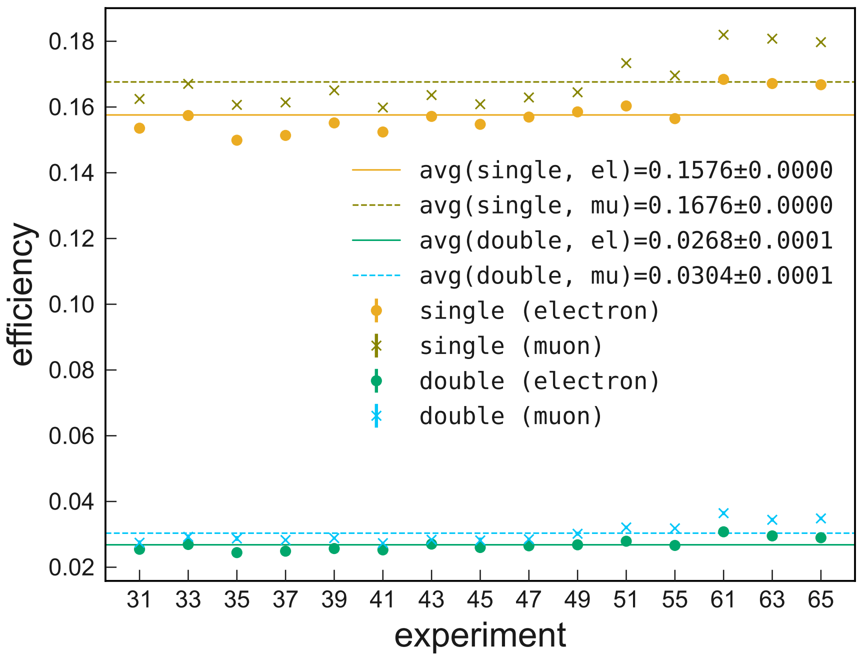

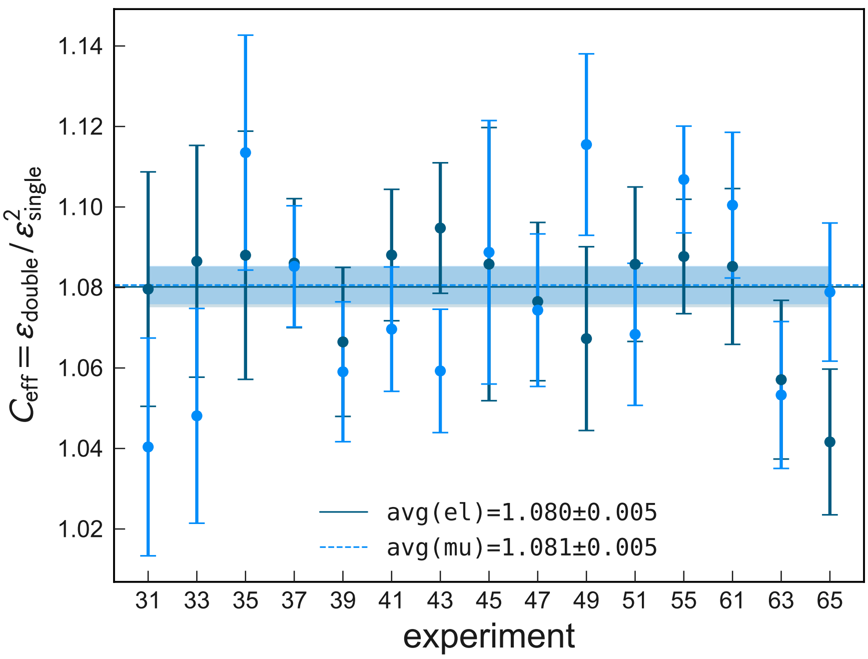

Figure 5.7: Upper: Efficiencies for each individual experiment, calculated separately for electron-channel (single-tag: yellow, double-tag: green) and muon-channel (single-tag: olive, double-tag: light-blue). The average values are shown by the lines in the same colors. Statistical error bars are too small to be seen. Lower: The ratio of efficiencies C_{eff} for each individual experiment, calculated separately for electron channel (dark-blue) and muon-channel (light-blue), the same colored lines represent the total C_{eff} −values averaged over the whole data set. Statistical uncertainties are shown by error bars and transparent areas. The size of the MC sample is five times the luminosity used in the analysis.

Two sets of ntuples from MC are generated, one where the skim is applied and one where it is not, in order to determine the effect of `HadronB`. The ntuples contain the number of generated events, as well as a variable that enumerates the number of true signal B decays occurring per event in order to distinguish between a single-tag and a double-tag event. These numbers are not reweighed as described in section 4.4. This is because the focus here are the differences that arise due to the applied cuts of the skim. The efficiency of the *HadronB*-skim on generated single-tag and double-tag events are

$$\epsilon_{\text{HadronB}}(\text{single}) = 98.1\%, \tag{5.18}$$

$$\epsilon_{\text{HadronB}}(\text{double}) = 96.2\%. \tag{5.19}$$

Obviously, the default skim has a lower efficiency regarding the signal decay mode of this analysis than compared to all $B\overline{B}$ events. However, *HadronB* does not introduce a correlation between single-tag and double-tag efficiency reconstruction, since the square of the single-tag efficiency is equal to the double-tag efficiency,

$$\epsilon^2_{\text{HadronB}}(\text{single}) = 96.3\%, \tag{5.20}$$

as expected. To conclude, the collection of cuts of the *HadronB*-skim are not responsible for the correlation between the reconstruction efficiencies of single-tag and double-tag decays.

Track multiplicity

The third investigation carried out to find the cause of the behavior of efficiencies is the study of track multiplicities in events with single-tag and double-tag decays. The influence of the track count in the event on signal efficiencies is investigated. This requires a different approach to calculating the efficiencies as described in Equation 5.13 to Equation 5.16. In order to decompose the total efficiency into bins of track multiplicity, the number of generated signal decays must be deducted from the MC samples directly, otherwise the information on the number tracks is not available. Therefore, the denominator $N^{\text{generated}}$ in

$$\epsilon = \frac{N^{\text{reconstructed}}}{N^{\text{generated}}} \tag{5.21}$$

is obtained from `mDST` by the module `fillParticleListFromMC` paired with the requirement that the B^0 is decaying via the signal mode.

The MC corrections described in section section 4.4 are applied to both the reconstructed candidates and the generated decays. However, the reconstruction efficiency corrections (lepton PID and pion tracking efficiency) are exclusively applied to the reconstructed candidates.

The variable to determine the track multiplicity is defined as the number of charged final state particles ($e^-, \mu^-, \pi^-, K^-, p, \overline{\Sigma}, \overline{\Xi}, \overline{\Omega}$) per event, which are produced by the generator (*primary MCParticle*). [1]

[1] Using generic `nTracks` or `nCleanedTracks` variables for `basf2` is not practical in this context, since it requires counting the generated tracks in the event, not just the ones that are reconstructed.

The track multiplicities thus defined for single-tag and double-tag decays are depicted in the upper plot of Figure 5.8. For both tag types, the most likely multiplicity per event is 8. There are only events with an even multiplicity because the B^0 is a neutral particle.

In the case of single-tag decays, the distribution is significantly wider, ranging from 2 to 24. On the other hand, double-tag decay events are ranging from 4 to 16. To facilitate comparison, the track multiplicity is plotted using a logarithmic scale.

Single-tag and double-tag efficiencies are computed in bins of track multiplicity, combining one even and one odd multiplicity into a single bin. These efficiencies are then plotted alongside the total efficiencies. The result is shown in the lower plot in Figure 5.8.

This study reveals a significant correlation between multiplicity and reconstruction efficiencies. The single tag efficiency ranges from $\epsilon_{\text{single}}(2 \text{ tracks}) = 0.21 \pm 0.02$ to $\epsilon_{\text{single}}(22 \text{ tracks}) = 0.09 \pm 0.04$, i.e. the probability to correctly reconstruct a signal decay is roughly twofold higher for low-multiplicity events compared to high-multiplicity events. However, same applies for double tag decays. Here, the efficiency ranges from $\epsilon_{\text{double}}(4 \text{ tracks}) = 0.04 \pm 0.00$ to $\epsilon_{\text{double}}(14 \text{ tracks}) = 0.02 \pm 0.01$. Within the margin of uncertainty, a comparable factor is observed between the lowest and highest event multiplicities. Consequently, the study on multiplicity also does not offer an explanation for $C_{\text{eff}} \neq 1$.

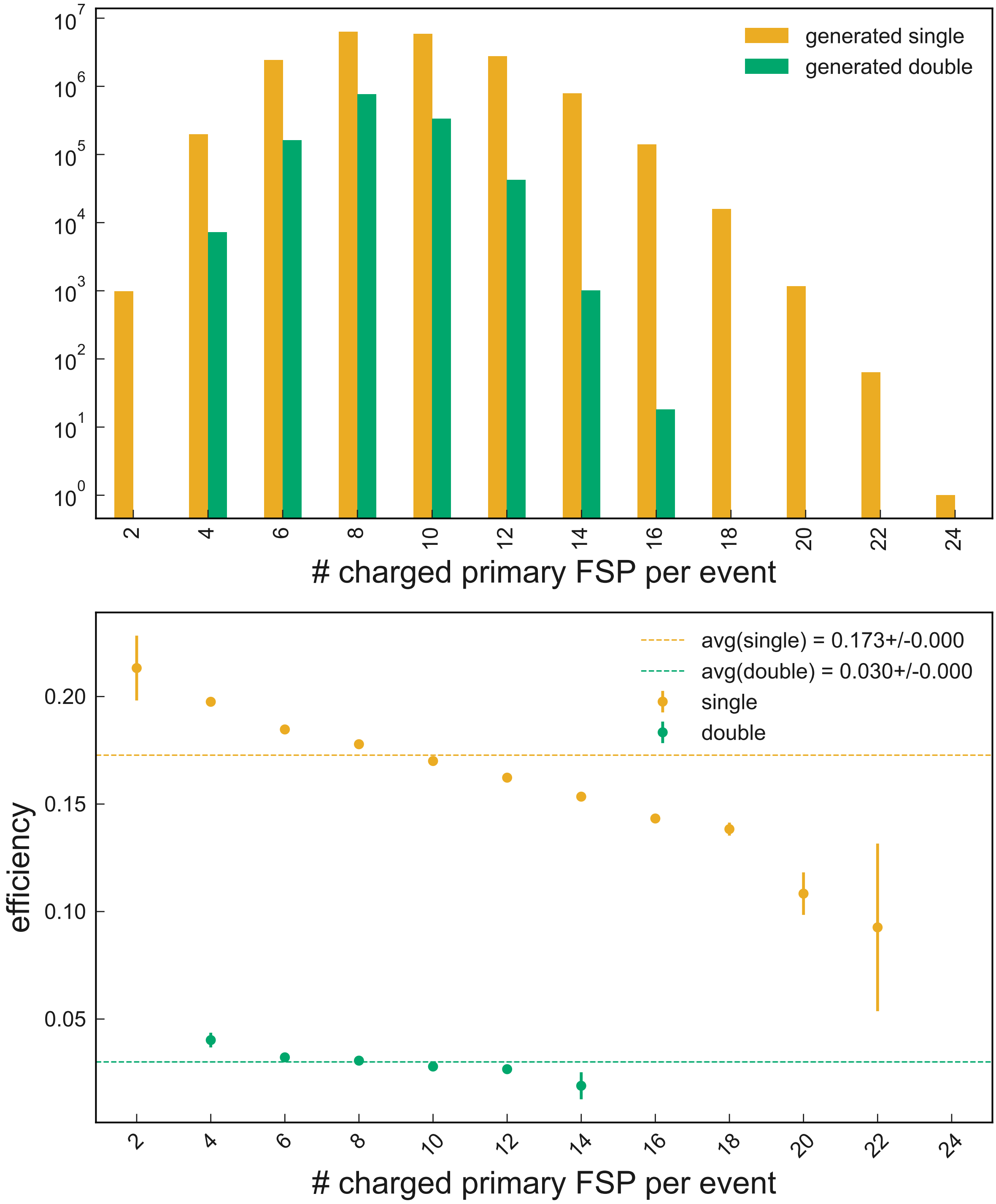

Figure 5.8: Upper: The track multiplicity (number of charged primary final state particles) per single-tag (yellow) and double-tag (green) events in log-scale. Both distributions peak at 8 tracks per event. Lower: Single-tag (yellow) and double-tag (green) efficiencies in bins of the track multiplicity. The dashed lines in the same colors represent the total efficiencies.

Chapter 6

Signal Yield Extraction

This chapter outlines the extraction of the number of signal-tag and double-tag decays from experimental data. The fit variable is introduced. Subsequently, the different types of backgrounds and their distributions are described. The chapter concludes by explaining the fit procedure, a binned extended maximum likelihood estimation, and its validation. A detailed treatise of fitting with maximum likelihood estimators is found in [85].

6.1 Fit variable

The variable that is used to discriminate between signal and background candidates is the missing mass squared that is calculated as

$$M_{\text{miss}}^2 = (P_B - P_\ell - P_{D^*})^2 \tag{6.1}$$

$$= \left(\frac{\sqrt{s}}{2} - E_\ell - E_{D^*}\right)^2 - (\vec{p}_\ell + \vec{p}_{D^*})^2\,, \tag{6.2}$$

where P denotes the 4-momentum, $\sqrt{s}$ the center-of-mass energy, E the energy and $\vec{p}$ the 3-momentum vector. The undetectable neutrino carries energy and momentum that is missing for the full reconstruction of the kinematic information of the B meson. It is therefore assumed that the B meson is at rest in the center-of-mass frame:

$$P_B = \begin{pmatrix} E_B \\ \vec{p}_B \end{pmatrix} = \begin{pmatrix} \sqrt{s}/2 \\ 0 \end{pmatrix}. \tag{6.3}$$

This is justified by the relatively small magnitude of the 3-momentum of the B meson, on average around 0.34 GeV, compared to the momenta of the lepton and the D^*, having typically momenta of several GeV [36].

Due to the missing momentum carried by the neutrino, the M_{miss}^2 distribution will peak at 0 for signal decays, while it will have a broad distribution with a long tail to negative values for combinatorial background candidates, with a hard drop to 0 for kinematic reasons.

As described in section 5.1, the objective of this analysis is to derive f_{00}, the branching fraction of $\Upsilon(4S) \to B^0\overline{B}^0$. The notation following Equation 5.3

clarifies that the effective measure of this analysis is the counting of single and double tag candidates. This counting is accomplished by integrating the fitted curve over the M^2_{miss} distributions corresponding to both tagging types. The fit for the single-tag candidates is straightforward, a simple fit to the 1-dimensional distribution. In contrast to the approach taken in the *BaBar* analysis [2], a different procedure is used for the double tag candidates: a fit is applied to the two-dimensional distribution, with each axis representing the M^2_{miss} of the respective B^0 candidates.

6.2 Types of backgrounds

The background is drawn from three different kinds of events: continuum, charged B and neutral B mesons. Essential for the extraction of f_{00} is the behavior of the background in the signal region. We therefore categorize the events into *peaking* or *non-peaking* background by plotting the M^2_{miss} distributions in Figure 6.1. The background components derived from this plot are specified in the following list:

- *uds*: Contributions from the three lightest quarks are part of the non-resonant continuum, i.e. no B meson pair was created in the e^+e^- collision, but a pair of $u\overline{u}$, $d\overline{d}$ or $s\overline{s}$. The much lighter masses of these states produce a significantly different event shape compared to $B\overline{B}$ pairs. The event shape of these events, given the smaller masses of the produced mesons, are two back-to-back jets, much different to the sphere-like shapes of $B\overline{B}$ pairs. The M^2_{miss} distribution for this background is overall flat.

- *charm*: Also part of the continuum, but the produced X_c mesons have higher masses, which is why they are distinguished from *uds* in this analysis. The M^2_{miss} distribution for this background also behaves differently in that there is a noticeable peak in the signal region.

- *charged* $B^- \to D^{**}\ell\ \nu$: Contribution from charged B mesons decaying semileptonically to orbitally excited charmed mesons. There are four possible states of D^{**} coming from B^-: D^0_1, D'^0_1, D^{*0}_2, D^{*0}_0. In the D^{**} decays, an additional slow pion is produced. In the attempt to reconstruct the B^0 meson, the combination of a correct lepton and the slow pion from the D^{**} decay or from the D^* decay, the missing mass squared in this case would add up to the mass of the pion, which is approximately 140 MeV. However, due to the low resolution of the signal peak (~ 1 GeV), these events cannot be resolved and are thus indistinguishable from signal.

- *charged other*: All other combinations of leptons and pions coming from B^- decays are grouped together and as can be seen in Figure 6.1, events with $M^2_{\text{miss}} \simeq 0$ GeV also accumulate more frequently.

- *mixed* $B^0 \to D\ \ell\ \nu$, *mixed* $B^0 \to D^*\ \ell\ \nu$ and *mixed* $B^0 \to D^{**}\ \ell\ \nu$: The qualitative M^2_{miss} distributions are similar for all semileptonic charmed decays of the neutral B meson: fairly broadly distributed with a negligible accumulation in the signal region, hence all three types of events can be treated as

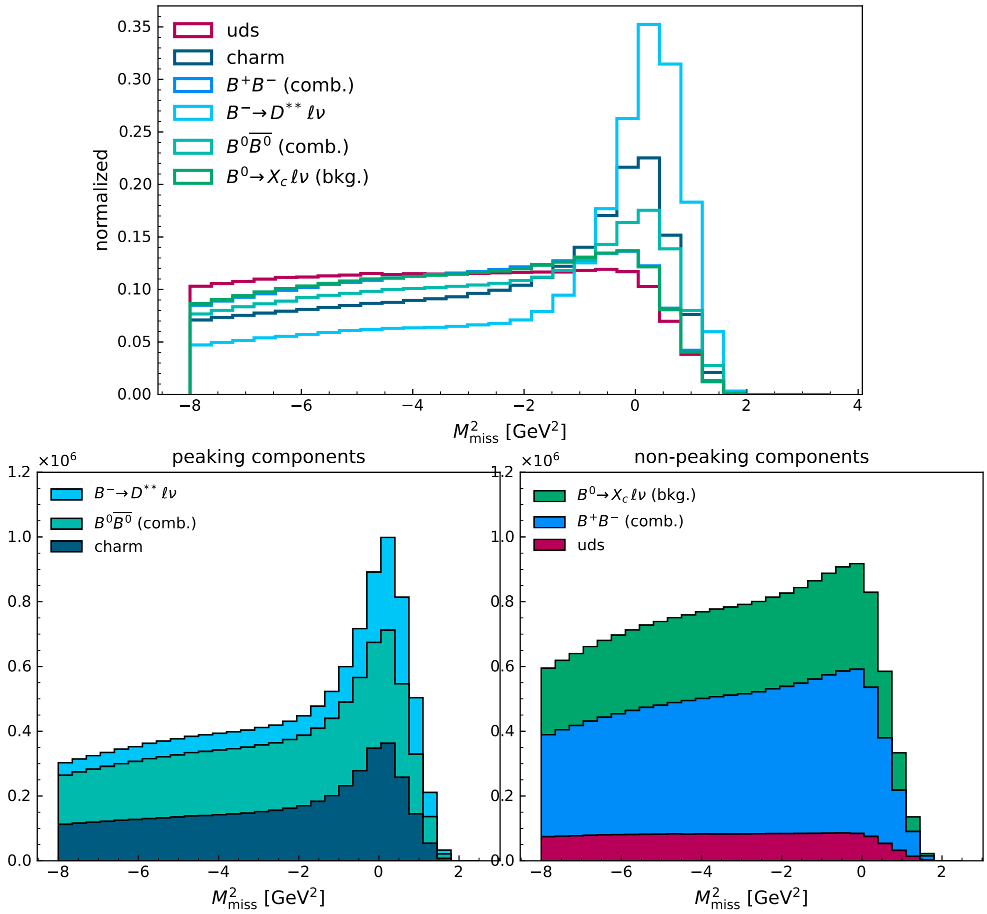

Figure 6.1: Top: Comparison of all background components. Stacked plot of all peaking components (bottom left) and non-peaking components (bottom right).

non-peaking background.

- *mixed other*: All other combinations of leptons and pions coming from B^0 decays are grouped together and since there is a small but noticeable accumulation at $M^2_{\rm miss}$ =0 GeV, events falling into this category is also considered as peaking background.

To extract the number of double-tag decays, a two-dimensional distribution is fitted as described in section 6.1. Hence, we have events with two B^0 candidates for which there is a type of background, which is exists only for double-tag events:

- *semicombinatoric background*: This background only occurring for double-tag events is the combination of one correctly reconstructed and one falsely reconstructed B^0 signal decay.

6.3 Signal yields

To determine f_{00}, it is necessary to extract the contributions of signal decays to the single-tag and double-tag distributions of the missing mass squared variable obtained from experimental data. These values are referred to as the signal yields

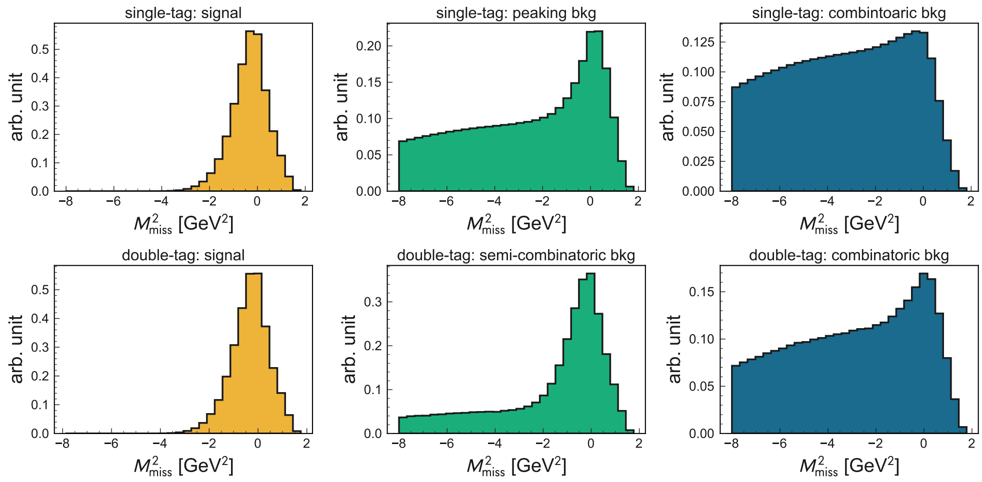

Figure 6.2: M^2_{miss} distributions for the categories used to create fit templates. Upper: single-tag decays (signal, peaking background and combinatoric background). Lower: double-tag decays (signal, semi-combinatoric background and combinatoric background). Shown here is the projection on one B meson. A 3-dimensional representation of the double-tag distributions is shown in Figure 6.3

for single-tag and double-tag.

The extraction requires the underlying probability density functions (PDF) that describe the shape of the distributions of the signal and background components. In this analysis, the shapes of the PDFs are not described analytically, but are obtained directly from the simulated distributions. This procedure is known as template fitting.

The only free parameter of the PDF is thus the normalization which is optimized by seeking the maximum likelihood that the sum of the PDF describe the data best. As it is usual in particle physics, the distributions are represented in binned histograms, consequently binned extended maximum likelihood fits are performed to extract the signal yields. While it is a one-dimensional fit for single-tags, the fit for double-tags is carried out in two dimensions.

The shapes of the templates are derived from 5 streams of the complete generic *Belle* MC sample. The entire fit procedure is carried out using the RooFit toolkit [86].

To generate fitting templates, the reconstructed decays are divided into categories. For both single-tag and double-tag decays, there are three categories each: signal, peaking background, and non-peaking background for single-tag; and signal, semi-combinatorial background, and combinatorial background for double-tag. The template category distributions are shown in Figure 6.2. PDF templates are individually created from MC for all three single-tag categories and three double-tag categories.

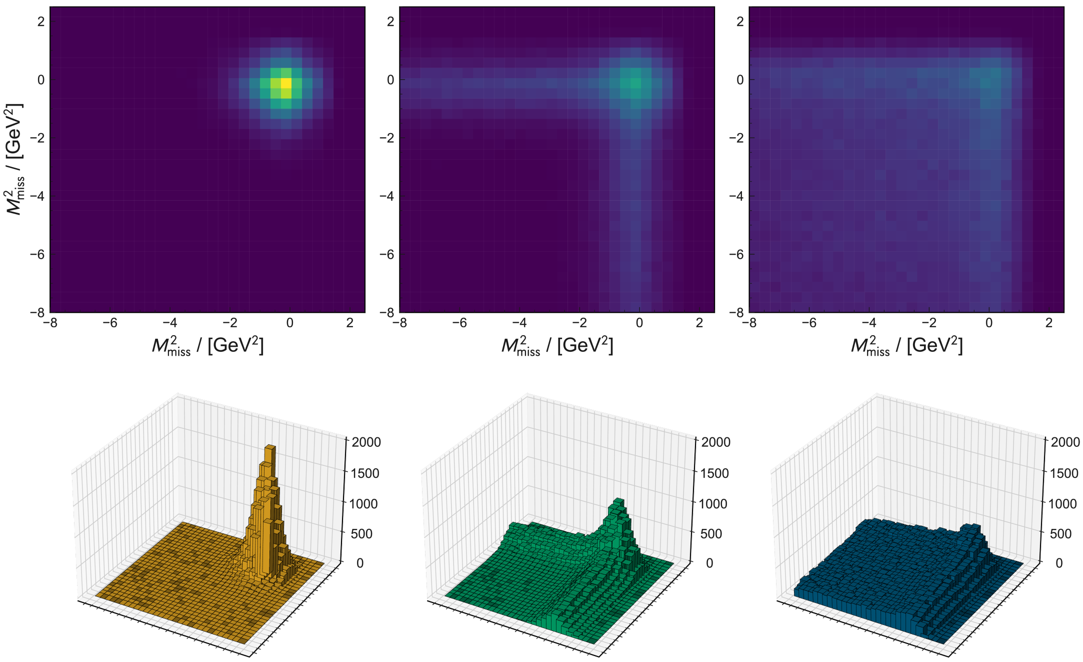

Figure 6.3: 2-dimensional (upper) and 3-dimensional (lower) representation of the M^2_{miss} distributions of double-tag candidates, for the categories used to create fit templates.

6.4 Fit validation

Toy MC samples are employed to evaluate potential biases within the fits. This involves generating missing mass square distributions by sampling from the fit templates that have been previously fitted to data. The number of generated candidates is drawn from a Poisson distribution with the mean set to the expected number of candidates. A total of 10 000 samples are generated for each tag type. Subsequently, the samples are fitted, and for each fit to the sample distribution, the weighted residuals, referred to as pull, is calculated as

$$\text{pull} = \frac{N_{\text{fit}} - N_{\text{expected}}}{\sigma_{\text{fit}}}, \tag{6.4}$$

where N_{fit} is the yield of candidates from the fit, N_{expected} the generated number of candidates and σ_{fit} the fit uncertainty. The distribution of all pull-values serves as a diagnostic tool for assessing the quality of the fit. The mean of the pull distribution offers insight into the extent to which the fitted values deviate from the expected values. If the mean is close to 0, it indicates that, on average, the fitted values align well with the expected values, pointing to the absence of a systematic bias in the fit. A width of 1 implies that the spread of the pull distribution is comparable to the uncertainties associated with the fit. If the width is larger than 1, it indicates that the uncertainties estimated by the fit are underestimated.

The result of the toy study for fitting the single-tag M^2_{miss} distribution is

$$\mu_{\text{pull}}(\text{single}) = 0.029 \pm 0.003, \tag{6.5}$$
$$\sigma_{\text{pull}}(\text{single}) = 1.014 \pm 0.002, \tag{6.6}$$
$$\tag{6.7}$$

and for the double-tag fit

$$\mu_{\text{pull}}(\text{double}) = -0.002 \pm 0.003, \tag{6.8}$$
$$\sigma_{\text{pull}}(\text{double}) = \quad 1.000 \pm 0.002. \tag{6.9}$$

These values are represented in Figure 6.4 and Figure 6.5 for single-tag and double-tag, respectively.

The analysis of the pull distributions suggests a negligible bias for the single-tag signal, given the magnitude of 2.9% compared to the relative fit uncertainty of about 0.1%. This is still valid if accepting the underestimation of the uncertainty of the fit by 1.4%. According to the toy MC study, the double-tag fit is free of bias even without neglect and the uncertainty is accurately determined.

Comparable results are found for fits to the data samples of the individual experiments. The outcome of the toy MC study for each experiment is represented in Figure 6.6.

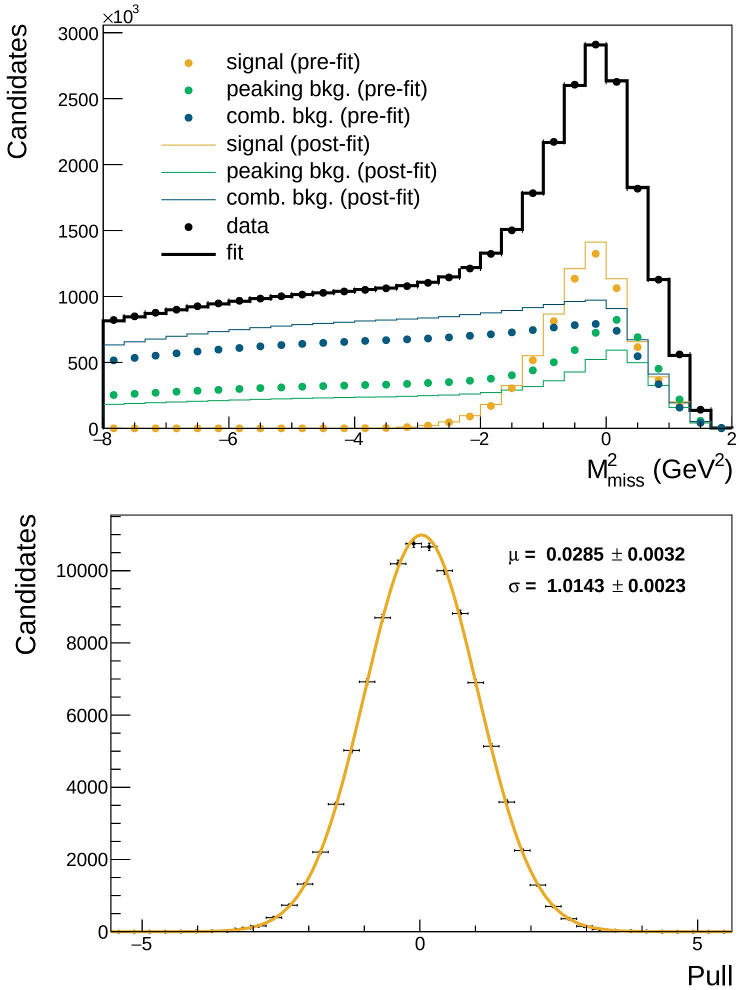

Figure 6.4: Upper: Fit to the missing mass squared distribution of single tag candidates. The plot shows the distributions of the three fit components: signal, peaking background and combinatorial background, both before (dots) and after (lines) fitting. Yellow represents the signal, green the peaking background and blue the combinatorial background. Lower: The pulls of the signal yield from 10 000 toy MC samples fitted by a Gaussian function. The mean and width of the Gaussian indicate a negligible bias of 2.9% of the uncertainty of the fit, which is underestimated by 1.4%.

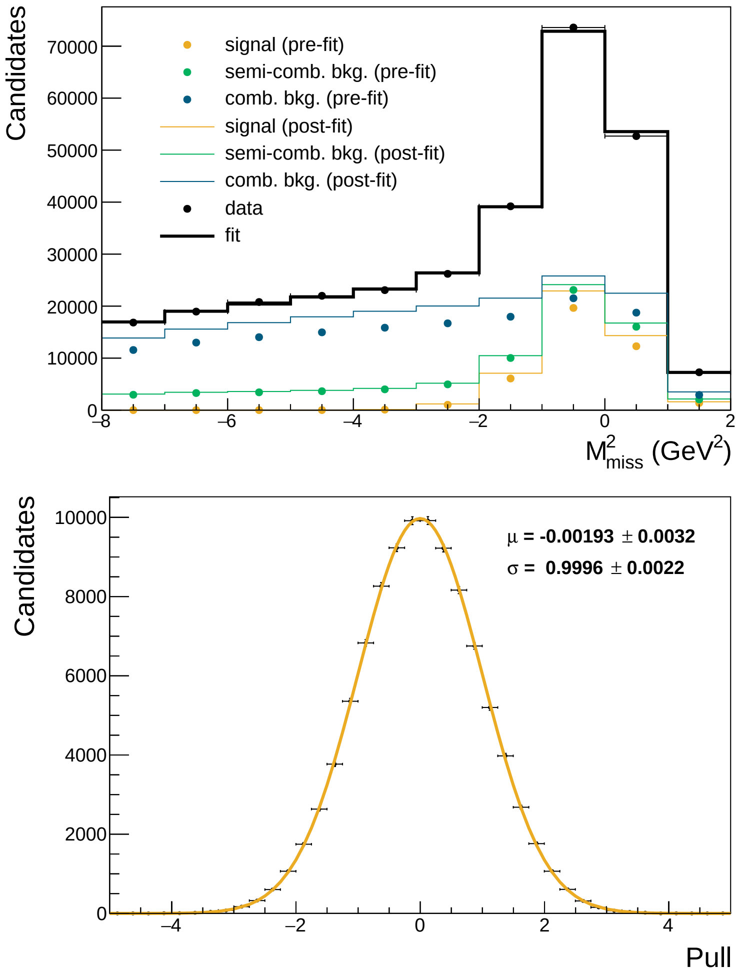

Figure 6.5: Upper: Fit to the missing mass squared distribution of double tag candidates, featuring the projection onto one B^0 (The projection onto the other B^0 gives a comparable plot). The plot shows the distributions of the three fit components: signal, semi-combinatoric background and combinatorial background, both before (dots) and after (lines) fitting. Yellow represents the signal, green the semi-combinatoric background and blue the combinatorial background. Lower: The pulls of the signal yield from 10 000 toy MC samples, fitted by a Gaussian function. The mean and width of the Gaussian distribution signify a standard normal distribution, indicating an unbiased fit with accurately determined uncertainty.

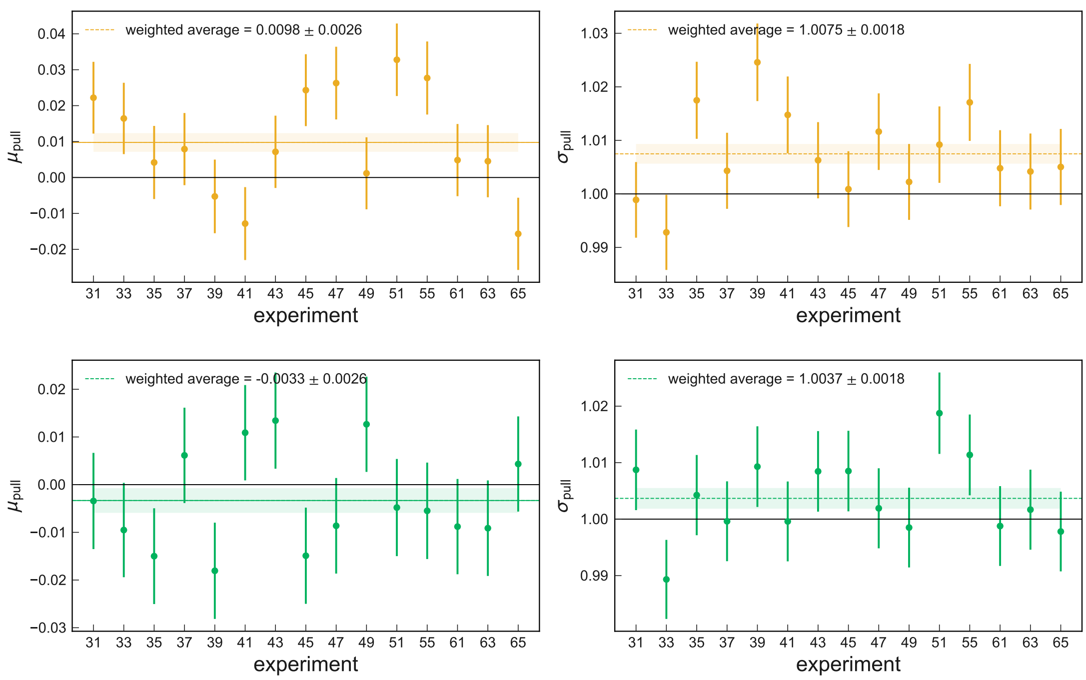

Figure 6.6: The outcome of the toy MC study for single-tag decays (yellow) and double-tag decays (green). The left plots show the mean values and the right plots the widths of the Gaussian distributions fitted to the pulls. The biases towards underestimated fit yields of 1% of the uncertainty of the fit for single-tag or 0.8% for double-tag are negligible.

Chapter 7

Validation of Analysis Method

Initial reconstruction efficiency studies have revealed an unexpected behavior. The variance of C_{eff} across experiments was too significant, indicating that the assumption of constancy would not yield a valid result, as shown in Figure 5.6. A proposed solution was to split the measurement of f_{00} into experiment-dependent measurements, rather than performing a *global* measurement. In the context of this thesis, global refers to analyzing the entire data sample collectively, without distinguishing individual experiments.

However, for the experiment-dependent measurement, the value of C_{eff} would be determined for each experiment individually, followed by measurements of f_{00} for each experiment, respectively. The final result would be the statistically weighted average of all experiment-dependent f_{00} results.

The outcome of the validity studies described in this chapter will determine the methodology selected for the measurement of f_{00}. If a dependency among individual experiments persists, the measurement is performed separately for each experiment. However, if the experiment-dependent f_{00} results are shown to be congruent between experiments, the global, run-independent measurement is carried out and its outcome will be regarded as the final result for f_{00}. The experiment-based result will then serve as a validation measure for the global outcome.

7.1 Semi-unblinding

Everything presented in this chapter is still blind to the measurement of f_{00}. An examination is carried out on experimental Belle data, involving the following procedures:

- The M^2_{miss} distributions of simulated and experimental data are compared. In this way, the quality of the description of the data by the simulation is generally analyzed. By making the comparison before and after the application of the corrections, the effect of the reweighting on the agreement can also be studied.

- The single-tag signal branching ratio is measured. This validation serves to confirm the extraction of the signal yield and assess the credibility of the single-tag reconstruction efficiency.
- Another validation procedure is to calculate f_{00} for each experiment, with each individual result being randomized with the same randomly generated number. The purpose of this investigation is to decide whether the determination of f_{00} requires distinct measurements for each individual experiment since the reconstruction efficiencies exhibit such dependency.

The following statistical metrics are used frequently in this section. For the individual results x_{exp} of each of the N experiments, the *weighted average* $\overline{x} = (x_1, ...x_N)$ is calculated by taking the arithmetic mean of $\vec{x}$, where each value is weighted according to its associated reciprocal variance $w_{\text{exp}} = 1/\sigma^2_{\text{exp}}$:

$$\overline{x} = \frac{\sum_{\text{exp}} x_{\text{exp}} \cdot w_{\text{exp}}}{\sum_{\text{exp}} w_{\text{exp}}}. \tag{7.1}$$

To analyze whether the results of the experiment-depending measurements are statistically consistent weighted average, a χ^2 test is used, calculated as

$$\chi^2 = \frac{\sum_{\text{exp}} \left(x_{\text{exp}} - \overline{x}\right)^2}{\sum_{\text{exp}} \sigma^2_{\text{exp}} + \sigma^2_{\overline{x}}}, \tag{7.2}$$

where $\sigma_{\overline{x}}$ is the uncertainty on the weighted average.

7.2 Data−MC agreement

In section 4.4 it was outlined what the principle considerations are when reweighting the MC sample. It is possible to assess how well the two data sets match with respect to the selected variables by comparing the distributions from the data and from the MC.

The comparison of M^2_{miss} distributions from data and MC for partially reconstructed B^0 are shown in Figure 7.1 and Figure 7.2 for single-tag and double-tag events, respectively.

For single-tag candidates, the data from the MC sample were divided into distinct components, to each of which specific or common weights were applied, described in detail in section 6.2. Double-tag candidates reconstructed from MC, on the other hand, are not quite so finely divided. Here, a distinction is made between uds, charm, combinatorial background of charged and neutral B-meson events and the semi-combinatorial background components.

The figure shows two plots, on the left the genuine state is shown, meaning that no MC corrections are applied yet. The right plot shows the state after the MC is reweighed according to the corrections mentioned in section 4.4.

The small plots below the M^2_{miss} plots represent the relative residuals between the MC and experimental data distributions above. The relative residuals observed for

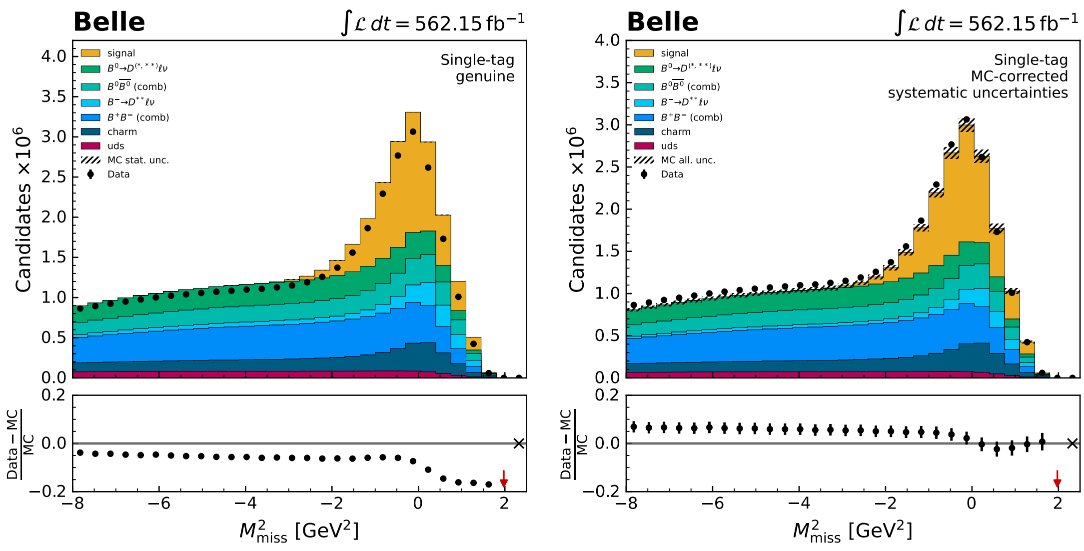

Figure 7.1: Comparison of M^2_{miss} distribution for single-tag candidates reconstructed from MC and experimental data. Left: genuine MC (no weights applied). Right: corrected MC (reweighed) incorporating the systematic uncertainties of all correction factors (outlined in section 8.1). Additionally, the relative residuals of data and MC for each bin is shown under each plot.

simulated data, which ideally match the experimental data, are expected to align with zero. However, this analysis shows a deviation from this expectation both before and after reweighting.

An improvement is observed for single tag candidates. While an overall normalization discrepancy remains, its significance is mitigated by focusing on the shape of the distribution rather than the absolute normalization. In particular, the normalization is determined by the fit, which depends mostly on the shape of the distribution.

For single-tag candidates, the fits show relative consistency (except for normalization) for negative M^2_{miss} values, but shows discrepancies for positive M^2_{miss} values.

For double-tag candidates, the scenario prior to reweighting appears less pronounced than for single-tag candidates. The reweighting procedure mainly affects the normalization, although with a slight improvement in the alignment of the distribution shapes, despite the persistent normalization discrepancy similar to that for single tag candidates.

These deviations are accepted and considered as a source of systematic uncertainty. This approach is based on the observation of a similar tendency in side channels, see subsection 7.5.2. Since one side channel only contains background candidates, the hypothesis can be derived that the deviation is due to an incorrect modelling of the background. In subsection 8.1.5, corrections are determined on the basis of these side channels, used for the estimation of the systematic effect of the data−MC disagreement in the M^2_{miss} distribution.

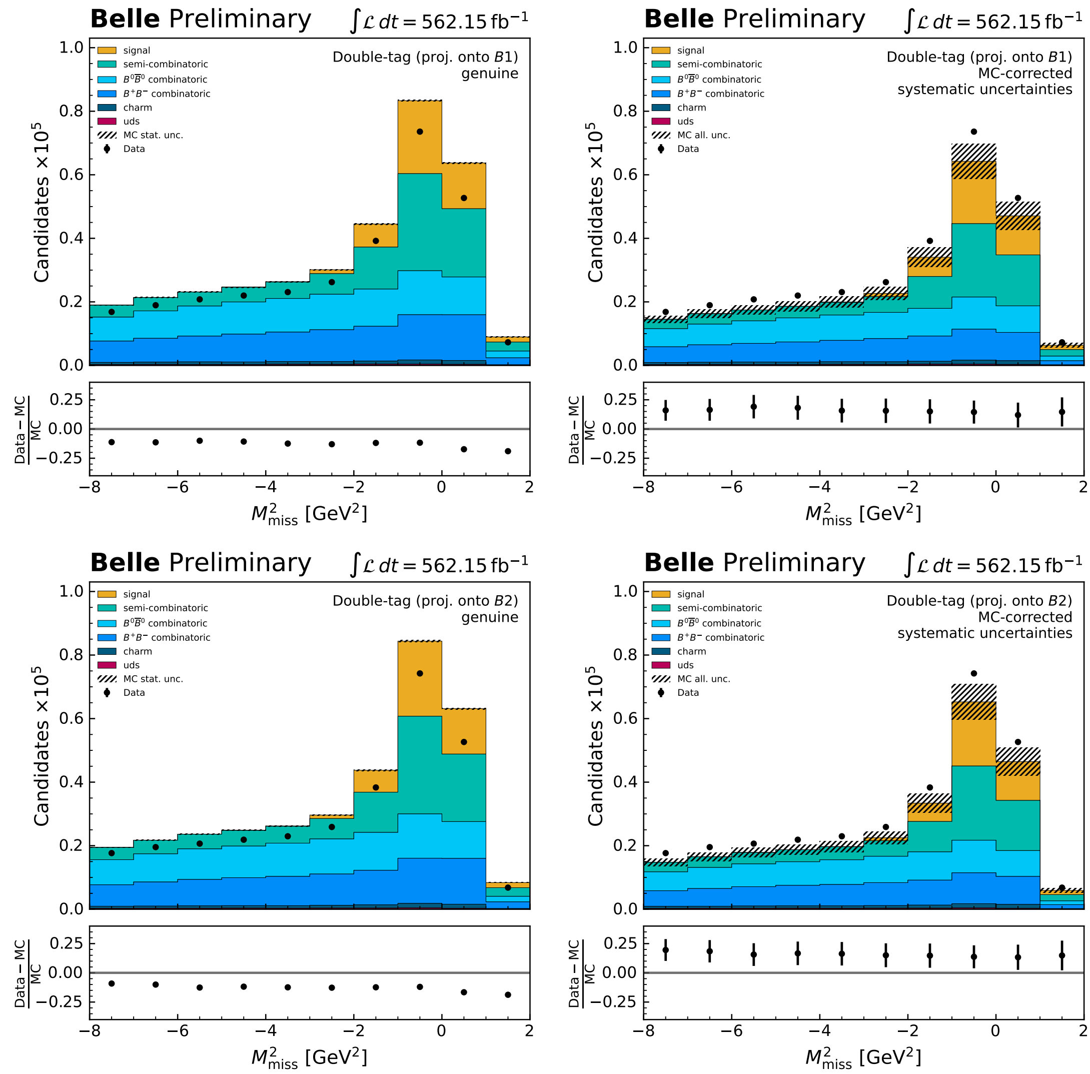

Figure 7.2: Comparison of M^2_{miss} distribution for double-tag candidates reconstructed from MC and experimental data. The top row depicts the projection onto one B^0, while the bottom row illustrates the projection onto the other B^0. Left: genuine MC (no weights applied). Right: corrected MC (reweighed) incorporating the systematic uncertainties of all correction factors (outlined in section 8.1). Additionally, the relative residuals of data and MC for each bin is shown under each plot.

7.3 Single-tag signal branching ratio

The objective of this investigation is to validate the entire signal yield extraction procedure and to ascertain the simulation-determined single-tag efficiency. To examine this, the branching ratio of the signal decay chain can be quantified. Solving Equation 5.1 for the branching fractions leads to the resulting product branching fraction expressed as follows:

$$\begin{aligned}\mathcal{B}_{\text{signal}} &= \mathcal{B}\left(\Upsilon(4S) \to B^0\overline{B}^0\right) \times \mathcal{B}\left(B^0 \to D^{*-}\ell^+\nu_\ell\right) \times \mathcal{B}\left(D^{*-} \to \overline{D}^0\pi^-\right)\\ &= \frac{N_{\text{single}}}{4N_{B\overline{B}}\epsilon_{\text{single}}},\end{aligned} \tag{7.3}$$

where N_{single} is the number of reconstructed single-tag decays, $N_{B\overline{B}}$ denotes the number of produced pairs of B mesons in data and ϵ_{single} stands for the single-tag efficiency. The factor $2 \cdot 2 = 4$ is derived from the number of lepton channels and the number of B mesons per event. The product of the branching ratios, projected from the values of the PDG, is calculated to

$$\mathcal{B}_{\text{signal}}^{\text{PDG}} = \left(1.701 \pm 0.070\right) \times 10^{-2}, \tag{7.4}$$

with the individual branching ratios provided in [1] as $\mathcal{B}\left(\Upsilon(4S) \to B^0\overline{B}^0\right) = 0.487 \pm 0.013$, $\mathcal{B}\left(B^0 \to D^{*-}\ell^+\nu_\ell\right) = 0.0516 \pm 0.0016$ and $\mathcal{B}\left(D^{*-} \to \overline{D}^0\pi^-\right) = 0.677 \pm 0.005$.

The measurement of $\mathcal{B}_{\text{signal}}$ in Equation 7.3 can be performed on data without revealing f_{00}, the result of the analysis. The global result, i.e. without differentiation among individual experiments, is measured to be

$$\begin{aligned}\mathcal{B}_{\text{signal}}^{\text{meas.}} &= \left(1.794 \pm 0.002_{\text{stat}} \pm 0.064_{\text{syst}}\right) \times 10^{-2} &(7.5)\\ &= \left(1.794 \pm 0.064\right) \times 10^{-2}, &(7.6)\end{aligned}$$

where the systematic uncertainty is determined as explained in section 8.1. Additionally, following the results of [87], the lepton tracking efficiency is prescribed with a relative systematic uncertainty of 0.35%.

The validation result translates to a discrepancy between the measured value and the expected PDG value of less than one standard deviation. It is represented in Figure 7.3. A plausible explanation for this deviation could be the relatively imprecise determined branching fraction of $B^0 \to D^{*-}\ell^+\nu_\ell$. The values for this branching fraction listed in [1] fall within the range of 4.69 ± 0.34 to 6.1 ± 0.4.

7.4 Measurement of the normalized f_{00}

The aim of this validation study is to assess whether the observed variation in the efficiency ratio C_{eff} between experiments is acceptable and not due to methodological errors. At the beginning of this chapter, it is outlined that the determination of f_{00} may necessitate experiment-specific measurements. Following this strategy,

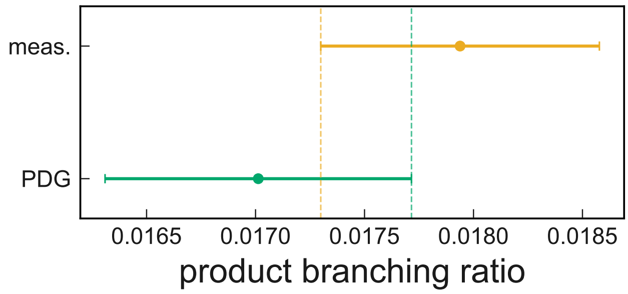

Figure 7.3: The measured value of the product signal branching ratio $\mathcal{B}_{\text{signal}}$, depicted in yellow, and the expected value given by PDG[1], depicted in green. The bars represent the total uncertainties. The discrepancy corresponds to 0.97σ.

the measurements for each distinct experiment is made. Prior to examining the outcome, the results for the yield factor, defined as,

$$f_{\text{yield}}\left(\text{exp}\right) = \frac{1}{N_{B\overline{B}}\left(\text{exp}\right)} \frac{N^2_{\text{single}}\left(\text{exp}\right)}{N_{\text{double}}\left(\text{exp}\right)}, \tag{7.7}$$

for each experiment are normalized based on the outcome of a particular reference experiment, where $N_{B\overline{B}}$ denotes the number of $B\overline{B}$ events in the sample, and $N_{\text{single/double}}$ the number of reconstructed signal and double tag candidates per sample.

In this context, the experiment with the lowest statistical uncertainty is selected as reference, which is experiment 55.

The normalization of individual results is crucial to maintain the confidentiality of the outcomes and ensure the continuation of a blind analysis. The basic idea of this crosscheck is eventually the measurement of f_{00} for each individual experiment $f_{00}(\text{exp})$, which before inspection, is divided by the outcome of experiment 55, so that

$$f_{00}^{\text{norm}}\left(\text{exp}\right) = \frac{f_{00}\left(\text{exp}\right)}{f_{00}\left(55\right)}. \tag{7.8}$$

Given that $\mathcal{B}\big(\Upsilon(4S) \to B^0\overline{B}^0\big)$ is a physical constant, it follows that the distribution of $f_{00}^{\text{norm}}\left(\text{exp}\right)$ must align with 1. Figure 7.4 depicts the decomposition of this crosscheck.

The upper plot presents C_{eff}, determined from simulated data, for each distinct experiment. The spread of C_{eff} across experiments is quantified with $\chi^2|_{\text{mean}} = 14.0$ with respect to the mean, corresponding to a $p-$value of $p = 0.53$ for 15 samples.

The center plot shows the normalized yield factor f_{yield}, a quantity obtained from fitting experimental data. The variation observed in this distribution adheres closely to the anticipated value of 1, substantiated by a p-value of approximately $p = 0.47$.

Following, the lower plot represents the experiment-wise product of the values in the aforementioned plots, giving the result of the normalized evaluation of f_{00}

for each specific experiment. Within the confines of statistical uncertainty, the normalized values align with 1, since the p-value is larger than 0.63.

In conclusion, this study demonstrates the accurate determination of C_{eff} values derived from MC. The test showed consistency between the experiment-dependent C_{eff} values and the subsequent measurement of the normalized values of f_{00}.

7.5 Control channels

This section is dedicated to the validation of the analysis method by investigating control channels. The control channels investigated are: the wrong sign combination and the exclusive reconstruction. These channels provide insights into the discrepancies observed in the missing mass squared distributions of candidates reconstructed from MC samples compared to experimental data section 7.2. In particular, the wrong sign control channel is employed to estimate the systematic effect caused by the non-alignment of the M^2_{miss} distribution of MC and data candidates.

7.5.1 Exclusive reconstruction

The outcome of partial reconstruction is sought to be better understood by omitting inclusively and fully reconstructing the signal decay of $\overline{B}^0 \to D^{*+}(\to D^0\pi^+)\ell^+\overline{\nu}$. Two highly frequent hadronic decay modes of the D^0, namely $D^0 \to K^- \pi^+$ and $D^0 \to K^- \pi^+ \pi^- \pi^+$, are selected.

The M^2_{miss} distributions for both decays are displayed in Figure 7.5, and the MC distributions are compared to data. Although not immediately obvious and lacking a definitive conclusion, it is noticeable that the residuals tend to be more negative for positive M^2_{miss} compared to values of M^2_{miss} below 0, in particular in the case of the $D^0 \to K^- \pi^+$ channel. This reflects the observation of the partial reconstruction as depicted in Figure 7.1.

7.5.2 Wrong-sign reconstruction

As delineated in section 5.2, the formation of signal B^0 candidates involves the combination of lepton and pion candidates. Conservation of charge necessitates opposite charges for the lepton and the pion. Therefore, when attempting to combine a lepton candidate with the same charge as the pion candidate, it is guaranteed that no correctly reconstructed signal B^0 candidate is found in the sample. Consequently, the wrong-sign channel exclusively comprises background candidates. A comparison between MC and data M^2_{miss} distribution is also conducted and displayed in Figure 7.6.

Considering the residuals depicted among the distributions of M^2_{miss}, a qualitatively similar behavior to the case of correct reconstruction can be observed, both before and after reweighting. Specifically, this behavior entails that before reweighting, the simulated data overestimate the experimental data for all ranges of M^2_{miss}.

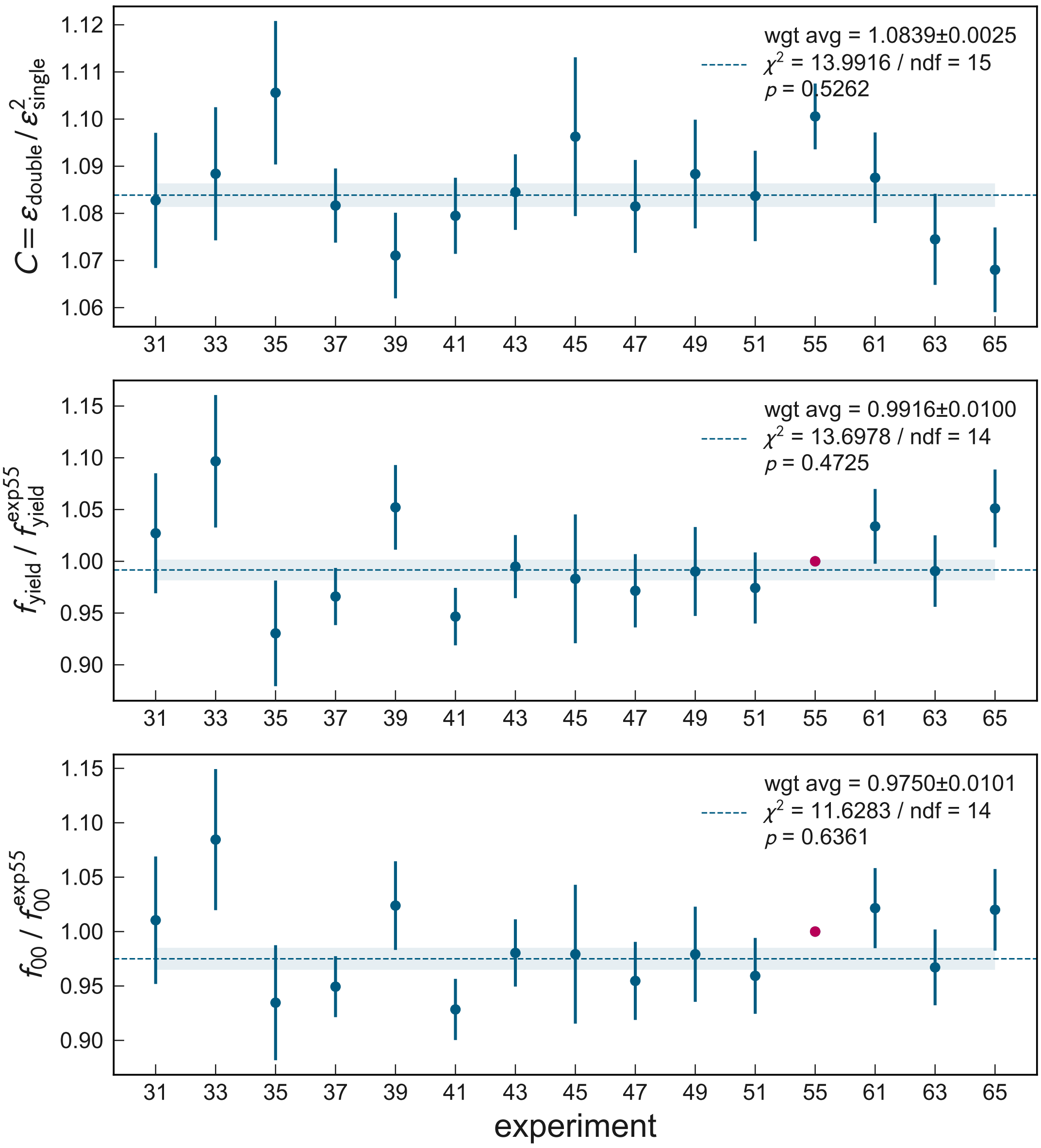

Figure 7.4: Decomposition of the experiment-dependent, normalized measurement of $f_{00} = \dfrac{1}{4N_{B\bar{B}}} \dfrac{N^2_{\text{single}}}{N_{\text{double}}} C_{\text{eff}}$. The efficiency ratio C_{eff} (upper plot). The central plot shows the fraction of yields $N^2_{\text{single}}/N_{\text{double}}$, while the lower plot displays the branching fraction f_{00}, both normalized with respect to the outcome of experiment 55 (identified by red markers). The statistical metrics (weighted average, χ^2) are defined in Equation 7.1 and Equation 7.2. The vertical blue bars represent the statistical uncertainties.

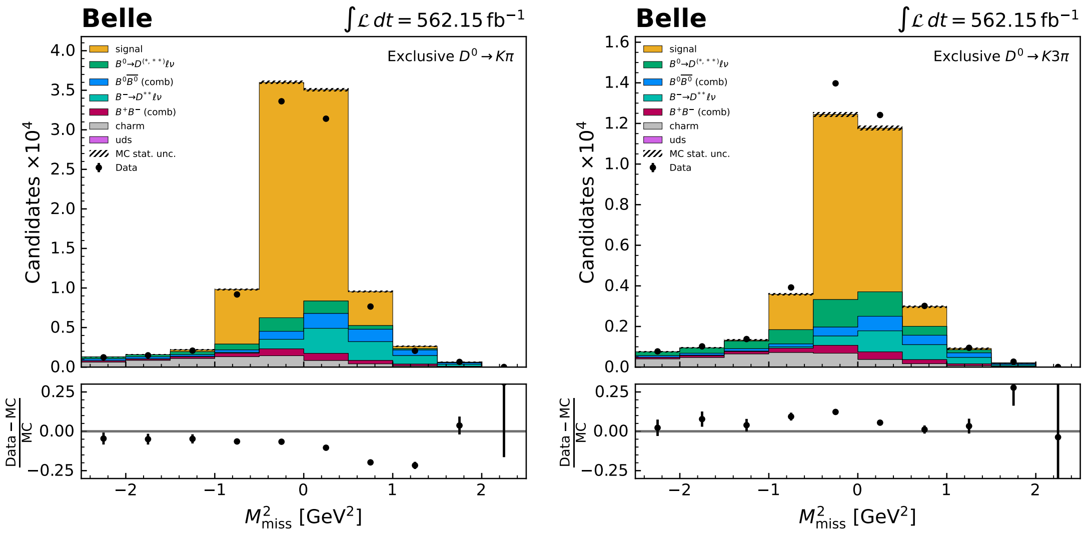

Figure 7.5: Comparison of M^2_{miss} distributions of exclusively reconstructed candidates from data and MC. The left plot depicts the exclusive channel of $D^0 \to K^-$ π^+ and the right plot of $D^0 \to K^-$ π^+ π^- π^+. Additionally, the relative residuals of data and MC for each bin is shown under each plot.

After reweighting, the data are underestimated by the MC, with a relatively constant trend for M^2_{miss} values up to -2 GeV^2. From approximately -1.5 GeV^2 onwards, the relative residuals decrease, only to rise again to the original values around 1 GeV^2. Thus, there is a small *dip* for positive values of M^2_{miss}. A comparable dip is clearly noticeable in the case of correctly reconstructed candidates.

Due to the similar behavior and the fact that in the case of the wrong-sign channel, no signal events contribute, the assumption can be made that the deviation of the simulation from the data arises solely from an inaccurate modeling of the background.

Based on this assumption, in subsection 8.1.5, a bin-dependent correction factor is determined from the wrong-sign distributions. These factors, when applied to the correct-sign candidates, allow for an adjustment of the MC distribution to match the real data.

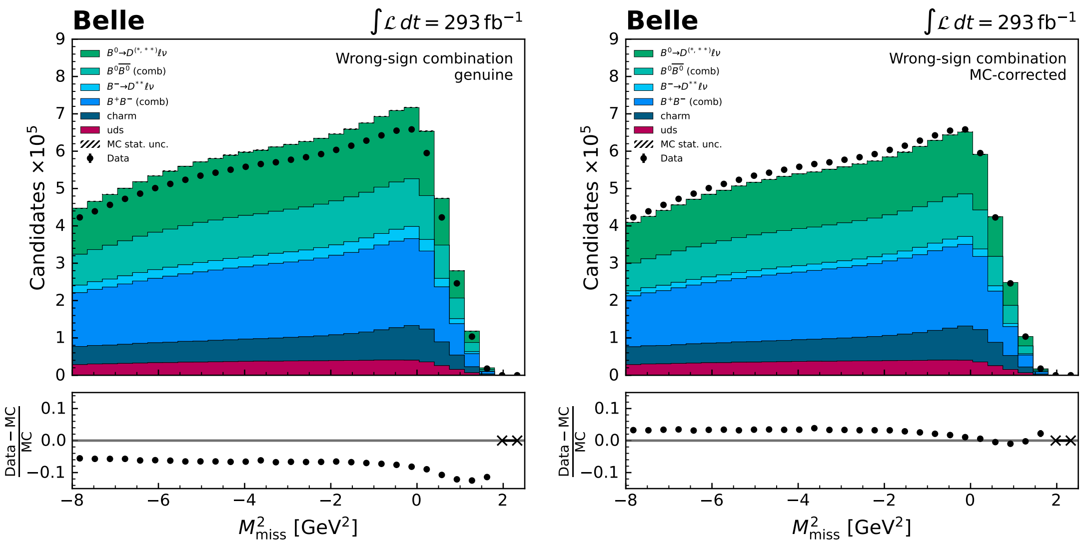

Figure 7.6: Comparison of M^2_{miss} distributions of wrong-sign candidates reconstructed from data and MC. Left: genuine MC (no weights applied). Right: corrected MC (reweighed). Additionally, the relative residuals of data and MC for each bin is shown under each plot.

Chapter 8

Systematic Uncertainties

8.1 Evaluation

This section covers the systematic uncertainties resulting from the modeling of the MC samples and the measured number of produced $B\overline{B}$ pairs in the experiment.

The first part of this section explains the derivation of up and down variations for the corrections with correlated uncertainties. These include the slow pion efficiency (see subsection 4.4.1), the lepton PID (see subsection 4.4.2) and parametrization of the form factors (see subsection 4.4.5). Further, it is explained how the number of B meson pairs produced was determined experimentally. Finally, the systematic uncertainty due to the disagreement of M^2_{miss} distributions of MC candidates and candidates reconstructed from data is elaborated.

The second part of the section summarizes the results of the systematic investigation. This includes the corrections mentioned in the first part. In addition, those corrections are considered that have uncorrelated variations from the beginning: the updating of branching fractions (see subsection 4.4.4) and the event scaling (see subsection 4.4.3).

The calculation of systematic uncertainties proceeds by calculating f_{00} using all nominal values of the MC correction factors. The determination of f_{00} involves the calculation of C_{eff} and the fitting of the M^2_{miss} distribution to determine the single-tag and double-tag signal yield. The whole procedure to determine f_{00} is then repeated for each systematic variation. In cases where systematic uncertainties are correlated, it is necessary to transform these uncertainties into uncorrelated up and down variations before proceeding.

8.1.1 Slow pion efficiency

The corrections applied to account for different efficiencies in data and MC for the reconstruction of slow pions is explained in subsection 4.4.1. The correction factors listed in Table 4.2 are equipped with uncorrelated and correlated statistical uncertainties and an additional systematic uncertainty. The statistical uncertainty among different kinematic bins is independent, while the systematic uncertainties are assumed to be fully correlated.

A principal component analysis is performed to calculate up and down variations while accounting for the correlations. Initially, the covariance matrix C_π is defined in terms of the six momentum bins.

This matrix is the sum of the covariance matrices of the uncorrelated and correlated statistical uncertainties, $C^{\text{uncorr}}_{\text{stat}}$ and $C^{\text{corr}}_{\text{stat}}$ respectively, and the correlated systematic uncertainties $C^{\text{corr}}_{\text{syst}}$

$$C_\pi = C^{\text{uncorr}}_{\text{stat}} + C^{\text{corr}}_{\text{stat}} + C^{\text{corr}}_{\text{syst}}. \tag{8.1}$$

The statistical covariance matrix is free of correlations and therefore diagonal and defined as

$$C^{\text{uncorr}}_{\text{stat}} = \begin{bmatrix} \left(\sigma^{\text{uncorr}}_{\text{stat}}(1)\right)^2 & \dots & 0 \\ \vdots & \ddots & \\ 0 & & \left(\sigma^{\text{uncorr}}_{\text{stat}}(6)\right)^2, \end{bmatrix} \tag{8.2}$$

where $\sigma^{\text{uncorr}}_{\text{stat}}(i)$ is the uncorrelated statistical uncertainty for the ith momentum bin.

Due to the correlations of the other uncertainties, the two latter matrices have off-diagonal elements. With an assumed correlation of 100%, these matrices are defined as

$$C^{\text{corr}}_{\text{stat,syst}} = \begin{bmatrix} \sigma^{\text{corr}}_{\text{stat,syst}}(1) \cdot \sigma^{\text{corr}}_{\text{stat,syst}}(1) & \dots & \sigma^{\text{corr}}_{\text{stat,syst}}(1) \cdot \sigma^{\text{corr}}_{\text{stat,syst}}(6) \\ \vdots & \ddots & \\ \sigma^{\text{corr}}_{\text{stat,syst}}(6) \cdot \sigma^{\text{corr}}_{\text{stat,syst}}(1) & & \sigma^{\text{corr}}_{\text{stat,syst}}(6) \cdot \sigma^{\text{corr}}_{\text{stat,syst}}(6), \end{bmatrix} \tag{8.3}$$

where $\sigma^{\text{corr}}_{\text{stat,syst}}(i)$ is either the correlated statistical or systematic uncertainty for the ith momentum bin.

Subsequently, the eigenvalues of C_π are determined and organized as a vector denoted as $\vec{\lambda}$. The matrix P is constructed by arranging the eigenvectors of C_π as its columns. This relation is expressed by

$$\vec{\lambda} = P^{-1} \cdot C_\pi \cdot P, \tag{8.4}$$

corresponding to the eigendecomposition of the covariance matrix C_π. If one rotates the vector of weights ρ_π into the space spanned by the matrix of eigenvectors P,

$$\hat{\rho}_\pi = \rho_\pi \cdot P^{-1}, \tag{8.5}$$

the covariance of $\hat{\rho}_\pi$ is diagonal and therefore uncorrelated and hence up and down variations can be computed by adding and subtracting the variances from the rotated nominal correction weights. The variances are the square of eigenvalues λ_k.

$$\tilde{\rho}_{\pi,\pm k} = \hat{\rho}_\pi \pm \sqrt{\lambda_k}. \tag{8.6}$$

Finally, the up and down variations in the rotated space are transformed back, which yields the correction factor variations Δ_{ρ_π}

$$\Delta_{\rho_\pi,\pm k} = \tilde{\rho}_{\pi,\pm k} \cdot P. \tag{8.7}$$

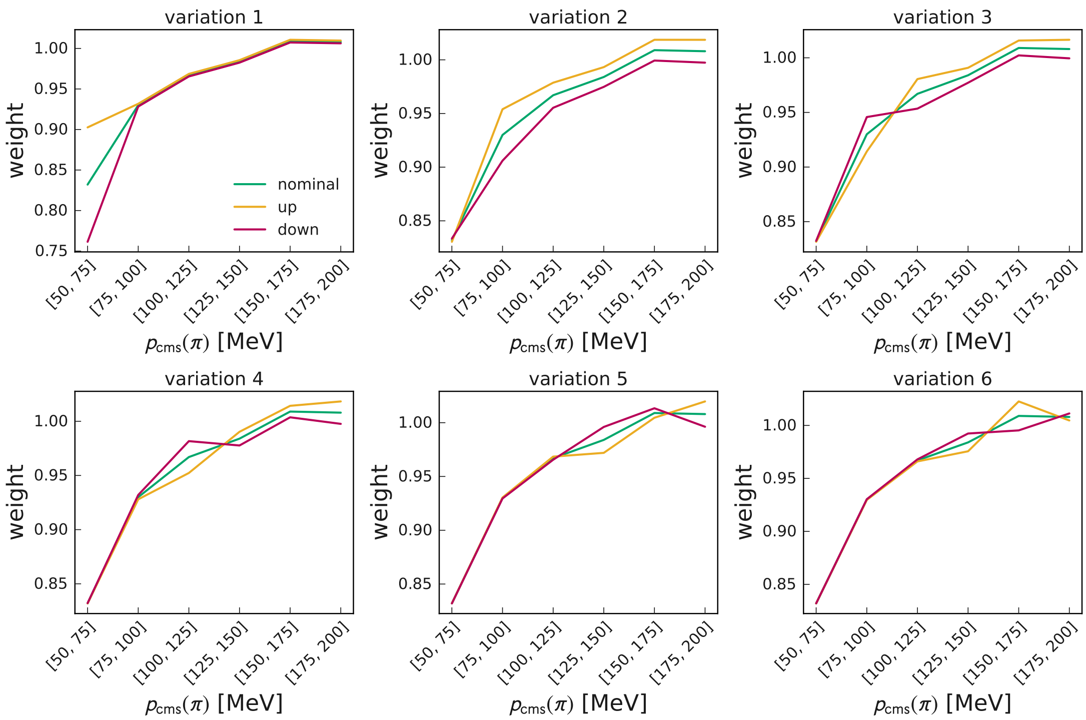

Figure 8.1: The 2 × 6 sets of correction factor variations (weights) of the pion reconstruction efficiency reweighting in terms of the 6 momentum bins. The nominal correction weight is represented by the green line, the up and down variations by the yellow and red lines respectively.

This results in 2×6 sets of correction factor variations, displayed in Figure 8.1

8.1.2 Lepton identification efficiency

The corrections applied to consider the deviating lepton identification efficiency is introduced in subsection 4.4.2. The correction factors determined in [65] are equipped with uncorrelated and correlated uncertainties, the fake rate corrections from [66] only with correlated uncertainties. Both types of uncertainties are used to obtain variations of the correction factors. For this purpose, 250 variations of the nominal correction factors are generated for the statistical and systematic uncertainties, respectively.

In general, the variational weight $w_{\text{variation}}$ is calculated using the nominal weight w_{nominal}, the corresponding uncertainty σ_{w} and a random number $\mathcal{G}_{\text{rand}}(0,1)$, sampled from the standard normal distribution:

$$w_{\text{variation}} = w_{\text{nominal}} + \mathcal{G}_{\text{rand}}(0,1) \cdot \sigma_{\text{w}} \tag{8.8}$$

There are two different types of variations, accounting for the uncorrelated and the correlated uncertainties. In the case of the uncorrelated error, the random number $\mathcal{G}_{\text{rand}}(0,1)$ is generated independently for each kinematic bin. Conversely, for variations sampled from the correlated uncertainties, a singular random number is shared across all kinematic bins. Subsequent iterations of sampling require the generation of new random numbers.

8.1.3 Form factor models

As explained in subsection 4.4.5, there are two different models being updated, with different approaches.

Model update 1: $B \to D\ell\nu_\ell$ and $B \to D^*\ell\nu_\ell$

The input values that parametrize the form factor model are varied in order to estimate the systematic uncertainty of the chosen model. Since these parameters are correlated with each other, they need to be decoupled. For the decays $B \to D\ell\nu$ and $B \to D^*\ell\nu$, the statistical and systematic uncertainties are written as column vectors $\vec{\sigma}_{\text{stat}}$ and $\vec{\sigma}_{\text{syst}}$. With the corresponding correlation matrices C_{stat} and C_{syst}, the total correlation matrix C_{FF} is defined as

$$C_{\text{FF}} = \vec{\sigma}_{\text{stat}}\vec{\sigma}_{\text{stat}}^{\intercal} \odot C_{\text{stat}} + \vec{\sigma}_{\text{syst}}\vec{\sigma}_{\text{syst}}^{\intercal} \odot C_{\text{syst}}, \tag{8.9}$$

with $A \odot B$ is the element-wise product of the matrices A and B and $\vec{\sigma}^{\intercal}$ denoting the transpose of $\vec{\sigma}$. Therefore, $\vec{\sigma}\vec{\sigma}^{\intercal}$ is the outer product of the column vectors.

Similar to the principal component analysis described in subsection 4.4.2, this results in pairs of five pairs up and down variations for $B \to D\ell\nu_\ell$ and six pairs for $B \to D^*\ell\nu_\ell$. The distribution of the weights and its variations are found in Figure 8.2 and Figure 8.3 respectively. The statistical and systematic correlation matrices are found in section A.3, where the values for $B \to D\ell\nu_\ell$ are listed in Table A.3 and for $B \to D^*\ell\nu_\ell$ in Table A.1 and Table A.2.

Model update 2 : $B \to D^{**}\ell\nu$

The systematic uncertainties due to the form factor remodeling for decays of the type $B \to D^{**}\ell\nu$ are evaluated differently. As mentioned, the reweighting procedure is not based on an analytical method, but on newly generated MC samples that are produced with both the old ISGW2 and the new LLSW parametrization. Therefore, separate MC samples are generated for each of the variation of every input parameter. The resulting variations of correction factors are shown exemplarily for $B \to D_1\ell\nu$ in Figure 8.4. The results of the remaining decays involving a D^{**} are found in section A.3 in Figure A.7, Figure A.8 and Figure A.9.

8.1.4 Number of B-events

The decisive Belle note that published the measurement of the number of $N_{B\bar{B}}$ by S.Swain and T.Browder (Internal Belle Note 659 *"Measurement of N(BBar) and BBar cross-section at Belle"*) is no longer available. This meant that the measurement results of the individual experiments, including the breakdown of the uncertainties, could only be found in a Perl script on the KEK website that lists the experiment-depending total numbers [88].

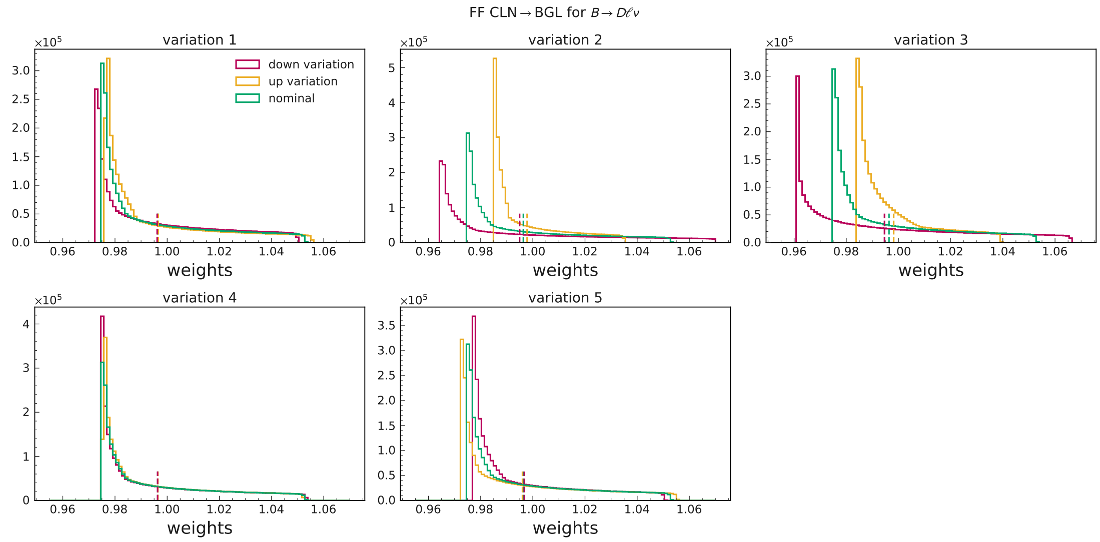

Figure 8.2: Distribution of nominal correction factors and the five pairs of up and down variations after reconstruction for the $B \to D\ell\nu_\ell$ form factor remodeling from CLN to BGL parametrization. Due to cuts being applied in the reconstruction, the normalization is not necessarily conserved here.

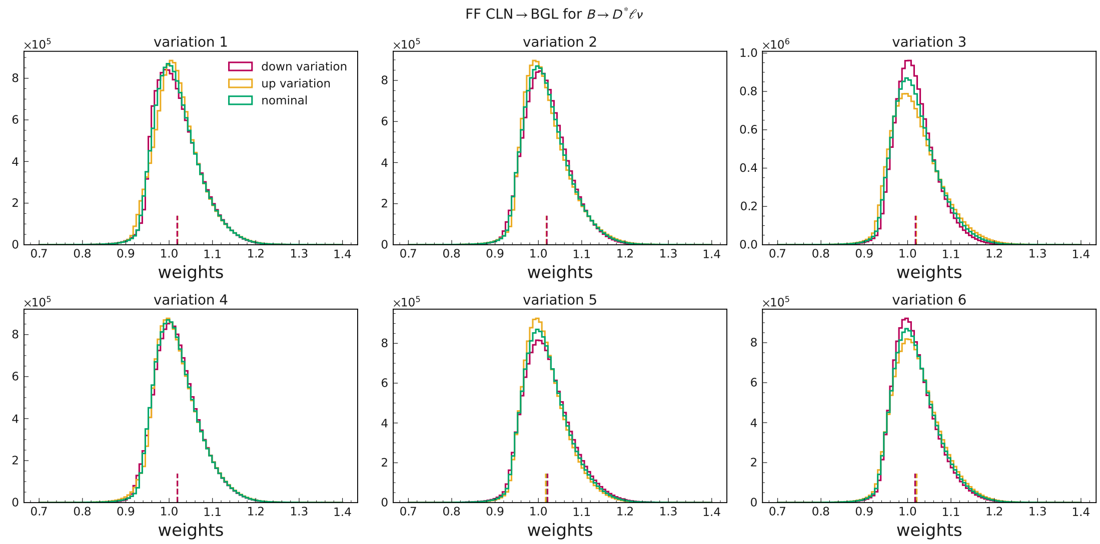

Figure 8.3: Distribution of nominal correction factors and the six pairs of up and down variations after reconstruction for the $B \to D^{*}\ell\nu_\ell$ form factor remodeling from CLN to BGL parametrization. Due to cuts being applied in the reconstruction, the normalization is not necessarily conserved here.

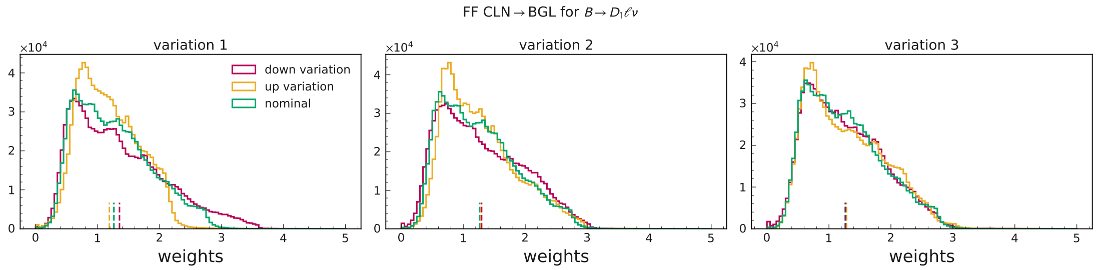

Figure 8.4: Distribution of nominal correction factors and the 3 pairs of up and down variations for the $B \to D_1\ \ell\nu$ ISGW2 to LLSW form factor remodeling. Due to cuts being applied in the reconstruction, the normalization is not necessarily conserved here. The weight distribution of the remaining D^{**} decays are found in section A.3.

Several sources exist that describe the idea behind the measurement of $B\overline{B}$ pairs [89, 90], partly providing different information. Therefore, the two papers mentioned, are cited in the following.

The hadronic sample acquired by the Belle detector is the combination of the $B\overline{B}$ sample with $e^+e^- \to \Upsilon(4S) \to B\overline{B}$ decays and the continuum events with $e^+e^- \to q\overline{q}$, where q are the quarks lighter than the b-quark . Therefore, the total number of produced on-resonance events is

$$N^{\text{on}} = N^{\text{on}}_{B\bar{B}} + N^{\text{on}}_{q\bar{q}}. \tag{8.10}$$

To determine the number of $B\overline{B}$ pairs, Belle has taken an off-resonance sample. With this, the ratio

$$\alpha = \frac{N^{\text{on}}_{q\bar{q}}}{N^{\text{off}}_{q\bar{q}}} = \frac{\mathcal{L}^{\text{on}}}{\mathcal{L}^{\text{off}}} \cdot \frac{s^{\text{off}}}{s^{\text{on}}} \tag{8.11}$$

can be formulated, where $\mathcal{L}$ denotes the integrated luminosity and $E_{\text{cms}} = \sqrt{s}$ the center-of-mass energy.

Inserting α into Equation 8.10 and solving for $N^{\text{on}}_{B\bar{B}} = N_{B\bar{B}}$ yields

$$\begin{aligned} N_{B\bar{B}} &= N^{\text{on}} - N^{\text{on}}_{q\bar{q}} \\ &= N^{\text{on}} - \alpha \cdot N^{\text{off}}_{q\bar{q}}. \end{aligned} \tag{8.12}$$

Assuming that, apart from cross sections, fermion production is independent of the center-of-mass energy, the ratio of the number of continuum events produced for on-resonance and off-resonance energy can be expressed as

$$\alpha = \frac{N^{\text{on}}_{q\bar{q}}}{N^{\text{off}}_{q\bar{q}}} = \frac{N^{\text{on}}_{e^+e^-}}{N^{\text{off}}_{e^+e^-}} = \frac{N^{\text{on}}_{\mu^+\mu^-}}{N^{\text{off}}_{\mu^+\mu^-}}, \tag{8.13}$$

where $N_{e^+e^-}$ is the number of Bhabha events and $N_{\mu^+\mu^-}$ the number of dimuon events. For the experiments that are used in this analysis (31−65), the measurement of the number of dimuon events is not considered reliable, hence only the Bhabha events are taken into account when determining α.

Equation 8.12 is not efficiency-corrected yet. Defining $c = \frac{\epsilon_{\text{on}}}{\epsilon_{\text{off}}}$ as the ratio of efficiencies for $q\overline{q}$ events for on-resonance and off-resonance, the final equation to extract the number of $B\overline{B}$ events from the hadronic sample reads

$$N_{B\overline{B}} = N^{\text{on}} - c \cdot \alpha \cdot N^{\text{off}}_{q\overline{q}}. \tag{8.14}$$

The statistical uncertainty is calculated by combining the on-resonance, off-resonance, and the statistical uncertainty for α:

$$\sigma_{\text{stat}} = \sqrt{N^{\text{on}} + (\alpha c)^2 N^{\text{off}} + (cN^{\text{off}})^2 \sigma^2_{\alpha}}, \tag{8.15}$$

and for the systematic uncertainty, an additional uncertainty is considered: the time dependence of the beam gas fraction, denoted by δ_{BGF}. This results in

$$\sigma_{\text{syst}} = \sqrt{\delta^2_{\text{BGF}} + (cN^{\text{off}})^2 \sigma^2_{\alpha^\cdot} + (\alpha N^{\text{off}})^2 \sigma^2_{c}}. \tag{8.16}$$

Depending on the beam gas fraction, asymmetric up and down uncertainties are calculated. For the measurement of f_{00}, the uncertainties are symmetrized by choosing the larger variation.

The statistical, systematic and total uncertainties for $N_{B\overline{B}}$ for the total data sample is

$$N_{B\overline{B}} = \left(619.6198 \pm 0.5316_{\text{stat}} \pm 9.4548_{\text{syst}}\right) \times 10^6 \tag{8.17}$$
$$= \left(619.6198 \pm 9.4697_{\text{total}}\right) \times 10^6 \tag{8.18}$$

as well as for the individual experiments are listed in section A.4.

8.1.5 Data-MC disagreement

As described in section 7.2 and observed in Figure 7.1, the M^2_{miss} distribution of the signal candidates is not particularly well described by MC. A similar behavior of non-aligning M^2_{miss} distribution was found in the side-channels, as described in subsection 7.5.1 and subsection 7.5.2. Based on the relative residuals of the wrong-sign channel, bin-dependent weight factors are determined in the comparison of data and MC in Figure 7.6.

The bin-wise correction factors $w_{\text{D−MC}}$ considering the data−MC disagreement are calculated as

$$w_{\text{D−MC}}\,(i) = \frac{N_{\text{data, i}} - N_{\text{MC, i}}}{N_{\text{MC, i}}} \times 1.05, \tag{8.19}$$

where $N_{\text{data, i}}$ and $N_{\text{MC, i}}$ denote the number of candidates in each bin i, reconstructed from data and MC, respectively. These relative residuals are increased by 5%, whereby this value was determined visually, so that the best match of the M^2_{miss} distributions is obtained.

Applying these corrections to the background fit components of the correct-sign candidates results in a better alignment of M^2_{miss} distributions for MC and data.

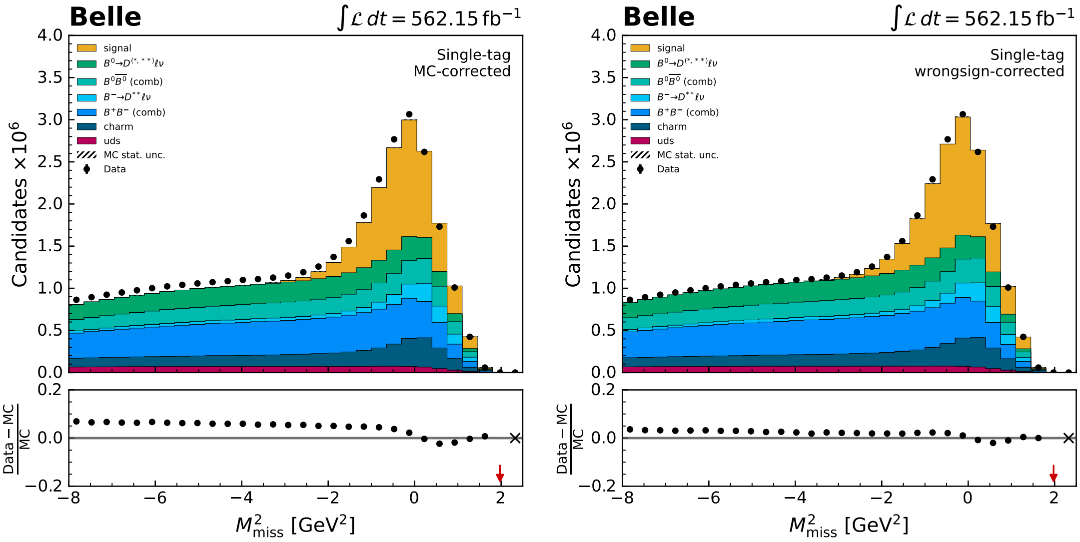

Figure 8.5: Data − MC comparison of M^2_{miss} distribution. Left: nominal corrected MC. Right: MC that has additionally been corrected with the weights calculated in Equation 8.19.

The weights determined in this section are solely intended for the purpose of determining the systematic uncertainty. To emphasize this, the terms nominally corrected MC and wrong-sign corrected MC are employed. In Figure 8.5, the outcome (wrong-sign corrected MC, right plot), in comparison with the candidates that have just been reweighed to the corrections explained in section 4.4 (nominal corrected MC, left plot) are presented.

As the shape of the PDF distribution is modified, the impact of the correction is confined to the shape of the fit templates. Consequently, this systematic uncertainty is designated as *PDF shape*. To estimate this uncertainty, the procedure to determine f_{00} is repeated with the fit templates generated from the wrong-sign corrected MC M^2_{miss} distributions. The absolute distance to the nominal value of f_{00} is prescribed as the systematic uncertainty due to the shape of the background PDF.

8.2 Summary of uncertainties

This section outlines the derivation of systematic uncertainties from the various types of sources mentioned in section 8.1. The results of the evaluation of systematic uncertainties for the measurement of f_{00} are listed in Table 8.1 and presented in Figure 8.6.

The systematic uncertainty due to the measured number of B meson pairs is determined by linearly propagating the uncertainty of $N_{B\bar{B}}$ as given in Equation 8.1.4. Equivalently, the systematic uncertainty is determined by the inaccuracy of the efficiencies due to the finite MC sample and hence the uncertainty on C_{eff}.

Correcting the MC samples for outdated physical parameters or differences between simulation and data impacts the reconstruction efficiencies as well as the shape of kinematic distributions and therefore the fit shapes. For this, it is necessary to consider the influence of the corrections on C_{eff} and the signal yields as systematic uncertainties for the measurement of f_{00}.

To ascertain these uncertainties while maintaining adherence to the criteria for a blinded analysis, all outcomes of f_{00} are randomized by an undisclosed, randomly generated value n^{R} prior to analysis.

The calculation of systematic uncertainties due to MC corrections starts with the determination of f_{00}, where all correction factors are set to their nominal values:

$$f_{00}^{\text{nom, R}} = 0.4004, \tag{8.20}$$

where the superscript *nom* indicates for nominal value and *R* for the randomization.

Then, similarly, for each variation k and for each type of MC correction, f_{00} is calculated with the up and down variation factors and randomized with the same random number n^{R}. The outcome is denoted as $f_{00}^{\text{type, R}}(k, \text{up})$ and $f_{00}^{\text{type, R}}(k, \text{down})$, respectively. The types of corrections comprise the list of

- slow pion efficiency with 6 variations,
- form factor parametrization:
  - with 5 variations for $B \to D\ell\nu_\ell$,
  - with 6 variations for $B \to D^*\ell\nu_\ell$,
  - with 3 variations for $B \to D_1\ell\nu_\ell$ and $B \to D_2^*\ell\nu_\ell$,
  - with 2 variations for $B \to D_1'\ell\nu_\ell$ and $B \to D_0^*\ell\nu_\ell$,
- branching fractions with single variation, and
- event scaling with single variation,
- lepton PID with 2×250 sampled variations (no up and down variation).

The difference from the nominal value is then calculated. Finally, the larger absolute difference is selected as the systematic uncertainty associated with this type of MC correction:

$$\sigma_{\text{syst}}^{\text{type}}(k) = max\Big(\left|f_{00}^{\text{nom, rand}} - f_{00}^{\text{type, rand}}(k, \text{up})\right|, \left|f_{00}^{\text{nom, rand}} - f_{00}^{\text{type, rand}}(k, \text{down})\right| \Big). \tag{8.21}$$

This procedure is repeated for each variation and for each type of MC corrections. The individual variations k of a type of MC correction, that is, the individual systematic uncertainties can be summed in quadrature.

$$\sigma_{\text{syst}}^{\text{type}} = \sqrt{\sum_{\text{k}} \left(\sigma_{\text{syst}}^{\text{type}}(k)\right)^2}. \tag{8.22}$$

The same holds for the distinct systematic uncertainties as well as for the statistical uncertainty. Therefore, the total measurement uncertainty derives from the quadratic sum of the statistical uncertainty and the systematic uncertainty:

$$\sigma_{\text{syst}} = \sqrt{\sum_{\text{type}} \left(\sigma_{\text{syst}}^{\text{type}}\right)^2}, \tag{8.23}$$

$$\sigma_{\text{total}} = \sqrt{\left(\sigma_{\text{stat}}\right)^2 + \left(\sigma_{\text{syst}}\right)^2}. \tag{8.24}$$

The result of the blinded measurement of f_{00} is determined to

$$f_{00}^{R} = 0.4004 \ \pm \ 0.0038_{\text{stat}} \left(\text{rel. } 0.94\%\right) \ \pm \ 0.0111_{\text{syst}} \left(\text{rel. } 2.76\%\right) \tag{8.25}$$

$$= 0.4004 \ \pm \ 0.0117_{\text{total}} \left(\text{rel. } 2.92\%\right). \tag{8.26}$$

Although the result is randomized, the comparative evaluation of the relative uncertainties allows an assessment of the magnitude of the uncertainty with respect to the *BaBar* measurement[2]:

$$f_{00}^{BaBar} = 0.486 \ \pm \ 0.010_{\text{stat}} \left(\text{rel. } 2.06\%\right) \ \pm \ 0.008_{\text{syst}} \left(\text{rel. } 1.65\%\right) \tag{8.27}$$

$$= 0.486 \ \pm \ 0.0128_{\text{total}} \left(\text{rel. } 2.64\%\right). \tag{8.28}$$

Assuming that the data set on which the *BaBar* measurement is based ($\mathcal{L} = 71.8\,\text{fb}^{-1}$), and the data set used in this analysis ($\mathcal{L} = 571.15\,\text{fb}^{-1}$) have a similar composition, a relative statistical error of 0.78% can be expected given the almost 7-fold size of the Belle data set. The slightly larger statistical uncertainty of 0.95% can be attributed to a larger proportion of background events. To quantify this, the figure of merit (*FOM*) is evaluated for single-tag candidates, which is derived from the counts of signal and background candidates:

$$\text{FOM} = \frac{N_{\text{signal}}}{\sqrt{N_{\text{signal}} + N_{\text{background}}}}, \tag{8.29}$$

This metric is computed for the *BaBar* analysis, yielding $\text{FOM}^{BaBar} = 611$, and compared with the corresponding value for this analysis, $\text{FOM} = 1184$. Consequently, the *BaBar* detector is able to select a sample with a higher signal purity than the *Belle* detector. As a result, a slightly increased statistical uncertainty is observed, which differs from what would be expected from a comparison of data set sizes alone.

The systematic uncertainty is also greater in comparison with the *BaBar* measurement result. This is ascribed to the correlation between single and double candidate reconstruction that was only observed in the case of this measurement. This obviously leads to fewer systematic uncertainties which are being cancelled out by taking the ratio when determining f_{00}.

type of uncertainty	abs. uncertainty	rel. uncertainty [%]
statistical	0.0038	0.94
systematic	0.0111	2.76
– $N(B\overline{B})$	0.0062	1.54
– PDF shape	0.0048	1.20
– C_{eff}	0.0009	0.23
– branching fractions	0.0062	1.55
– event scaling	0.0002	0.05
– form factor models	0.0037	0.93
– slow pion efficiency	0.0025	0.63
– lepton PID	0.0012	0.29
total	0.0117	2.92

Table 8.1: The absolute uncertainties with respect to $f_{00}^{\text{nom, R}} = 0.4004$ and the relative uncertainties given as percentages for the various sources of measurement uncertainty. The last row presents the total uncertainties, calculated as the square root of the sum of the squares of the individual uncertainties.

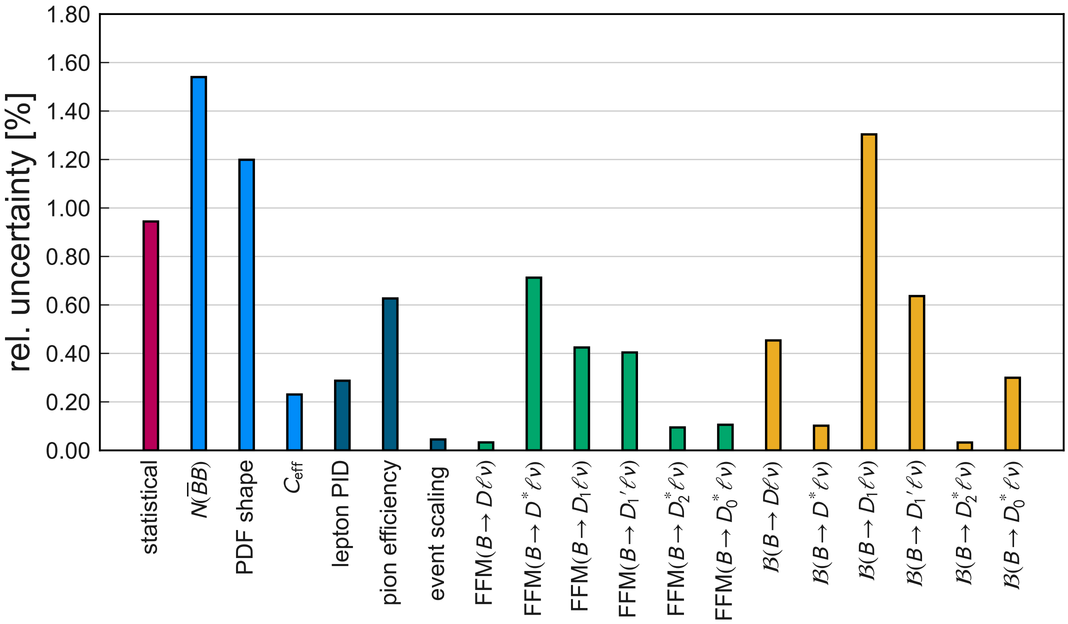

Figure 8.6: This plot illustrates all relative uncertainties determined for the global measurement of f_{00}, presented as percentages. The red bar is the statistical uncertainty, all other bars show various uncertainties from systematic sources: the number of measured $N(B\overline{B})$, the uncertainty due to the shapes of the PDFs and the error on the efficiency ratio C_{eff} (light blue), the lepton PID, pion reconstruction efficiency and the uncertainty due to event scaling (dark blue), the updating of form factor models for $B \to X_c\ell\nu_\ell$ decays (green), and the updating of branching fractions for $B \to X_c\ell\nu_\ell$ decays (yellow). The values are listed in Table 8.1

Chapter 9

Preliminary Results

Despite the analysis being conducted with the utmost care, the results are still to be regarded as preliminary. This is because, at the time of writing this thesis, the *Belle II* collaboration had not yet conducted an official review process. The analysis was summarized in a detailed transcript, a Belle Note, and submitted to the corresponding committee of the *Belle II* collaboration prior the box opening. Additionally, the main aspects of the analysis and the blinded results were presented to this committee. After thoroughly reviewing the *Belle* Note, the committee expressed the intention to release the results in a *Belle II* publication.

This chapter defines the two measurement approaches, presents the measurement results after box-opening, discusses the conclusions and shortcomings of the result, gives a summary of the analysis and provides an outlook on further development in this matter.

9.1 The two measurement approaches

The analysis encompasses two distinct approaches: the global measurement of f_{00} and the experiment-dependent measurement. The global measurement is the main result while the experiment-based measurement serves as validation.

The global measurement involves analyzing all data collected by the *Belle* detector at the $\Upsilon(4S)$ resonance using the SVD2 configuration. In this approach, the data sample is treated as a single continuous dataset, and the resulting parameter is labeled as f_{00}^{global}.

In the process of developing the simulation-level analysis, the variance of reconstruction efficiencies across experiments has raised concerns regarding the viability of the anticipated global measurement. While the validity study described in section 7.4 indicates that this variance likely stems from a combination of detector and reconstruction algorithms rather than the method itself, f_{00} is still independently determined for each experiment. The resulting value of this approach is obtained by calculating the weighted average of the experiment-based outcomes, with the weights determined by the inverse square of the statistical fit uncertainties

$$w = \frac{1}{\sigma_{\text{stat, fit}}(\text{exp})}. \tag{9.1}$$

The experimented-based validation measurement is labeled as $f_{00}^{\text{exp-based}}$.

9.2 Box-opening

This analysis is performed as a blind analysis. Initially, all methods are developed using simulated data. The entire analysis process is subsequently applied to experimental data. However, the final result, specifically the value of f_{00}, is strictly not examined. Instead, the individual results in the experiment-based validity measurement are normalized by the result from reference experiment 55, and in the global measurement, the result is randomized using a randomly generated number.

Box-opening refers to unblinding the analysis by eliminating the randomization in the calculation of the global f_{00} measurement and omitting normalizing the experiment-dependent $f_{00}^{\text{normed}}(\text{exp})$.

The systematic uncertainties listed in Table 8.1 are determined on the global measurement of f_{00} and are thus precisely only valid for f_{00}^{global}. Yet, in order to compare the two results, the relative systematic uncertainty for the global measurement is prescribed as the systematic uncertainty for the experiment-based measurement as well.

The preliminary outcome of the global measurement is

$$f_{00}^{\text{global}} = 0.477 \pm 0.005_{\text{stat}}(\text{rel. } 0.94\%) \pm 0.013_{\text{syst}}(\text{rel. } 2.75\%)\,. \tag{9.2}$$

The statistical and systematic uncertainties are presented separately. Their absolute values are indicated by the respective superscript label, with the relative uncertainties provided in parentheses.

The validating result of the experiment-based measurement is

$$f_{00}^{\text{exp}-\text{based}} = 0.478 \pm 0.013_{\text{total}}(\text{rel. } 2.76\%)\,. \tag{9.3}$$

Only the total uncertainty is provided here because the systematic uncertainty for the experiment-based result was not rigorously determined, but was rather simply carried over from the global measurement. The total uncertainty is calculated as the square root of the sum of the squares of the statistical and systematic uncertainties.

Table 9.1 lists the signal yields for single-tag and double-tag decays for the global sample and the individual experiments.

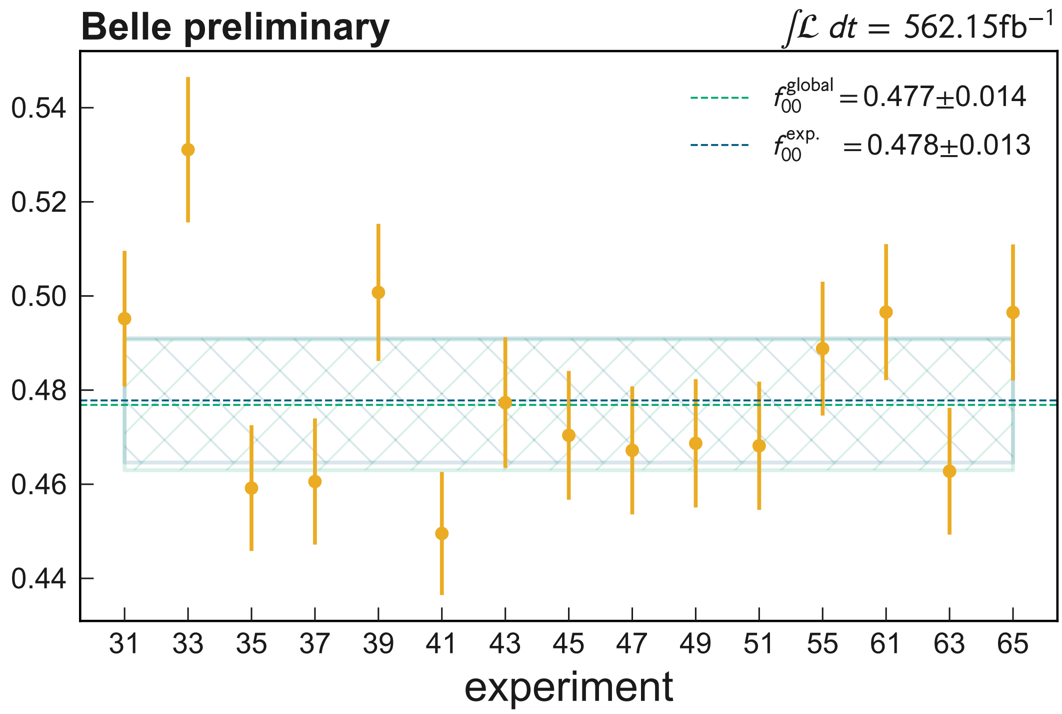

Figure 9.1: The preliminary results after box-opening of the f_{00} analysis. The result of the global measurement f_{00}^{global} is represented by the green line, with its total uncertainty shown by the green hatched area. The weighted average, serving as validation, of the experiment-based outcomes $f_{00}^{\text{exp-based}}$ is illustrated in blue, with the uncertainty indicated by the area with perpendicular hatches. The outcomes of the measurement of f_{00} for the individual experiments are shown in yellow, with their uncertainties indicated by the yellow bars. The results, the global measurement and the validation outcome, are in excellent agreement.

Sample	Single-tag yield	Double-tag yield
global	$(7.159 \pm 0.008) \times 10^6$	$(4.71 \pm 0.04) \times 10^4$
experiment 31	$(2.184 \pm 0.014) \times 10^5$	$(1.33 \pm 0.07) \times 10^3$
experiment 33	$(2.215 \pm 0.014) \times 10^5$	$(1.30 \pm 0.07) \times 10^3$
experiment 35	$(1.996 \pm 0.014) \times 10^5$	$(1.29 \pm 0.07) \times 10^3$
experiment 37	$(7.565 \pm 0.027) \times 10^5$	$(5.00 \pm 0.14) \times 10^3$
experiment 39	$(5.179 \pm 0.022) \times 10^5$	$(3.05 \pm 0.12) \times 10^3$
experiment 41	$(7.102 \pm 0.026) \times 10^5$	$(4.73 \pm 0.13) \times 10^3$
experiment 43	$(6.961 \pm 0.026) \times 10^5$	$(4.47 \pm 0.13) \times 10^3$
experiment 45	$(1.587 \pm 0.013) \times 10^5$	$(1.02 \pm 0.06) \times 10^3$
experiment 47	$(4.635 \pm 0.022) \times 10^5$	$(3.02 \pm 0.11) \times 10^3$
experiment 49	$(3.380 \pm 0.018) \times 10^5$	$(2.23 \pm 0.09) \times 10^3$
experiment 51	$(4.966 \pm 0.022) \times 10^5$	$(3.41 \pm 0.12) \times 10^3$
experiment 55	$(9.200 \pm 0.030) \times 10^5$	$(5.94 \pm 0.16) \times 10^3$
experiment 61	$(4.865 \pm 0.022) \times 10^5$	$(3.46 \pm 0.12) \times 10^3$
experiment 63	$(4.560 \pm 0.021) \times 10^5$	$(3.39 \pm 0.11) \times 10^3$
experiment 65	$(5.183 \pm 0.022) \times 10^5$	$(3.46 \pm 0.12) \times 10^3$

Table 9.1: Single-tag and double-tag signal yields for the entire (global) data sample and for each individual experiment.

9.3 Discussion

The outcome of the global measurement f_{00}^{global}, given in Equation 9.2, is in excellent agreement with the validity measurement result in Equation 9.3. The comparison of both approaches is illustrated in Figure 9.1, where the numerical values of f_{00}^{global} and $f_{00}^{\text{exp-based}}$ are shown alongside the individual f_{00} measurements for each experiment. Considering the uncertainties, the spread of the experiment-based result is in line with the expectation.

The degree of confidence in the measurement and its result is further increased by benchmarking the outcomes with the published value of the *BaBar* measurement. The result of this analysis is excellent agreement with the outcome of the *BaBar* analysis. The comparison is depicted in Figure 9.2.

9.4 Shortcomings of the analysis

Some aspects of the analysis require further investigation as they could not be fully resolved within the scope of the thesis. This section discusses the main ones and offers suggestions for further improvement.

9.4.1 Validation of MC corrections

The corrections of the generic Belle MC samples explained in section 4.4 have been subject to many revisions and continuous development throughout the work on

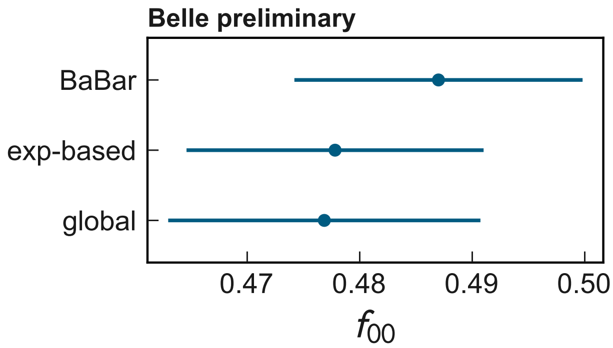

Figure 9.2: Benchmarking the two distinct measurement outcomes of f_{00} in this analysis with the published value of the *BaBar* measurement [2]. The global measurement result, validated through the experiment-based approach, aligns with the outcome of the *BaBar* analysis within the bounds of uncertainty.

the analysis. It is important to note that the influence of the correction factors on both the reconstruction efficiencies of single-tag and double-tag candidates as well as the distribution of the fit variables, and thus on the overall result of the measurement, is significant.

Challenging in this context is that no reliable method was available or could be constructed to credibly verify the correctness of the implementation of the weight factors. A comparison of suitable physical quantities with existing *Belle* analyses that use the same signal channel could resolve this issue.

9.4.2 MC-data disagreement

A substantial deficit in the analysis is the discrepancy between the M^2_{miss} distributions of reconstructed candidates from MC samples and experimental data, as shown in Figure 7.1. Despite the manifold corrections that the MC data set has undergone, a significant deviation remains, especially in the signal region with positive M^2_{miss} values. This mainly applies to single-tag candidates, for double-tag candidates the deviation is fairly constant and therefore not problematic. The effect of this deviation is absorbed with a systematic uncertainty, as described in subsection 8.1.5. The effect of this deviation is taken into account with a systematic uncertainty. At 1.2%, this is one of the three largest uncertainties for f_{00}.

In order to avoid this systematic uncertainty, it would have to be clarified what causes the deviations in the M^2_{miss} distribution. Therefore, the two kinematic variables that enter the calculation of M^2_{miss} are to be investigated: the momentum of the lepton and the momentum of the pion. The respective distributions are found in Figure 9.3, showing the comparison of the simulated and the reconstructed candidates from experimental data. Neither variable shows sufficient agreement between the distributions. In the pion momentum distribution, the disagreement is particularly large for momentum less than 80 MeV. The lepton momentum distributions align relatively good for low momentum but gets progressively worse with increasing momentum.

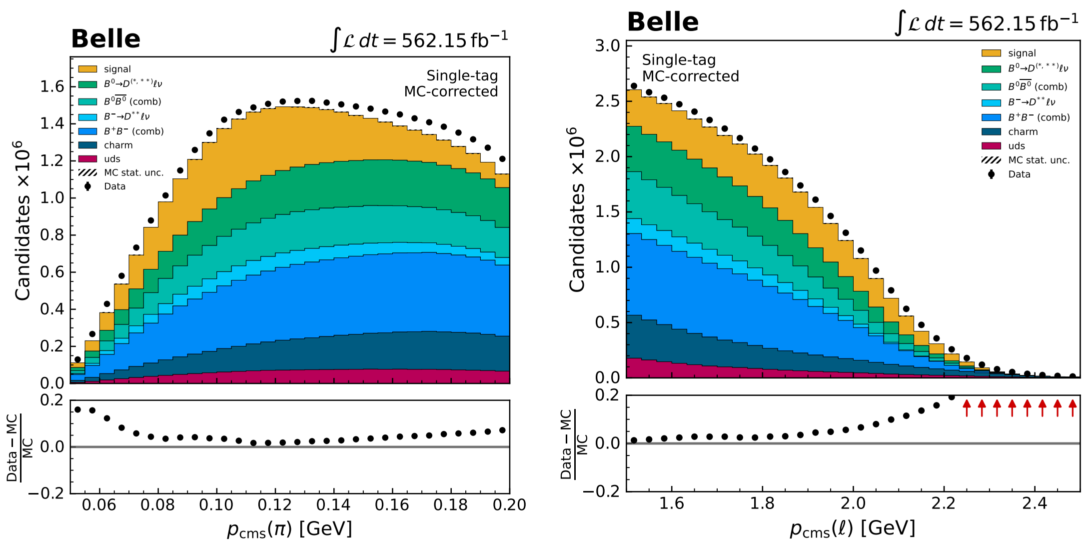

Figure 9.3: MC-data comparison of the two kinematic variables that are used to calculate fit variable M^2_{miss}: the pion momentum(left) and the lepton momentum (right).

It is also not possible to draw any direct conclusions about the deviations if only electrons or muons are selected for the reconstruction. The distribution of the lepton momentum for either the electron channel or muon channel is shown in Figure A.11. The pulls show the same qualitative behavior.

9.4.3 Wrong-sign correction factors

For this analysis, the wrong-sign channel is utilized to establish correction factors for the MC, aimed at evaluating the systematic uncertainties arising from data-MC discrepancies. This systematic uncertainty is referred to as *PDF shape*, as the mismodeling of the MC affects the shape of the fit templates.

In the past, there have been doubts about whether the wrong-sign combination sample serves as an appropriate control channel.In fact, it must be ensured that the correct-sign sample and the wrong-sign sample are composed of the same event types. By dividing the samples into appropriate event categories and comparing the components of the wrong-sign and correct-sign distributions, it becomes evident that the wrong-sign sample are fed from different event types. This is shown in Figure 9.4. It is therefore advisable to consider searching for a more suitable control channel.

9.4.4 Dependency of $R^{c/n}$ on the center-of-mass energy

Theoretical model calculations [19, 20, 21, 23, 22, 25] conclude that the production rate asymmetry of charged and uncharged B meson pairs in the decay of a resonantly generated $\Upsilon(4S)$ depends considerably on the centre-of-mass energy of the e^+e^- collision, as discussed in subsection 2.2.2. Hence, F. Bernlochner, M. Jung *et al.* suggest in [26] to determine $R^{c/n}$ at multiple center-of-mass energies in the vicinity

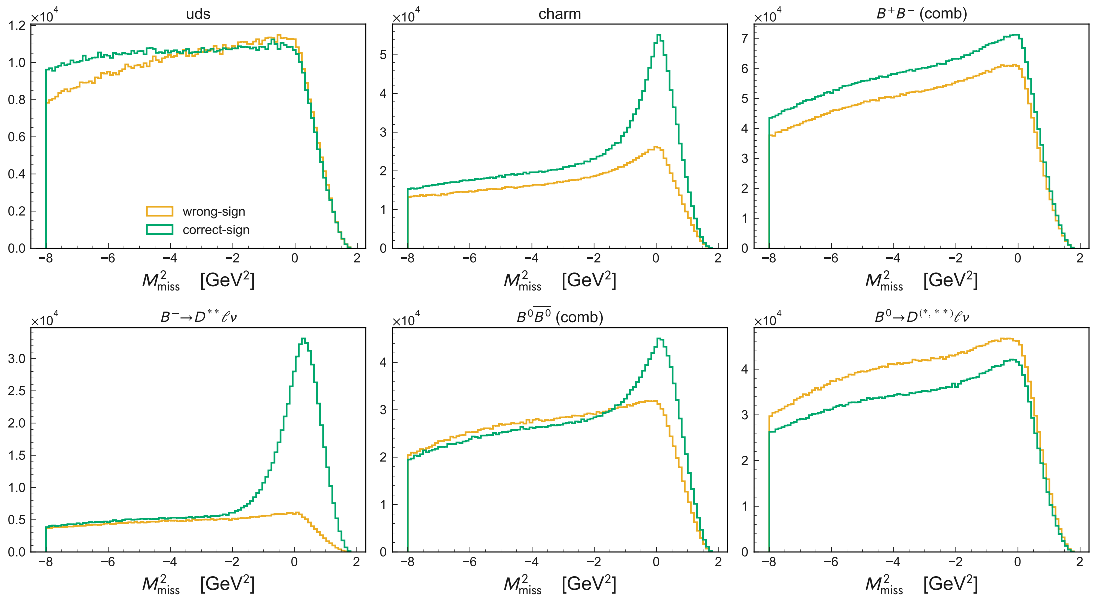

Figure 9.4: Comparing distributions of wrong-sign and correct-sign samples for various categories of events. Both the shape and the normalization do not match, in particular for the charm background and $B^- \to D^{**}\ell\nu$ decays.

of the $\Upsilon(4S)$ resonance.

A theoretical calculation of $R^{c/n}$ in dependency of center-of-mass energy is provided by the authors in Figure 9.5. Here, $R^{c/n}$ is plotted as a function of $\sqrt{s}$ for two different theory models. On request, an attempt was also made in the course of this analysis to prepare such a plot for f_{00} instead of $R^{c/n}$. In view of the time available, this could only be achieved to a limited extent. The missing information to calculate f_{00} as a function of $\sqrt{s}$ is an estimate of the number of produced $B\overline{B}$ pairs for specific center-of-mass energies. Therefore, the energy scan in Figure 9.6 only shows

$$\frac{N^2_{\text{single}}}{N_{\text{double}}} \cdot \frac{\epsilon_{\text{double}}}{\epsilon^2_{\text{single}}}, \tag{9.4}$$

the term involving $N_{B\overline{B}}$ is missing. A dependence on the center-of-mass energy is clearly visible, but there is no clear trend as predicted by Figure 9.5.

The upper plot in Figure 9.6 shows the distribution of the center-of-mass energy, which is not uniformly distributed. In order to be able to make statistically valid conclusions, a quantile-based binning is selected for the center-of-mass energy, providing data samples with equally sized portions. The lower plot represents Equation 9.4 as a function of $\sqrt{s}$ for each bin as defined in the upper plot. Only statistical uncertainties are incorporated in the calculation. Certainly, very different quantities are being compared here, which is why no general conclusion can be drawn. However, it is worth pursuing this further.

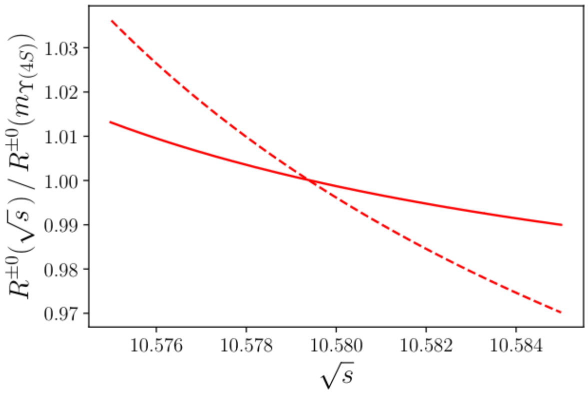

Figure 9.5: The ratio $R^{c/n}$ (here: $R^{+/0}$) as a function of $\sqrt{s}$ using two different theory model calculations, normalized to the respective values at $\sqrt{s} = 10.5794\,\mathrm{GeV}$ [26].

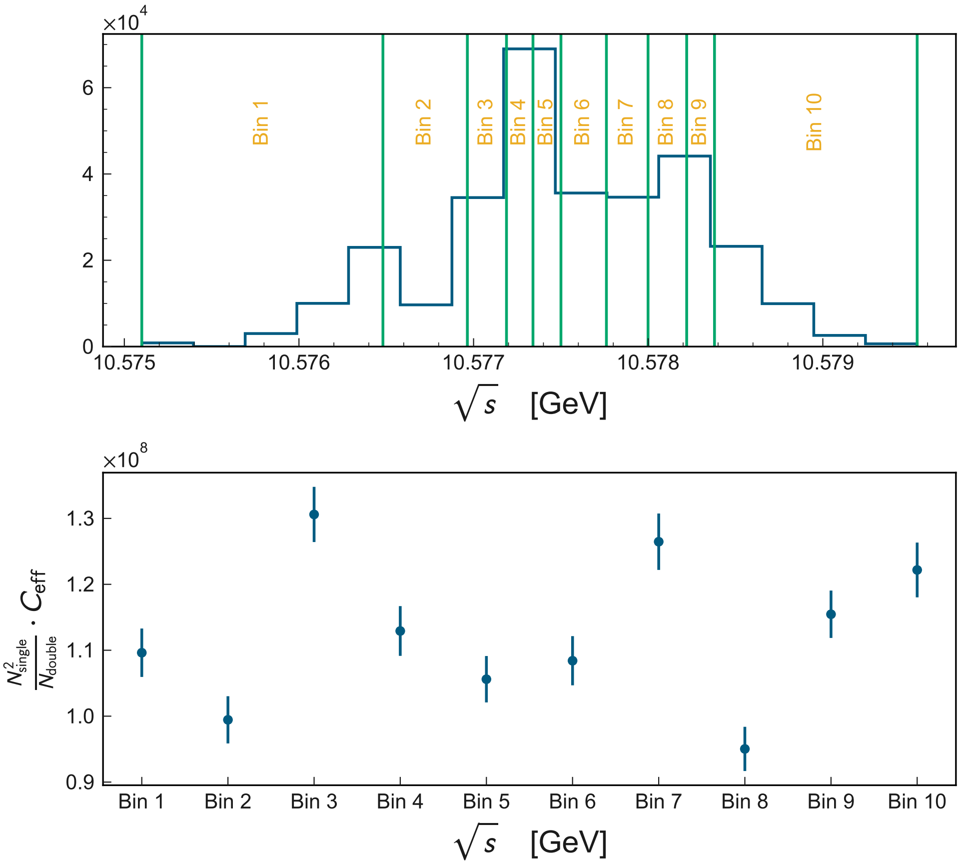

Figure 9.6: Upper: Distribution of center-of-mass in reconstructed events. Indicated by the green lines is the quantile-based binning used for the energy scan below. Lower: Center-of-mass energy scan of the product of fit yield ratio and efficiency ratio. The calculation of f_{00} is not feasible due to the missing information on the number of $B\overline{B}$ mesons in the respective binning.

Appendix A

A.1 Supplementary Material for the Tagging Method

There are three cases for reconstructing single-tag candidates. We define three different reconstruction efficiencies ϵ and the corresponding number of reconstructed candidates. We use the abbreviation $\mathcal{BR} = \mathcal{B}\big(B^0 \to D^{*-}(\to \overline{D}^0\pi^-)\ell^+\nu_\ell \big)$:

1. one true B^0 in the event, one B^0 is reconstructed correctly:

$$P\left(1 \text{ correctly rec } B^0 \mid 1 \text{ true } B^0\right) = \epsilon_{\text{single}}$$

   there are two possibilities: $B_1 \to \text{signal} + B_2 \to \text{generic}$ and vice versa, thus the factor of 2:

$$N_{\text{single}}\left(1 \text{ correctly rec } B^0 \mid 1 \text{ true } B^0\right) \;\sim\; 2 \cdot \mathcal{BR} \cdot \Big(1 - \mathcal{BR}\Big) \cdot \epsilon_{\text{single}}$$

2. two true B^0 in the event, one B^0 is reconstructed correctly:

$$P\left(1 \text{ correctly rec } B^0 \mid 2 \text{ true } B^0\right) = \epsilon_{\text{single}} \cdot (1 - \epsilon_{\text{single}})$$

   there are two possibilities: B_1 is correctly reconstructed while B_2 not and vice versa, thus the factor of 2:

$$N_{\text{single}}\left(1 \text{ correctly rec } B^0 \mid 2 \text{ true } B^0\right) \;\sim\; 2 \cdot \mathcal{BR}^2 \cdot \epsilon_{\text{single}} \cdot (1 - \epsilon_{\text{single}})$$

3. two true B^0 in the event, two B^0 are reconstructed correctly:

$$P\left(2 \text{ correctly reconstructed } B^0 \mid 2 \text{ true } B^0\right) = \epsilon_{\text{double}}$$

   there are two single-tag candidates in the event, thus the factor of 2:

$$N_{\text{single}}\left(2 \text{ correctly rec } B^0 \mid 2 \text{ true } B^0\right) \;\sim\; 2 \cdot \mathcal{B}\big(B^0 \to \text{signal} \big)^2 \cdot \epsilon_{\text{double}}$$

Combined this gives the expression for the number of reconstructed single-tag candidates

$$\begin{aligned} N_{\text{single}} &= N_{B\overline{B}}\; f_{00}\; \Big[2\;(1 - \mathcal{BR})\;\mathcal{BR}\;\epsilon_{\text{single}} + 2\;\mathcal{BR}^2\;\epsilon_{\text{single}}\;(1 - \epsilon_{\text{single}}) + 2\;\mathcal{BR}^2\;\epsilon_{\text{double}}\Big] \\ &= N_{B\overline{B}}\; f_{00}\; 2\;\Big[\mathcal{BR}\;\epsilon_{\text{single}} \;+\; \mathcal{BR}^2 \epsilon^2_{\text{single}}(C_{\text{eff}} - 1)\Big], \end{aligned}$$

with $C_{\text{eff}} = \epsilon_{\text{double}}/\epsilon_{\text{single}}^2$.

We can neglect the term $\mathcal{BR}^2\epsilon_{\text{single}}^2(C_{\text{eff}} - 1)$ and consider it as an error on N_{single} with $\Delta_{N_{\text{single}}}/N_{\text{single}} = 0.14\%$.

A.2 Supplementary Material for MC Correction: Form Factor Reweighting

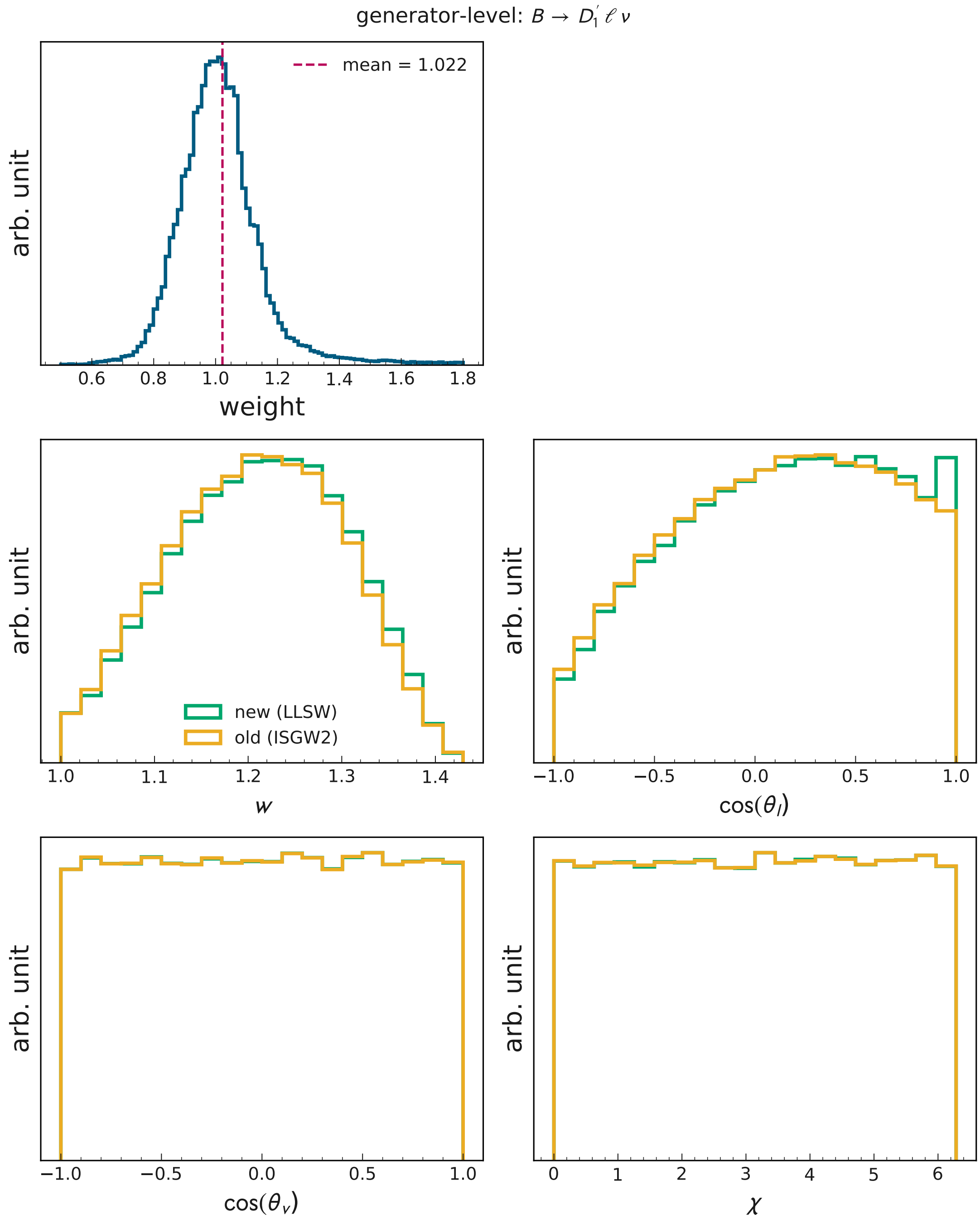

Figure A.1: Weight distribution and kinematic variable used to determine form factor model corrections for generator-level $B \to D_1' \ \ell\nu$ decays.

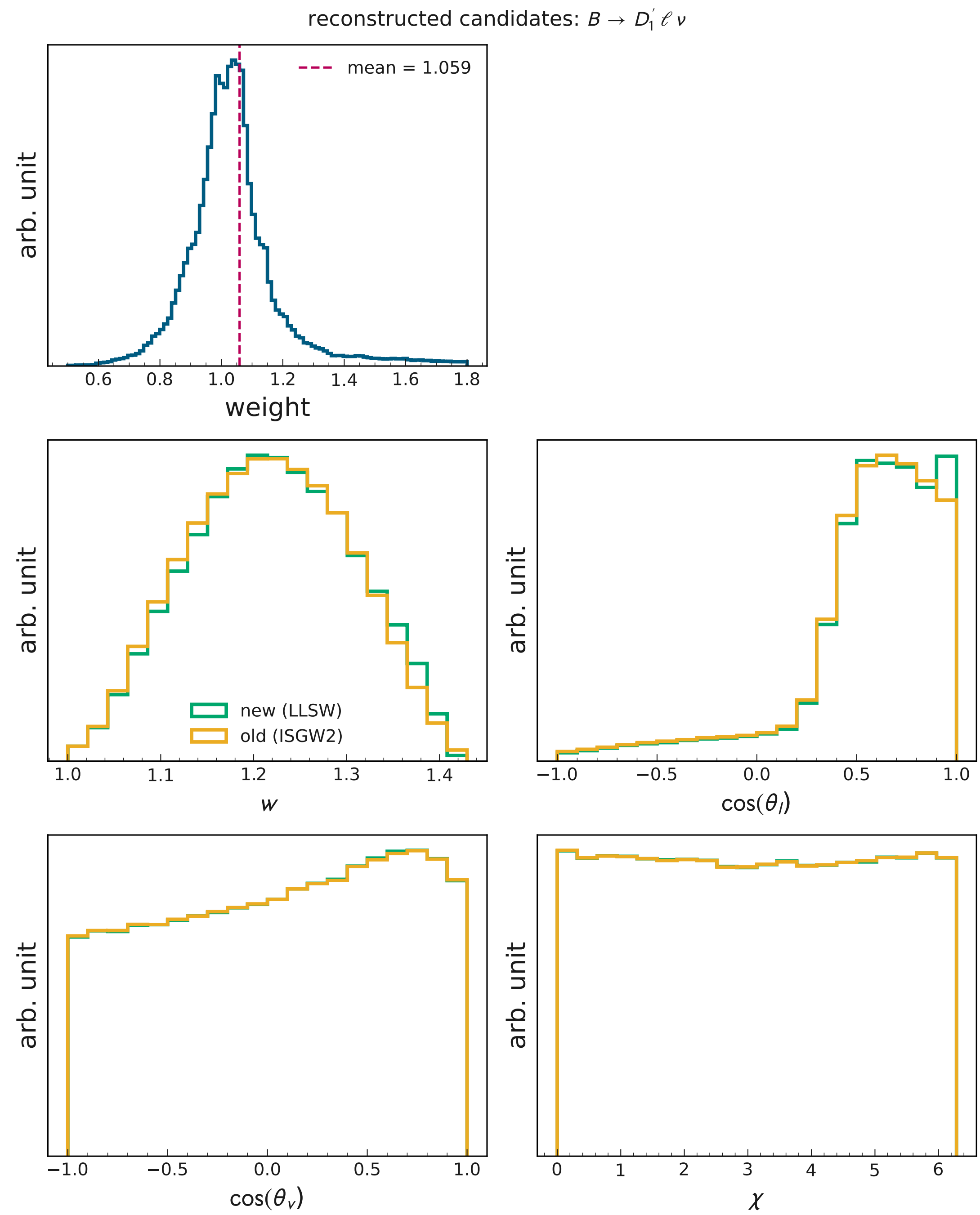

Figure A.2: Weight distribution and kinematic variable used to determine form factor model corrections for true reconstructed $B \to D_1' \ell\nu$ decays. Upper: Generator-level particles. Lower: Reconstructed candidates.

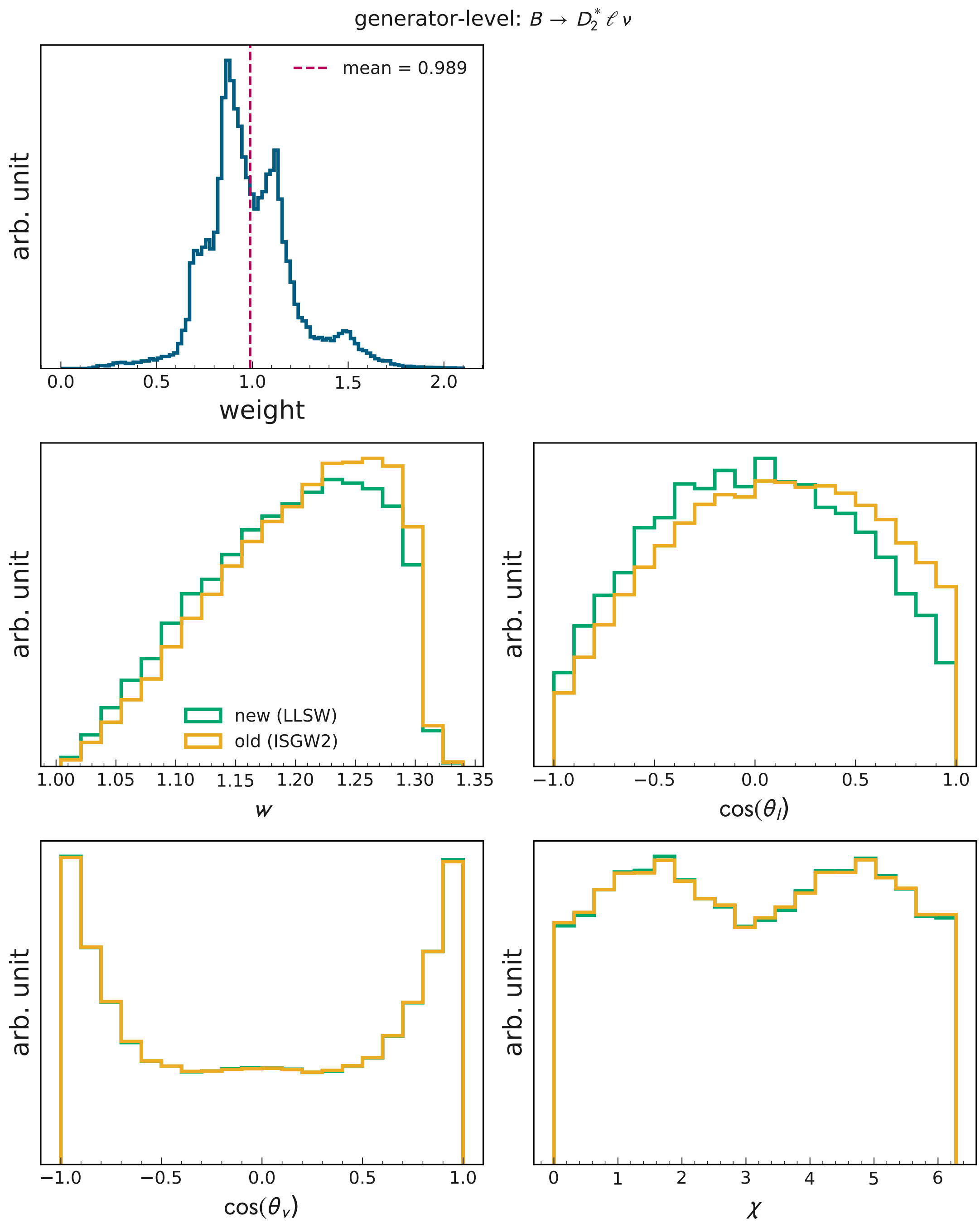

Figure A.3: Weight distribution and kinematic variable used to determine form factor model corrections for generator-level $B \to D_2^* \ \ell\nu$ decays.

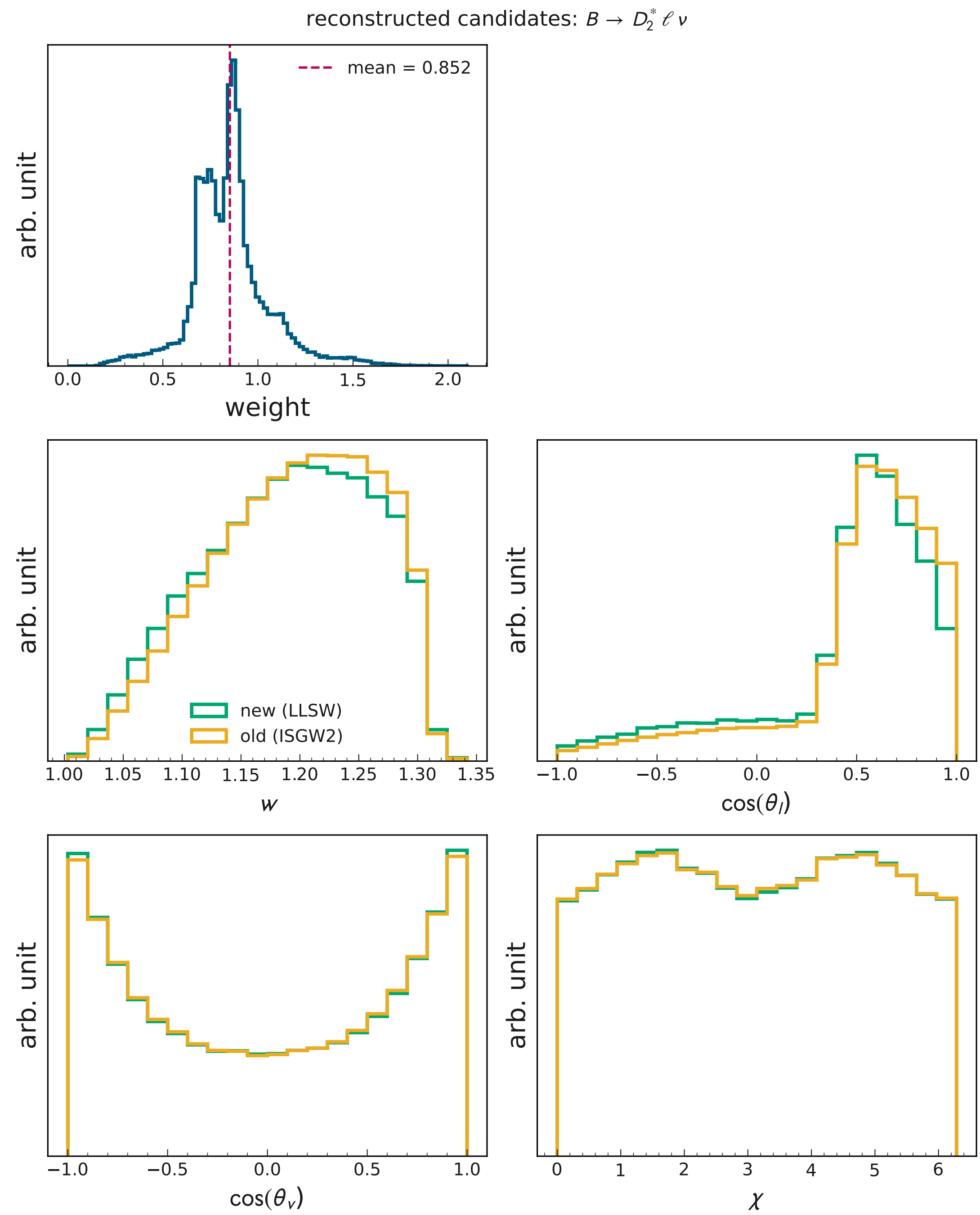

Figure A.4: Weight distribution and kinematic variable used to determine form factor model corrections for true reconstructed $B \to D_2^* \ell\nu$ decays. Upper: Generator-level particles. Lower: Reconstructed candidates.

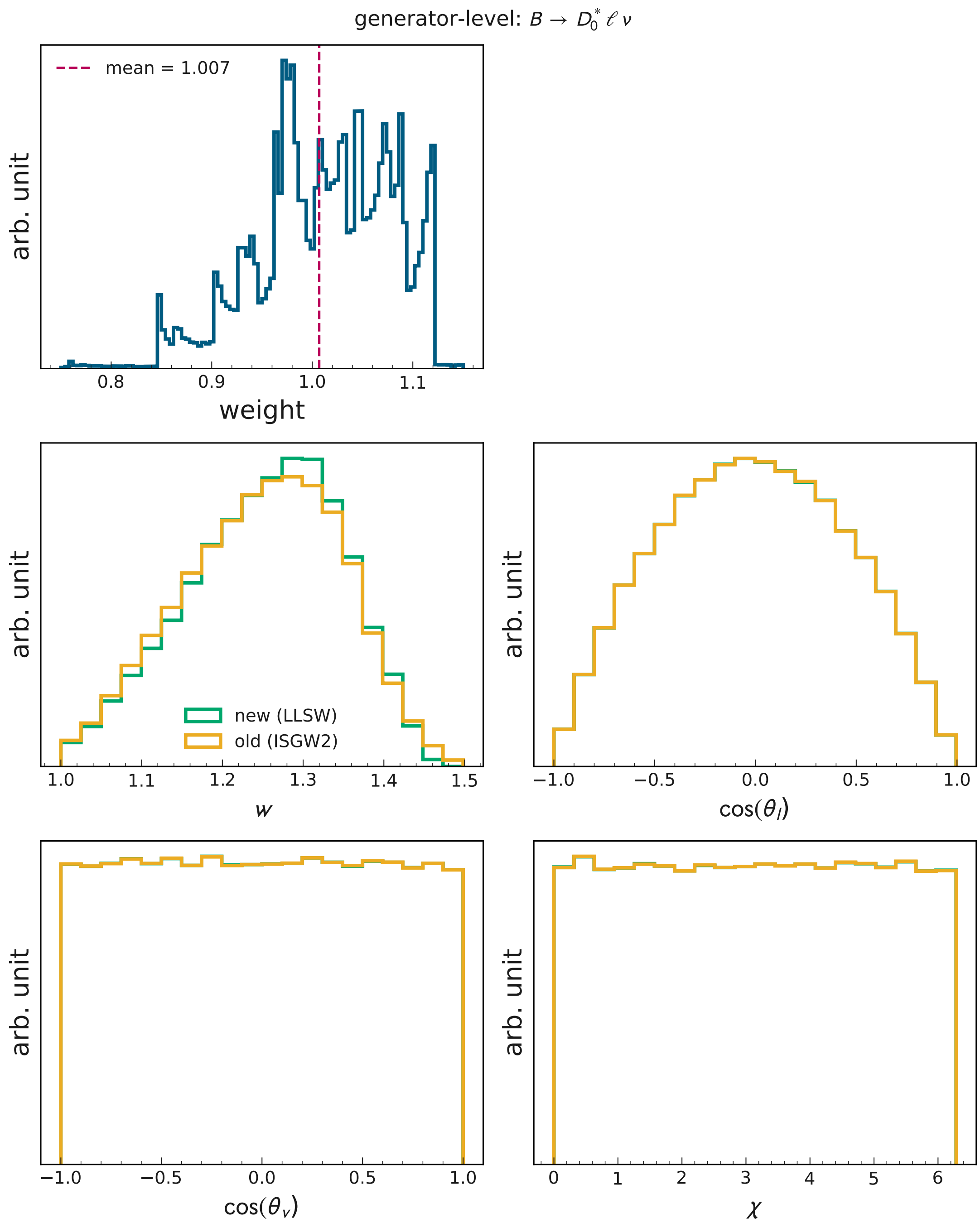

Figure A.5: Weight distribution and kinematic variable used to determine form factor model corrections for generator-level $B \to D_0^* \ell\nu$ decays.

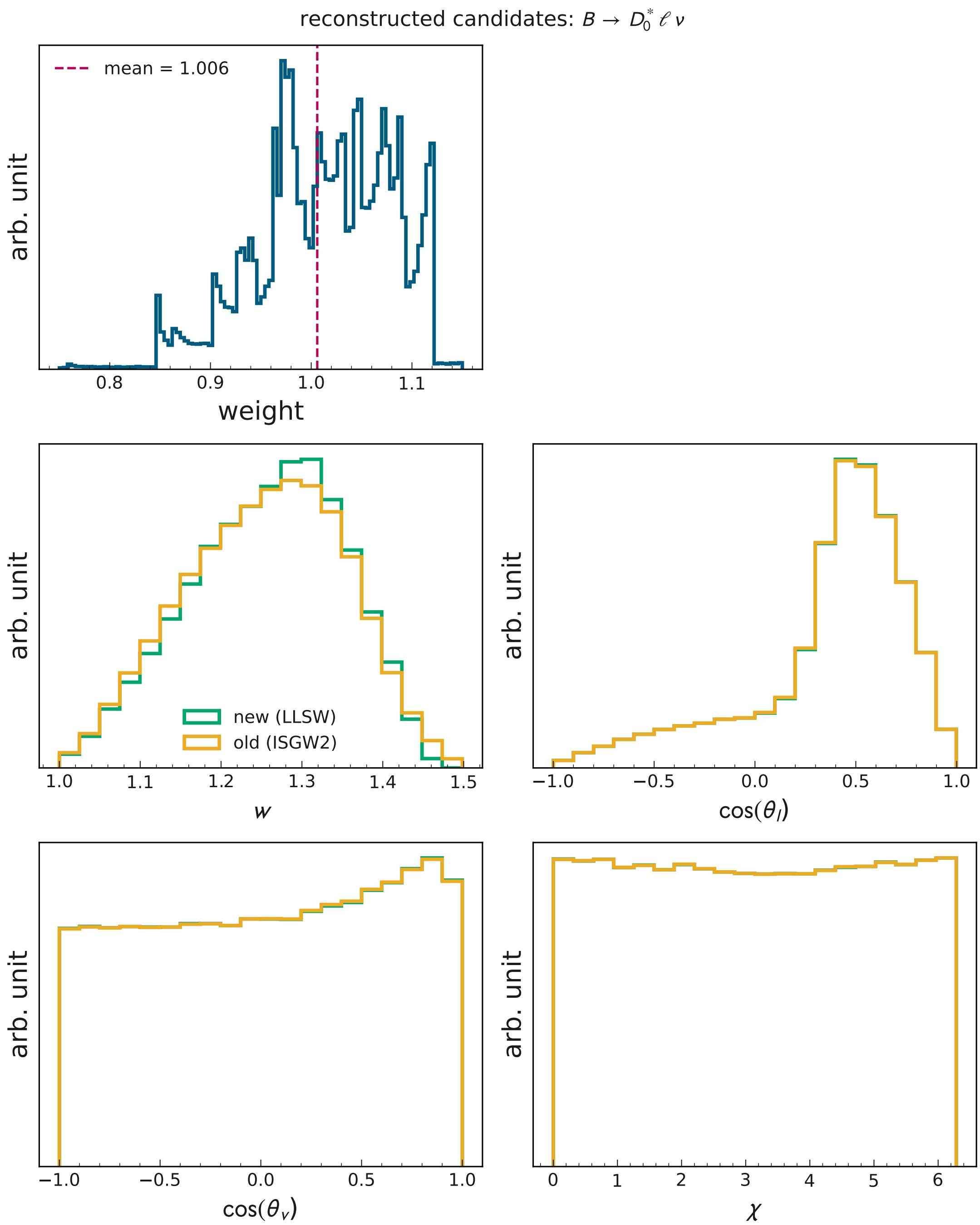

Figure A.6: Weight distribution and kinematic variable used to determine form factor model corrections for true reconstructed $B \to D_0^* \ell\nu$ decays. Upper: Generator-level particles. Lower: Reconstructed candidates.

A.3 Supplementary Material for the Form Factor Model Update

	Nom. $\times 10^3$	Stat. Correlation Matrix					
$\tilde{a}_0^g$	1.000	1.000	-0.940	-0.132	0.085	-0.077	0.158
$\tilde{a}_1^g$	-2.350	-0.940	1.000	0.129	-0.228	0.107	-0.189
$\tilde{a}_0^f$	0.511	-0.132	0.129	1.000	-0.806	-0.755	0.629
$\tilde{a}_1^f$	0.670	0.085	-0.228	-0.806	1.000	0.452	-0.362
$\tilde{a}_1^{\mathcal{F}_1}$	0.300	-0.077	0.107	-0.755	0.452	1.000	-0.977
$\tilde{a}_2^{\mathcal{F}_1}$	-3.680	0.158	-0.189	0.629	-0.362	-0.977	1.000

Table A.1: Statistical correlation matrix for the form factor remodeling from CLN to BGL parametrization for $B \to D^* \ \ell\nu$decays. The values used in this analysis are from a fit with BGL parametrization in the configuration (1,1,2) [78].

	Nom. $\times 10^3$	Syst. Correlation Matrix					
$\tilde{a}_0^g$	1.000	1.000	-0.937	-0.218	0.069	-0.081	0.161
$\tilde{a}_1^g$	-2.350	-0.937	1.000	0.127	-0.222	0.110	-0.192
$\tilde{a}_0^f$	0.511	-0.218	0.127	1.000	-0.800	-0.751	0.624
$\tilde{a}_1^f$	0.670	0.069	-0.222	-0.800	1.000	0.443	-0.354
$\tilde{a}_1^{\mathcal{F}_1}$	0.300	-0.081	0.110	-0.751	0.443	1.000	-0.978
$\tilde{a}_2^{\mathcal{F}_1}$	-3.680	0.161	-0.192	0.624	-0.354	-0.978	1.000

Table A.2: Systematic correlation matrix for the form factor remodeling from CLN to BGL parametrization for $B \to D^* \ \ell\nu$decays. The values used in this analysis are from a fit with BGL parametrization in the configuration (1,1,2) [78].

	Nom. $\times 10^3$	Stat. Correlation Matrix				
V_{cb}	41.11837	1.000	-0.402	-0.238	-0.110	0.047
$f_+(0)$	12.6147	-0.402	1.000	0.245	-0.161	0.020
$f_+(1)$	-96.2084	-0.238	0.245	1.000	-0.654	0.272
$f_+(2)$	413.884	-0.110	-0.161	-0.654	1.000	-0.770
$f_+(3)$	-173.699	0.047	0.020	0.272	-0.770	1.000

Table A.3: Correlation matrix for the form factor remodeling from CLN to BGL parametrization for $B \to D\ell\nu$ decays. The values used in this analysis are from a private fit to the data presented in [91].

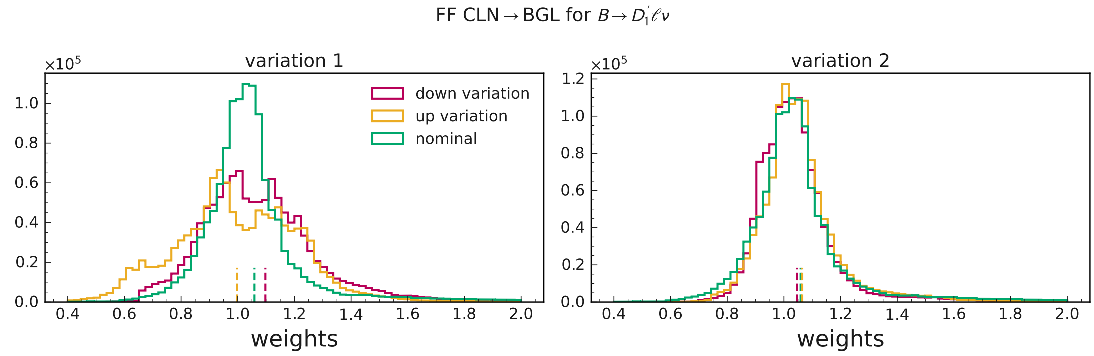

Figure A.7: Distribution of nominal correction factors and the 3 pairs of up and down variations for the $B \to D_1'\ell\nu$ ISGW2 to LLSW form factor remodeling.

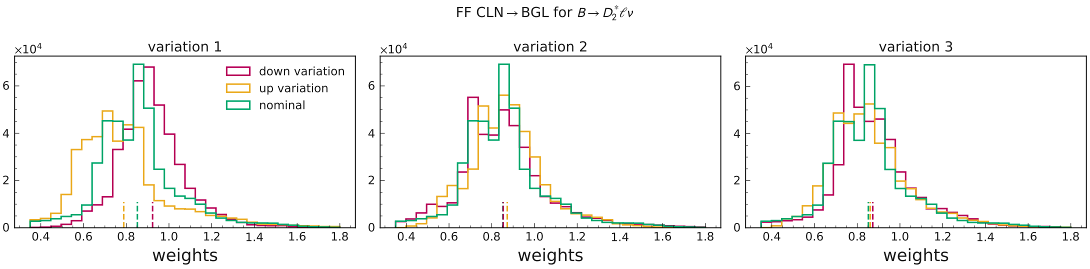

Figure A.8: Distribution of nominal correction factors and the 3 pairs of up and down variations for the $B \to D_2^*\ell\nu$ ISGW2 to LLSW form factor remodeling.

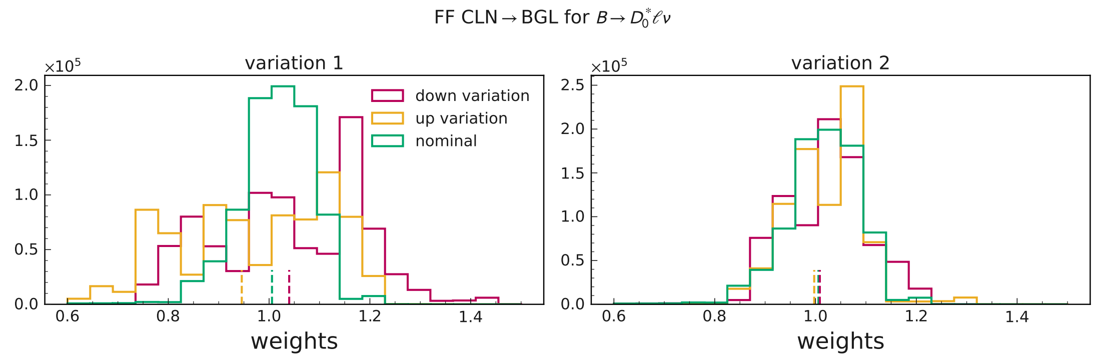

Figure A.9: Distribution of nominal correction factors and the 3 pairs of up and down variations for the $B \to D_0^*\ell\nu$ ISGW2 to LLSW form factor remodeling.

A.4 Supplementary Material for Systematic Uncertainties: Number of produced B meson pairs

exp.	$(N_{B\bar{B}} \pm \text{stat} \pm \text{syst}) \times 10^6$	total unc. $\times 10^6$ (rel. unc.)
31	$19.6587 \pm 0.0224 \pm 0.3036$	0.3045 (1.549%)
33	$19.3022 \pm 0.0210 \pm 0.2993$	0.3000 (1.554%)
35	$18.5262 \pm 0.0232 \pm 0.2852$	0.2861 (1.545%)
37	$67.1819 \pm 0.0473 \pm 1.0315$	1.0326 (1.537%)
39	$47.0818 \pm 0.0336 \pm 0.7257$	0.7265 (1.543%)
41	$64.0134 \pm 0.0471 \pm 0.9852$	0.9863 (1.541%)
43	$61.5614 \pm 0.0425 \pm 0.9483$	0.9493 (1.542%)
45	$14.3538 \pm 0.0171 \pm 0.2211$	0.2218 (1.545%)
47	$41.2186 \pm 0.0385 \pm 0.6395$	0.6406 (1.554%)
49	$29.7271 \pm 0.0322 \pm 0.4637$	0.4648 (1.564%)
51	$41.8919 \pm 0.0503 \pm 0.6586$	0.6605 (1.577%)
55	$80.2472 \pm 0.0503 \pm 1.2452$	1.2462 (1.553%)
61	$37.4460 \pm 0.0414 \pm 0.5609$	0.5624 (1.502%)
63	$35.6231 \pm 0.0289 \pm 0.5289$	0.5297 (1.487%)
65	$41.7867 \pm 0.0358 \pm 0.6307$	0.6317 (1.512%)
$31-65$	$619.6198 \pm 0.5316 \pm 9.4548$	9.4697 (1.53%)

Table A.4: The number of $N_{B\bar{B}}$ measured for each individual experiment and the total number for the complete data set used in this analysis. The statistical and systematic uncertainty are given. The last column represents the total absolute uncertainties as well as the total relative uncertainty [88], [67].

A.5 Supplementary Material for the MC-data disagreement

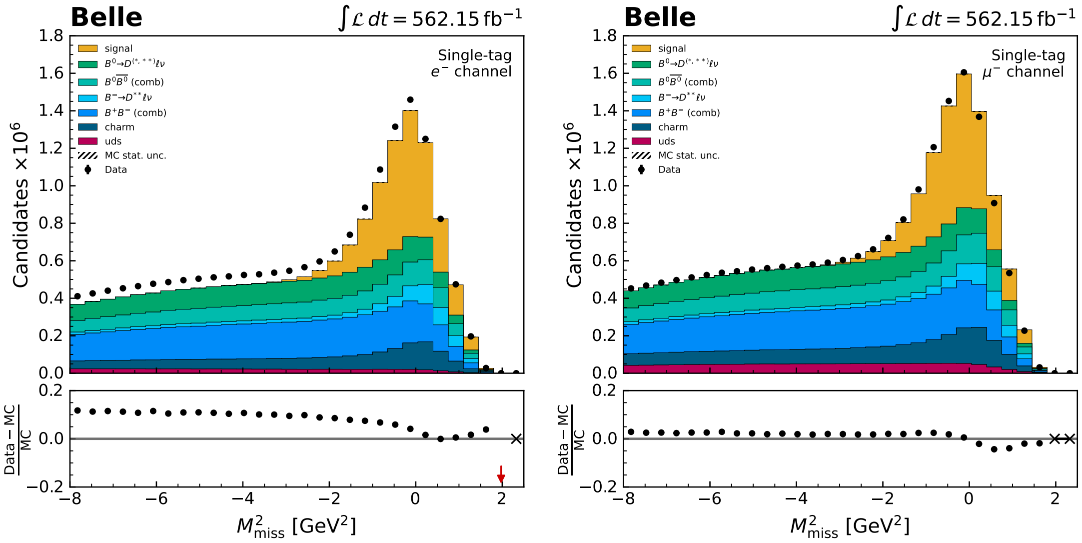

Figure A.10: The M^2_{miss} distribution, separately for the electron channel (left) and muon channel (right). The distribution of pulls is shown below. The disagreement in the electron channel is more significant, although qualitatively the deviation in the signal region is comparable: the *dip* in the pull distribution is observed in both reconstructed channels.

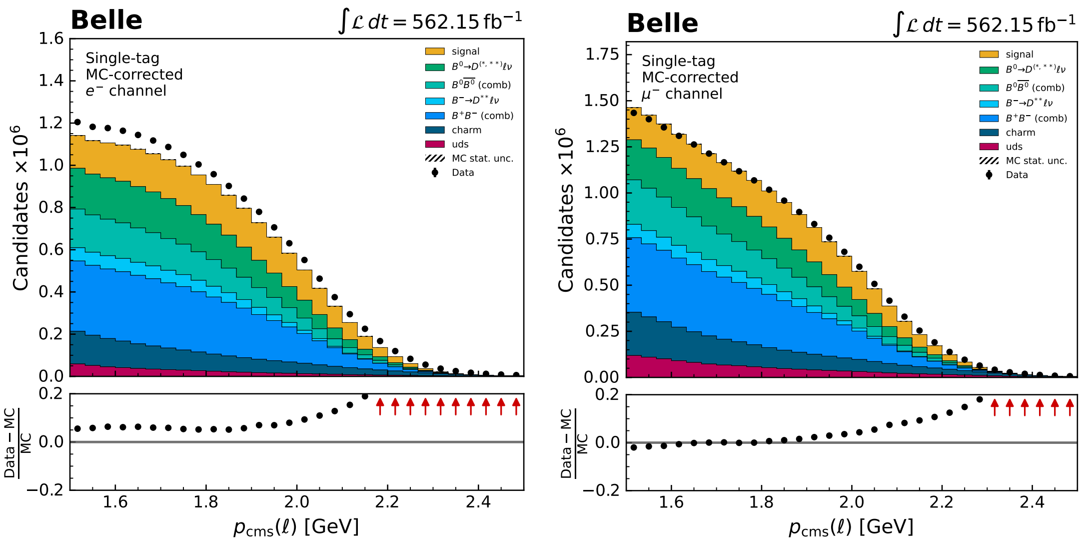

Figure A.11: Distribution of electron momentum (left) and muon momentum (right). The plots show the comparison of MC and experimental data. The distribution of pulls is shown below. It cannot be concluded from these plots that the agreement is systematically better or worse for one type of lepton.

Bibliography

[1] R. L. Workman and Others. “Review of Particle Physics”. In: *PTEP* 2022 (2022), p. 083C01. DOI: 10.1093/ptep/ptac097.

[2] Bernard Aubert et al. “Measurement of the branching fraction of $\Upsilon(4S) \to B^0\overline{B}^0$”. In: *Phys. Rev. Lett.* 95 (2005), p. 042001. DOI: 10.1103/PhysRevLett.95.042001. arXiv: hep-ex/0504001.

[3] David Griffiths. *Introduction to elementary particles*. 2008. ISBN: 978-3-527-40601-2.

[4] W. Buchmuller and C. Ludeling. “Field Theory and Standard Model”. In: *2005 European School of High-Energy Physics*. 2006. arXiv: hep-ph/0609174.

[5] Steven Weinberg. *The Quantum Theory of Fields, Volume 1: Foundations*. Cambridge University Press, 1995.

[6] MissMJ. *Standard Model of Elementary Particles*. Accessed: 2024-06-12. 2014. URL: https://upload.wikimedia.org/wikipedia/commons/0/00/Standard_Model_of_Elementary_Particles.svg.

[7] Paul Strange. “The Dirac Equation”. In: *Relativistic Quantum Mechanics: With Applications in Condensed Matter and Atomic Physics*. Cambridge University Press, 1998, pp. 99–129.

[8] Steven Weinberg. “The making of the Standard Model”. In: *European Physical Journal C* 34 (2004). DOI: 10.1140/epjc/s2004-01761-1.

[9] Makoto Kobayashi and Toshihide Maskawa. “CP-Violation in the Renormalizable Theory of Weak Interaction”. In: *Progress of Theoretical Physics* 49.2 (1973), pp. 652–657. ISSN: 0033-068X. DOI: 10.1143/PTP.49.652. eprint: https://academic.oup.com/ptp/article-pdf/49/2/652/5257692/49-2-652.pdf. URL: https://doi.org/10.1143/PTP.49.652.

[10] J. Charles et al. “CP violation and the CKM matrix: assessing the impact of the asymmetric B factories”. In: *Eur. Phys. J. C* 41 (2005), pp. 1–131. DOI: 10.1140/epjc/s2005-02169-1. URL: https://doi.org/10.1140/epjc/s2005-02169-1.

[11] T Muta. *Foundations of Quantum Chromodynamics*. WORLD SCIENTIFIC, 1987. DOI: 10.1142/0022. eprint: https://www.worldscientific.com/doi/pdf/10.1142/0022. URL: https://www.worldscientific.com/doi/abs/10.1142/0022.

[12] E. Noether. “Invariante Variationsprobleme”. ger. In: *Nachrichten von der Gesellschaft der Wissenschaften zu Göttingen, Mathematisch-Physikalische Klasse* 1918 (1918), pp. 235–257. URL: http://eudml.org/doc/59024.

[13] W. Heisenberg. “Über den Bau der Atomkerne. I”. In: *Zeitschrift für Physik* 77 (1932), pp. 1–11. DOI: 10.1007/BF01342433. URL: https://doi.org/10.1007/BF01342433.

[14] Claude Amsler. *Kern- und Teilchenphysik*. 1st ed. 264 Abb., 2 Fotos. Stuttgart: utb GmbH, 2007, p. 376. ISBN: 9783825228859. DOI: 10.36198/9783838528854.

[15] Bruno Berganholi et al. “Symmetries in particle physics: from nuclear isospin to the quark model”. In: (2024). arXiv: 2404.15988 [hep-ph].

[16] Klaus Schulten. *Notes on Quantum Mechanics*. 405 N. Mathews Street, Urbana, IL 61801 USA: Department of Physics and Beckman Institute, University of Illinois at Urbana-Champaign, 2000.

[17] Y. Amhis et al. “Averages of b-hadron, c-hadron, and τ-lepton properties as of 2018”. In: *The European Physical Journal C* 81.3 (2021). DOI: 10.1140/epjc/s10052-020-8156-7. URL: https://doi.org/10.1140%2Fepjc%2Fs10052-020-8156-7.

[18] David Atwood and William J. Marciano. “Radiative Corrections and Semileptonic B Decays”. In: *Phys. Rev. D* 41 (1990), p. 1736. DOI: 10.1103/PhysRevD.41.1736.

[19] G. Peter Lepage. “Coulomb corrections for $\Upsilon(4S) \to B\overline{B}$”. In: *Phys. Rev. D* 42 (1990), pp. 3251–3252. DOI: 10.1103/PhysRevD.42.3251.

[20] Roland Kaiser, Aneesh V. Manohar, and Thomas Mehen. “Isospin violation in $e^+e^- \to B\overline{B}$”. In: *Phys. Rev. Lett.* 90 (2003), p. 142001. DOI: 10.1103/PhysRevLett.90.142001. arXiv: hep-ph/0208194.

[21] M. B. Voloshin. “Variation of the relative yield of charged and neutral B mesons across the Upsilon(4S) resonance”. In: *Mod. Phys. Lett. A* 18 (2003), pp. 1783–1792. DOI: 10.1142/S0217732303011538. arXiv: hep-ph/0301076.

[22] M. B. Voloshin. “Relative yield of charged and neutral heavy meson pairs in e+ e- annihilation near threshold”. In: *Phys. Atom. Nucl.* 68 (2005), pp. 771–778. DOI: 10.1134/1.1935010. arXiv: hep-ph/0402171.

[23] M. B. Voloshin. “Charged to neutral B meson yield ratio across the Upsilon(4S) resonance”. In: *AIP Conf. Proc.* 698.1 (2004). Ed. by Zohreh Parsa, pp. 436–439. DOI: 10.1063/1.1664274.

[24] M. B. Voloshin. “Charged-to-neutral meson yield ratio at $\psi(3770)$ and $\Upsilon(4S)$ revisited”. In: *Phys. Rev. D* 97.11 (2018), p. 114023. DOI: 10.1103/PhysRevD.97.114023. arXiv: 1803.11135 [hep-ph].

[25] S. Dubynskiy et al. “Isospin breaking in the yield of heavy meson pairs in e+e- annihilation near threshold”. In: *Phys. Rev. D* 75 (2007), p. 113001. DOI: 10.1103/PhysRevD.75.113001. arXiv: 0704.0293 [hep-ph].

[26] Florian Bernlochner et al. “New approaches to determine $B^\pm$ and B^0 production fractions”. In: *PoS* EPS-HEP2023 (2024), p. 358. DOI: 10.22323/1.449.0358.

[27] Martin Jung. "Branching ratio measurements and isospin violation in B -meson decays". In: *Physics Letters B* 753 (2016). ISSN: 0370-2693. DOI: 10.1016/j.physletb.2015.12.024. URL: http://dx.doi.org/10.1016/j.physletb.2015.12.024.

[28] J. P. Alexander et al. "Measurement of the relative branching fraction of upsilon(4S) to charged and neutral B meson pairs". In: *Phys. Rev. Lett.* 86 (2001), pp. 2737–2741. DOI: 10.1103/PhysRevLett.86.2737. arXiv: hep-ex/0006002.

[29] Bernard Aubert et al. "Measurement of branching fractions for exclusive B decays to charmonium final states". In: *Phys. Rev. D* 65 (2002), p. 032001. DOI: 10.1103/PhysRevD.65.032001. arXiv: hep-ex/0107025.

[30] S. B. Athar et al. "Measurement of the ratio of branching fractions of the Upsilon(4S) to charged and neutral B mesons". In: *Phys. Rev. D* 66 (2002), p. 052003. DOI: 10.1103/PhysRevD.66.052003. arXiv: hep-ex/0202033.

[31] N. C. Hastings et al. "Studies of B0 - anti-B0 mixing properties with inclusive dilepton events". In: *Phys. Rev. D* 67 (2003), p. 052004. DOI: 10.1103/PhysRevD.67.052004. arXiv: hep-ex/0212033.

[32] Bernard Aubert et al. "Measurement of the B^+/B^0 production ratio from the $\Upsilon(4S)$ meson using $B^+ \to J/\psi K^+$ and $B^0 \to J/\psi K^0_S$ decays". In: *Phys. Rev. D* 69 (2004), p. 071101. DOI: 10.1103/PhysRevD.69.071101. arXiv: hep-ex/0401028.

[33] S. Choudhury, S. Sandilya, and K. Trabelsi. "Measurement of the B^+/B^0 production ratio in e^+e^- collisions at the $\Upsilon(4S)$ resonance using $B \to J/\psi(\ell\ell)K$ decays at Belle". In: *Phys. Rev. D* 107 (3 2023), p. L031102. DOI: 10.1103/PhysRevD.107.L031102. URL: https://link.aps.org/doi/10.1103/PhysRevD.107.L031102.

[34] Yasmine Sara Amhis et al. "Averages of b-hadron, c-hadron, and τ-lepton properties as of 2018". In: *Eur. Phys. J. C* 81.3 (2021), p. 226. DOI: 10.1140/epjc/s10052-020-8156-7. arXiv: 1909.12524 [hep-ex].

[35] R. M. Baltrusaitis et al. "Direct Measurements of Charmed-D-Meson Hadronic Branching Fractions". In: *Phys. Rev. Lett.* 56 (20 1986), pp. 2140–2143. DOI: 10.1103/PhysRevLett.56.2140. URL: https://link.aps.org/doi/10.1103/PhysRevLett.56.2140.

[36] A. J. Bevan et al. "The Physics of the B Factories". In: *Eur. Phys. J. C* 74 (2014), p. 3026. DOI: 10.1140/epjc/s10052-014-3026-9. arXiv: 1406.6311 [hep-ex].

[37] W. Altmannshofer et al. "The Belle II Physics Book". In: *PTEP* 2019.12 (2019). Ed. by E. Kou and P. Urquijo. [Erratum: PTEP 2020, 029201 (2020)], p. 123C01. DOI: 10.1093/ptep/ptz106. arXiv: 1808.10567 [hep-ex].

[38] I. Adachi et al. "Determination of $|V_{cb}|$ using $\overline{B}^0 \to D^{*+}\ell^-\overline{\nu}_\ell$ decays with Belle II". In: *Phys. Rev. D* 108 (9 2023), p. 092013. DOI: 10.1103/PhysRevD.108.092013. URL: https://link.aps.org/doi/10.1103/PhysRevD.108.092013.

[39] A. Abashian et al. "The Belle detector". In: *Nuclear Instruments and Methods in Physics Research Section A: Accelerators, Spectrometers, Detectors and Associated Equipment* 479.1 (2002). Detectors for Asymmetric B-factories, pp. 117–232. ISSN: 0168-9002. DOI: https://doi.org/10.1016/S0168-9002(01)02013-7. URL: https://www.sciencedirect.com/science/article/pii/S0168900201020137.

[40] KEK. "KEKB B factory design report". In: *Technical Information and Library* (1995).

[41] MS Zisman. "PEP-II: An Asymmetric B Factory: Conceptual Design Report". In: *SLAC Report* 418 (1993), pp. 2–93.

[42] Belle II collaboration. *Total recorded integrated luminosity up to now.* 2024. URL: http://web.archive.org/web/20080207010024/http://www.808multimedia.com/winnt/kernel.htm (visited on 05/24/2024).

[43] D Besson and T Skwarnicki. "Upsilon Spectroscopy: Transitions in the Bottomonium System". In: *Annual Review of Nuclear and Particle Science* 43.Volume 43, 1993 (1993), pp. 333–378. ISSN: 1545-4134. DOI: https://doi.org/10.1146/annurev.ns.43.120193.002001. URL: https://www.annualreviews.org/content/journals/10.1146/annurev.ns.43.120193.002001.

[44] S. Kurokawa. "KEKB status and plans". In: *Proceedings Particle Accelerator Conference* 1 (1995), 491–494 vol.1. DOI: 10.1109/PAC.1995.504699.

[45] K. Hosoyama et al. "Development of the KEK-B Superconducting Crab Cavity". In: *Conf. Proc. C* 0806233 (2008). Ed. by Ivan Andrian and Christine Petit-Jean-Genaz, THXM02.

[46] Y. Ushiroda. "Belle silicon vertex detectors". In: *Nuclear Instruments and Methods in Physics Research Section A: Accelerators, Spectrometers, Detectors and Associated Equipment* 511.1 (2003). Proceedings of the 11th International Workshop on Vertex Detectors, pp. 6–10. ISSN: 0168-9002. DOI: https://doi.org/10.1016/S0168-9002(03)01739-X. URL: https://www.sciencedirect.com/science/article/pii/S016890020301739X.

[47] Shoji Uno. "The BELLE central drift chamber". In: *Nuclear Instruments and Methods in Physics Research Section A: Accelerators, Spectrometers, Detectors and Associated Equipment* 379.3 (1996). Proceedings of the Sixth International Conference on Instrumentation for Experiments at e+ e- Colliders, pp. 421–423. ISSN: 0168-9002. DOI: https://doi.org/10.1016/0168-9002(96)00555-4. URL: https://www.sciencedirect.com/science/article/pii/0168900296005554.

[48] Particle Data Group. "Review of Particle Physics". In: *Progress of Theoretical and Experimental Physics* 2022.8 (2022), p. 083C01. ISSN: 2050-3911. DOI: 10.1093/ptep/ptac097. eprint: https://academic.oup.com/ptep/article-pdf/2022/8/083C01/49175539/ptac097.pdf. URL: https://doi.org/10.1093/ptep/ptac097.

[49] T Iijima et al. "Aerogel Cherenkov counter for the BELLE detector". In: *Nuclear Instruments and Methods in Physics Research Section A: Accelerators, Spectrometers, Detectors and Associated Equipment* 453.1 (2000). Proc. 7th Int. Conf on Instrumentation for colliding Beam Physics, pp. 321–325. ISSN: 0168-9002. DOI: https://doi.org/10.1016/S0168-9002(00)00652-5. URL: https://www.sciencedirect.com/science/article/pii/S0168900200006525.

[50] H Kichimi et al. "The BELLE TOF system". In: *Nuclear Instruments and Methods in Physics Research Section A: Accelerators, Spectrometers, Detectors and Associated Equipment* 453.1 (2000). Proc. 7th Int. Conf on Instrumentation for colliding Beam Physics, pp. 315–320. ISSN: 0168-9002. DOI: https://doi.org/10.1016/S0168-9002(00)00651-3. URL: https://www.sciencedirect.com/science/article/pii/S0168900200006513.

[51] A. Abashian et al. "The K(L) / mu detector subsystem for the BELLE experiment at the KEK B factory". In: *Nucl. Instrum. Meth. A* 449 (2000), pp. 112–124. DOI: 10.1016/S0168-9002(99)01383-2.

[52] A. Abashian et al. "The KLM detector subsystem for the BELLE experiment at the KEK B-factory". In: *Nuclear Instruments and Methods in Physics Research Section A: Accelerators, Spectrometers, Detectors and Associated Equipment* 449.1 (2000), pp. 112–124. ISSN: 0168-9002. DOI: https://doi.org/10.1016/S0168-9002(99)01383-2. URL: https://www.sciencedirect.com/science/article/pii/S0168900299013832.

[53] K Hanagaki et al. "Electron identification in Belle". In: *Nuclear Instruments and Methods in Physics Research Section A: Accelerators, Spectrometers, Detectors and Associated Equipment* 485.3 (2002), pp. 490–503. ISSN: 0168-9002. DOI: https://doi.org/10.1016/S0168-9002(01)02113-1. URL: https://www.sciencedirect.com/science/article/pii/S0168900201021131.

[54] A Abashian et al. "Muon identification in the Belle experiment at KEKB". In: *Nuclear Instruments and Methods in Physics Research Section A: Accelerators, Spectrometers, Detectors and Associated Equipment* 491.1 (2002), pp. 69–82. ISSN: 0168-9002. DOI: https://doi.org/10.1016/S0168-9002(02)01164-6. URL: https://www.sciencedirect.com/science/article/pii/S0168900202011646.

[55] T. Kuhr et al. "The Belle II Core Software". In: *Computing and Software for Big Science* 3.1 (2018). DOI: 10.1007/s41781-018-0017-9. URL: https://doi.org/10.1007%2Fs41781-018-0017-9.

[56] Moritz Gelb et al. "B2BII: Data Conversion from Belle to Belle II". In: *Computing and Software for Big Science* 2.1 (2018). DOI: 10.1007/s41781-018-0016-x. URL: https://doi.org/10.1007%2Fs41781-018-0016-x.

[57] Jolanta Brodzicka et al. "Physics achievements from the Belle experiment". In: *Progress of Theoretical and Experimental Physics* 2012.1 (2012), p. 04D001. ISSN: 2050-3911. DOI: 10.1093/ptep/pts072. eprint: https://academic.oup.com/ptep/article-pdf/2012/1/04D001/11595832/pts072.pdf. URL: https://doi.org/10.1093/ptep/pts072.

[58] Torbjorn Sjostrand. “Monte Carlo Generators”. In: *2006 European School of High-Energy Physics*. 2006, pp. 51–74. arXiv: hep-ph/0611247.

[59] David J. Lange. “The EvtGen particle decay simulation package”. In: *Nuclear Instruments and Methods in Physics Research Section A: Accelerators, Spectrometers, Detectors and Associated Equipment* 462.1 (2001). BEAUTY2000, Proceedings of the 7th Int. Conf. on B-Physics at Hadron Machines, pp. 152–155. ISSN: 0168-9002. DOI: https://doi.org/10.1016/S0168-9002(01)00089-4. URL: https://www.sciencedirect.com/science/article/pii/S0168900201000894.

[60] Torbjörn Sjöstrand. “High-energy-physics event generation with PYTHIA 5.7 and JETSET 7.4”. In: *Comput. Phys. Commun.* 82 (1994), pp. 74–89. DOI: 10.1016/0010-4655(94)90132-5. URL: https://cds.cern.ch/record/257199.

[61] Elisabetta Barberio and Zbigniew Was. “PHOTOS - a universal Monte Carlo for QED radiative corrections: version 2.0”. In: *Computer Physics Communications* 79.2 (1994), pp. 291–308. ISSN: 0010-4655. DOI: https://doi.org/10.1016/0010-4655(94)90074-4. URL: https://www.sciencedirect.com/science/article/pii/0010465594900744.

[62] R. Brun et al. “GEANT3”. In: *Geneva : CERN, 1987.* (1987).

[63] Florian U. Bernlochner, Zoltan Ligeti, and Sascha Turczyk. “A proposal to solve some puzzles in semileptonic B decays”. In: *Phys. Rev. D* 85 (9 2012), p. 094033. DOI: 10.1103/PhysRevD.85.094033. URL: https://link.aps.org/doi/10.1103/PhysRevD.85.094033.

[64] Wolfgang Dungel. “Systematic investigation of the reconstruction efficiency of low momentum $\pi^{\pm}$ and π^{0} ”. In: *Belle Note 1176 (Internal)* (2011). URL: https://belle.kek.jp/secured/belle_note/gn1176/bn1176.pdf.

[65] L. Hinz. “Lepton ID efficiency correction and systematic error”. In: *Belle Note 954 (Internal)* (2006). URL: http://belle.kek.jp/secured/belle_note/gn954/lhinz_bn954.ps.gz.

[66] P. Urquijo. “Semi-Inclusive Semileptonic B Decays”. In: *Belle Note 1251 (Internal)* (2012). URL: https://belle.kek.jp/secured/belle_note/gn1251/bn1251_v1.4.pdf.

[67] Kurtis Nishimura. *Number of B events in Hadron B(J)*. 2009. URL: https://belle.kek.jp/secured/nbb/nbb.html (visited on 04/18/2023).

[68] *Belle File Search Engine Ver 4.1*. URL: http://bweb3.cc.kek.jp/ (visited on 04/18/2023).

[69] *Remarks on Generated Generic MC samples*. URL: https://belle.kek.jp/group/software/MC/genericmc.html (visited on 04/18/2023).

[70] S. Duell and F. Bernlochner. “Correction of BF($B \to X_c \ell \nu$) in generic MC”. In: *Belle II - DESY Confluence* (). URL: https://confluence.desy.de/pages/viewpage.action?pageId=202394372 (visited on 09/07/2023).

[71] Florian U. Bernlochner et al. “Semitauonic b-hadron decays: A lepton flavor universality laboratory”. In: *Rev. Mod. Phys.* 94 (1 2022), p. 015003. DOI: 10.1103/RevModPhys.94.015003. URL: https://link.aps.org/doi/10.1103/RevModPhys.94.015003.

[72] Matthias Neubert. “Heavy-quark symmetry”. In: *Physics Reports* 245.5 (1994), pp. 259–395. ISSN: 0370-1573. DOI: https://doi.org/10.1016/0370-1573(94)90091-4. URL: https://www.sciencedirect.com/science/article/pii/0370157394900914.

[73] Matthias Neubert. “QCD-based interpretation of the lepton spectrum in inclusive $\overline{B} \to X_u \ell \overline{\nu}$ decays”. In: *Phys. Rev. D* 49 (7 1994), pp. 3392–3398. DOI: 10.1103/PhysRevD.49.3392. URL: https://link.aps.org/doi/10.1103/PhysRevD.49.3392.

[74] Irinel Caprini, Laurent Lellouch, and Matthias Neubert. “Dispersive bounds on the shape of $B \to D^{(*)} \ell \nu$ form-factors”. In: *Nucl. Phys. B* 530 (1998), pp. 153–181. DOI: 10.1016/S0550-3213(98)00350-2. arXiv: hep-ph/9712417.

[75] C. Glenn Boyd, Benjamin Grinstein, and Richard F. Lebed. “Model independent determinations of $B \to D\ell\nu, D^*\ell\nu$ form-factors”. In: *Nucl. Phys. B* 461 (1996), pp. 493–511. DOI: 10.1016/0550-3213(95)00653-2. arXiv: hep-ph/9508211.

[76] Markus Prim. *b2-hive/eFFORT v0.1.0*. Version v0.1.0. 2020. DOI: 10.5281/zenodo.3965699. URL: https://doi.org/10.5281/zenodo.3965699.

[77] R. Glattauer et al. “Measurement of the decay $B \to D\ell\nu_\ell$ in fully reconstructed events and determination of the Cabibbo-Kobayashi-Maskawa matrix element $|V_{cb}|$”. In: *Phys. Rev. D* 93 (3 2016), p. 032006. DOI: 10.1103/PhysRevD.93.032006. URL: https://link.aps.org/doi/10.1103/PhysRevD.93.032006.

[78] Daniel Ferlewicz, Phillip Urquijo, and Eiasha Waheed. “Revisiting fits to $B^0 \to D^{*-}\ell^+\nu_\ell$ to measure $|V_{cb}|$ with novel methods and preliminary LQCD data at nonzero recoil”. In: *Phys. Rev. D* 103 (7 2021), p. 073005. DOI: 10.1103/PhysRevD.103.073005. URL: https://link.aps.org/doi/10.1103/PhysRevD.103.073005.

[79] Daryl Scora and Nathan Isgur. “Semileptonic meson decays in the quark model: An update”. In: *Phys. Rev. D* 52 (5 1995), pp. 2783–2812. DOI: 10.1103/PhysRevD.52.2783. URL: https://link.aps.org/doi/10.1103/PhysRevD.52.2783.

[80] Adam K. Leibovich et al. “Semileptonic B decays to excited charmed mesons”. In: *Physical Review D* 57.1 (1998), pp. 308–330. DOI: 10.1103/physrevd.57.308. URL: https://doi.org/10.1103%2Fphysrevd.57.308.

[81] F. Metzner. “R(D*) with Leptonic tau and Hadronic FEI-Tag”. In: *Belle Note 1616 (Internal)* (2023). URL: https://belle.kek.jp/secured/belle_note/gn1616/rdstar_belle_note_1616_v0.1.pdf.

[82] Maximilian Welsch. “Measurement of the branching fraction of $B \to D^{**}(\to D^*\pi^0)\ell\nu$ analysis at the Belle experiment”. In: *Master's thesis* (2019).

[83] B. Casey. “HadronB”. In: *Belle Note 390* (2001). URL: https://belle.kek.jp/secured/belle_note/gn390/bn390_012901.ps.gz.

[84] Marko Staric. “Track smearing in MC”. In: *Belle Internal Wiki* (2012). URL: https://belle.kek.jp/secured/wiki/doku.php?id=physics:charm:tracksmearing.

[85] G. Cowan. *Statistical Data Analysis*. Oxford science publications. Clarendon Press, 1998. ISBN: 9780198501558. URL: https://books.google.de/books?id=ff8ZyW0nlJAC.

[86] Wouter Verkerke and David P. Kirkby. “The RooFit toolkit for data modeling”. In: *eConf* C0303241 (2003). Ed. by L. Lyons and Muge Karagoz, MOLT007. arXiv: physics/0306116.

[87] B. Bhuyan. “High PT Tracking Efficiency Using Partially Reconstructed D∗ Decays”. In: *Belle Note 1165 (Internal)* (2010). URL: https://belle.kek.jp/secured/belle_note/gn1165/BN1165_v1.pdf.

[88] Kurtis Nishimura. *Perl Script including result of NBB measurements*. URL: https://belle.kek.jp/secured/nbb/sum.pl (visited on 04/18/2023).

[89] Kurtis Alan Nishimura. “First observation of the inclusive decay $B \to X_s \eta$ with the BELLE detector”. PhD thesis. Hawaii U., 2010.

[90] Sanjay Kumar Swain. “Search for direct CP violation in $B^- \to D_{CP} K^{(*)-}$”. Other thesis. Hawaii U., 2004.

[91] R. Glattauer et al. “Measurement of the decay $B \to D\ell\nu_\ell$ in fully reconstructed events and determination of the Cabibbo-Kobayashi-Maskawa matrix element $|V_{cb}|$”. In: *Phys. Rev. D* 93.3 (2016), p. 032006. DOI: 10.1103/PhysRevD.93.032006. arXiv: 1510.03657 [hep-ex].